

**ULTRA-HIGH ENERGY COSMIC RAY ENERGY
SPECTRUM USING HYBRID ANALYSIS WITH TAX4**

by
Mathew Potts

A dissertation submitted to the faculty of
The University of Utah
in partial fulfillment of the requirements for the degree of

Doctor of Philosophy
in
Physics

Department of Physics and Astronomy
The University of Utah
May 2022

Copyright © Mathew Potts 2022

All Rights Reserved

The University of Utah Graduate School

STATEMENT OF DISSERTATION APPROVAL

The dissertation of Mathew Potts
has been approved by the following supervisory committee members:

<u>Charles Jui</u> ,	Chair(s)	<u>15 April 2022</u>
		<small>Date Approved</small>
<u>Tareq AbuZayyad</u> ,	Member	<u>15 April 2022</u>
		<small>Date Approved</small>
<u>Yue Zhao</u> ,	Member	<u>15 April 2022</u>
		<small>Date Approved</small>
<u>Steve Wasserbaech</u> ,	Member	<u>15 April 2022</u>
		<small>Date Approved</small>
<u>Michael Vershinin</u> ,	Member	<u>15 April 2022</u>
		<small>Date Approved</small>

by Christoph Boehme, Chair/Dean of
the Department/College/School of Physics and Astronomy
and by David Kieda, Dean of The Graduate School.

ABSTRACT

Cosmic rays are subatomic particles of extraterrestrial origin, and at the highest energies, they are not well understood. The variation of the cosmic ray flux with energy is referred to as the "Energy Spectrum." The measurement of the cosmic ray energy spectrum may hint at where cosmic rays come from. The Telescope Array (TA) Cosmic Ray Observatory, located in Millard County, Utah, is the largest cosmic ray detector in the Northern hemisphere. Following evidence for a hot spot in the arrival directions of the highest energy cosmic rays, TA underwent the TAx4 upgrade to expand the area of Surface Detectors (SD) by a factor of 4. The upgrade included new Fluorescence Detector (FD) stations to view over the expanded SD arrays. In this work, I will present a preliminary cosmic ray energy spectrum using hybrid events from TAx4, the hybrid resolutions of the detector, and data-MC comparisons. I will show this work's preliminary hybrid energy spectrum is in agreement with previous TA measurements, which is a key first step toward future composition and anisotropy studies.

For my parents, Shelley and Keith. Thanks for believing in me when I didn't believe in myself. I wouldn't be here without your love and support.

CONTENTS

ABSTRACT	iii
LIST OF FIGURES	vii
LIST OF TABLES	x
TELESCOPE ARRAY AND PHYSICS NOTATION	xi
CHAPTERS	
1. INTRODUCTION	1
1.1 Cosmic Ray Physics	1
1.1.1 Energy Spectrum	2
1.1.2 Composition	6
1.1.3 Anisotropy	7
1.2 Organization of the Dissertation	8
2. EXTENSIVE AIR SHOWER PHYSICS	12
2.1 Electromagnetic Cascade	12
2.2 Hadronic Core	16
2.3 Muonic Component	18
2.4 Lateral Distribution	19
2.5 Light Production	20
3. THE TELESCOPE ARRAY EXPERIMENT	22
3.1 Overview of TA	22
3.2 TAx4 Fluorescence Detectors	24
3.2.1 TAx4 Mirrors and PMTs	27
3.2.2 Electronics and FADC Readout	27
3.2.3 Trigger	29
3.2.4 Calibration	33
3.2.5 Operation Epochs	33
3.3 TAx4 Surface Detectors	36
3.3.1 Design	37
3.3.2 Trigger	38
3.3.3 Hybrid Trigger	38
3.3.4 Calibration	42
4. MONTE CARLO SIMULATION	47
4.1 CORSIKA	47
4.1.1 Dethinning	48
4.2 Fluorescence Detector Simulation	50

4.2.1	Input	50
4.2.2	Event Weighting	51
4.2.3	Light Production	52
4.2.4	Light Propagation	54
4.2.4.1	Rayleigh Scattering	54
4.2.4.2	Aerosol Scattering	55
4.2.4.3	Ozone Absorption	55
4.3	Surface Detector Simulation	56
4.4	Monte Carlo Set	56
4.4.1	Thrown Distributions	57
4.4.2	Resolution	62
5.	EVENT RECONSTRUCTION	70
5.1	Data Format	70
5.2	FD Reconstruction	72
5.2.1	Pass 0	72
5.2.2	Pass 1	73
5.2.3	Pass 2	74
5.3	SD Reconstruction	77
5.3.1	Pass 0	78
5.3.2	Pass 1	78
5.4	Hybrid Reconstruction	82
5.4.1	Hybrid Geometry Reconstruction	82
5.4.2	Energy Reconstruction	84
6.	DATA SELECTION AND DATA-MC COMPARISON	88
6.1	Example Event	89
6.2	Data-MC Comparisons	89
7.	RESULTS	99
7.1	Spectrum Calculation	99
7.1.1	Event Distribution	99
7.1.2	Aperture	101
7.1.3	Detector Ontime	101
7.1.4	Exposure	103
7.2	Energy Spectrum	103
8.	CONCLUSIONS	111
REFERENCES		113

LIST OF FIGURES

1.1	Cosmic Ray Energy Spectra of Various Experiments	3
1.2	Cosmic Ray Energy Spectra of Various Experiments Multiplied by E^3	4
1.3	$\langle X_{\max} \rangle$ Observed by Recent Experiments	7
1.4	Sky Map of the TA Hotspot	9
1.5	Sky Map of Perseus-Pisces Supercluster Excess	10
2.1	Diagram of an Extensive Air Shower	13
2.2	First Four Splittings in a Heitler Model	15
2.3	First Four Splittings of a Hadronic Cascade	17
2.4	Relative Fluorescence Intensities of Different Experiments	21
3.1	Map of TA	23
3.2	Photo of an SD used for TAx4	25
3.3	Schematic view of the SD's scintillator box	25
3.4	Aerial view of the TAx4 FD Sites	26
3.5	TAx4 Fluorescence Telescopes	28
3.6	Philips XP3062/FL PMT Assembly Picture	28
3.7	TAx4 FADC Rack	30
3.8	Diagram of the Three-fold Coincidence Triggering in TAx4	31
3.9	Vertical Shower Trigger Code Example	34
3.10	Inter-mirror Trigger Code Example	34
3.11	TAx4 FD Daughter Board	35
3.12	UVLED Module in Telescope 25 of TAx4	35
3.13	TAx4 SD Arrays	39
3.14	FADC Waveforms	40
3.15	Single-Muon Peak Measured by TAx4 SD	41
3.16	FWHM/peak of the ADC Distributions of the TA and TAx4 SDs	41
3.17	Position Dependence of the Single-Muon Peaks of a typical SD	44
3.18	RMS Width of the Positional Dependence of the Single-Muon Peaks for TA SDs and TAx4 SDs	45
3.19	Mean Relative Trigger Timings of TAx4 SDs	45

3.20	Non-Linearity of the Typical PMTs for the TA and TAx4 SDs	46
4.1	Lateral Distribution of Thinned CORSIKA Showers	49
4.2	Dethinning Geometry	49
4.3	Thrown Energy Distribution	58
4.4	Thrown Impact Parameter Distribution	59
4.5	Thrown Zenith Angle Distribution	60
4.6	Thrown Azimuthal Angle Distribution	61
4.7	Energy Resolution	65
4.8	Zenith Angle Resolution	66
4.9	In-Plane Angle Resolution	67
4.10	Impact Parameter Resolution	68
4.11	X_{\max} Resolution	69
5.1	Example of a Track-Like Event and a Random Noise Event	75
5.2	Shower Detector Plane (SDP) Diagram	76
5.3	FD Event Display with SDP Fit	77
5.4	FADC Signal Waveforms	79
5.5	Schematic of the Shower Front as it Hits the SD array	80
5.6	SD Timing Fit and Event Display	81
5.7	SDP In-plane Geometry Diagram	83
5.8	Monocular and Hybrid Timing vs Angle Fit	86
5.9	Shower Profile Plot	87
6.1	FD Event Display of Highest Energy Event	90
6.2	SD Event Display of Highest Energy Event	90
6.3	SD Time vs. Angle Fit of Highest Energy Event	91
6.4	Hybrid Time vs. Angle Fit of Highest Energy Event	91
6.5	Profile Plot of the Highest Energy Event	92
6.6	Data-MC Comparison - Zenith Angle	94
6.7	Data-MC Comparison - In-plane Angle	95
6.8	Data-MC Comparison - Azimuthal Angle	96
6.9	Data-MC Comparison - Impact Parameter	97
6.10	Data-MC Comparison - Energy	98
7.1	TAx4 Hybrid Data Distribution	100
7.2	TAx4 Reconstructed Aperture	102

7.3	TAx4 Ontime Plots	105
7.4	TAx4 Hybrid Exposure	106
7.5	Hybrid Energy Spectrum - $J(E)$	108
7.6	Hybrid Energy Spectrum - $E^3 J(E)$	109
7.7	Energy Spectrum Ratio	110

LIST OF TABLES

3.1	Epochal and Minor Changes to the TAx4 Detector	36
4.1	Example Input Card for MC Program	52
4.2	Spectral Feature Locations of TA's Energy Spectrum	52
4.3	TAx4 Resolution Comparison	63
6.1	TAx4 Hybrid Quality Cuts	89
7.1	TAx4 Hybrid Data Events per Energy Bin	100
7.2	TAx4 Reconstructed Aperture per Energy Bin	102
7.3	TAx4 FD Ontime	104
7.4	TAx4 Hybrid Exposure per Energy Bin	104
7.5	TAx4 Hybrid Energy Spectrum per Energy Bin	108

TELESCOPE ARRAY AND PHYSICS NOTATION

TA	Telescope Array Project, an international collaboration for studying UHECRs with the Telescope Array Cosmic Ray Observatory
TAX4	Telescope Array Times Four
TALE	Telescope Array Low Energy extension
UV	Ultraviolet
FD	Fluorescence Detector
SD	Surface Detector
UHE	Ultra High Energy, above 10^{17} eV
UHECR	Ultra High Energy Cosmic Ray
MD	Middle Drum site
FOV	Field Of View
eV	Electron Volts (1 Joule = 6.242×10^{18} eV)
EAS	Extensive Air Shower
PMT	PhotoMultiplier Tube
GZK	Greisen-Zatsepin-Kuzmin
SDP	Shower Detector Plane
MC	Monte Carlo
FADC	Fast Analog Digital Converter
R_p	Impact Parameter
X_{\max}	Parameter where the shower is at maximum development
ICRC	International Cosmic Ray Conference
HV	High Voltage
LV	Low Voltage
MIP	Minimum Ionizing Particle
VEM	Vertical Equivalent Muon

CHAPTER 1

INTRODUCTION

Victor Hess discovered cosmic rays in a series of high-altitude balloon flights in 1912. Initially, Hess made radiation measurements but was hampered by ionizing background radiation. He hoped to reduce ionizing radiation background by performing his experiments at higher altitudes. Hess's experiment measured radiation levels aboard a balloon that ascended to 5 km during a near-total eclipse of the Sun. He used two electrosopes, an early instrument used to measure electric charge, to measure radiation levels as a function of height. He found that radiation levels increased at higher altitudes. Hess reasoned that because the radiation source could not be terrestrial, it must be extraterrestrial. He called the new ionizing radiation *cosmic radiation*. It wasn't until 1925 that Robert Millikan coined the name *cosmic ray*.

Despite the name *cosmic rays*, they aren't rays at all; they are energetic particles accelerated by astrophysical sources. Cosmic rays are emitted from the Sun, from sources in our Galaxy, and from extragalactic sources at the highest energy ranges. Ultra-High Energy Cosmic Rays (UHECRs), cosmic rays with $E > 10^{17}$ eV, are the most energetic particles observed in the universe. For perspective, the Large Hadron Collider (LHC) accelerates protons in counter-rotating beams to 7 TeV (7×10^{12} eV), making the collision energy of 14 TeV (14×10^{12} eV), which are the most energetic particles that humans can produce. This implies that astrophysical sources exist in the universe that can accelerate particles beyond human capability.

1.1 Cosmic Ray Physics

The Ultra-High Energy (UHE) regime of cosmic rays is not well understood. Detecting UHECRs requires detectors with a large aperture and exposure time to generate enough statistics for study. UHECR researchers focus on understanding where they come from, their chemical composition, how they are accelerated to such high energies, and how they

propagate through the intergalactic medium. Experiments like the Telescope Array (TA), discussed in Chapter 3, are conducted to answer these questions through studies of the energy spectrum, anisotropy, and chemical composition.

1.1.1 Energy Spectrum

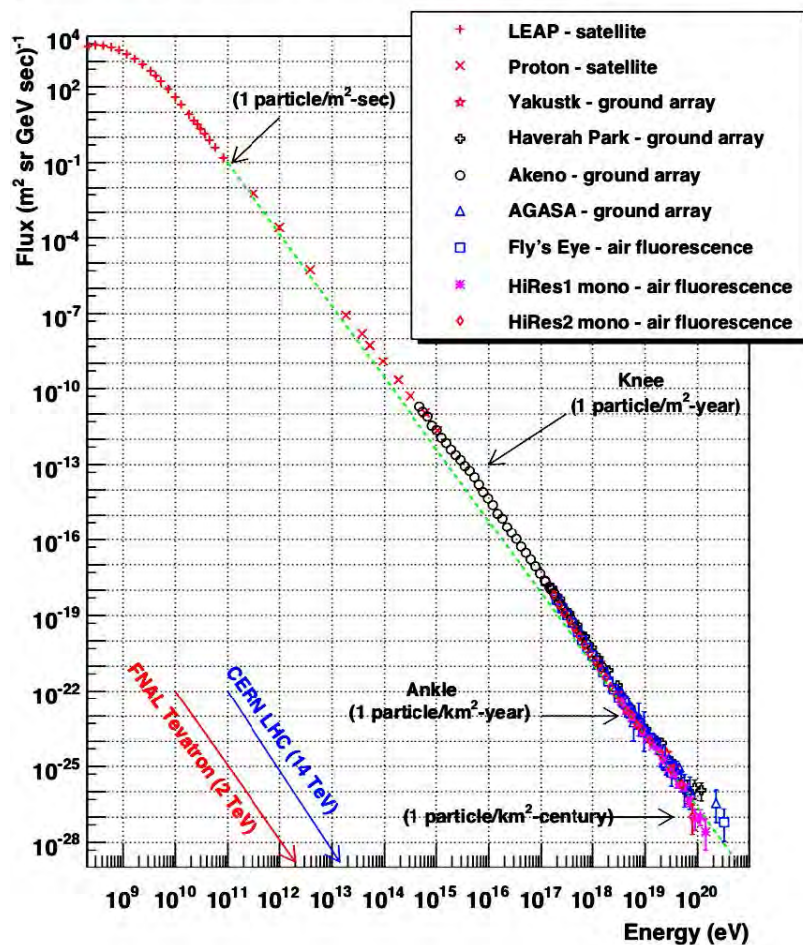
Cosmic rays have a broad range of energies, with experiments observing them across 12 orders of magnitude. Figure 1.1 shows the cosmic ray energy spectrum measured by various experiments. The flux of cosmic rays appears to follow a simple power law, $J(E) \propto E^{-\gamma}$, where γ is the power law's spectral index. The spectral index of cosmic rays across the entire energy range is approximately 3. A E^{-3} power law means that the flux of cosmic rays varies greatly with energy. At lower energies, cosmic rays are numerous, with a flux of 1 particle $\text{m}^{-2}\text{s}^{-1}$, and they are regular background for ground array detectors; however, at high energies above $10^{19.5}$ eV, the flux of cosmic rays drops to 1 particle km^{-2} century $^{-1}$.

The orders-of-magnitude differences in the cosmic ray flux require drastically different detection methods. Below 10^{15} eV, the flux is large enough for direct detection of cosmic ray particles. These experiments typically involve particle detectors on board a high-altitude balloon or satellite. Above 10^{15} eV, the flux is too low for direct detection to be viable. Reliable detection of UHECRs requires an indirect method of detecting cosmic rays by exploiting their interaction with Earth's atmosphere. This interaction is known as an extensive air shower (EAS). The physics of an EAS is discussed in detail in Chapter 2.

Close inspection of Figure 1.1 hints at subtle features that deviate from a simple E^{-3} power law, seen in Figure 1.1 by the dashed green line. If we multiply the flux by E^3 , in order to conceal the dominant E^{-3} trend, we see in Figure 1.2 the features are unmistakable. The "knee" and "second knee," as they are colloquially called, are two softenings of the spectrum that occur at $10^{15.5}$ eV and 10^{17} eV, respectively. At the "ankle," at $10^{18.7}$ eV, the spectrum hardens. There is also a sharp cutoff at $10^{19.5}$. Each feature has important implications for the sources, composition, and propagation of cosmic rays.

Below the knee, the spectral index is 2.7, and above the knee feature, the spectral index is 3.3 [20]. Cosmic rays in this energy range are considered to originate from galactic sources. One of the candidates for the acceleration of these cosmic rays are SuperNovae Remnants (SNRs). SNRs provide energetic shock fronts that expand for thousands of

Cosmic Ray Spectra of Various Experiments



Cosmic Ray Spectra of Various Experiments

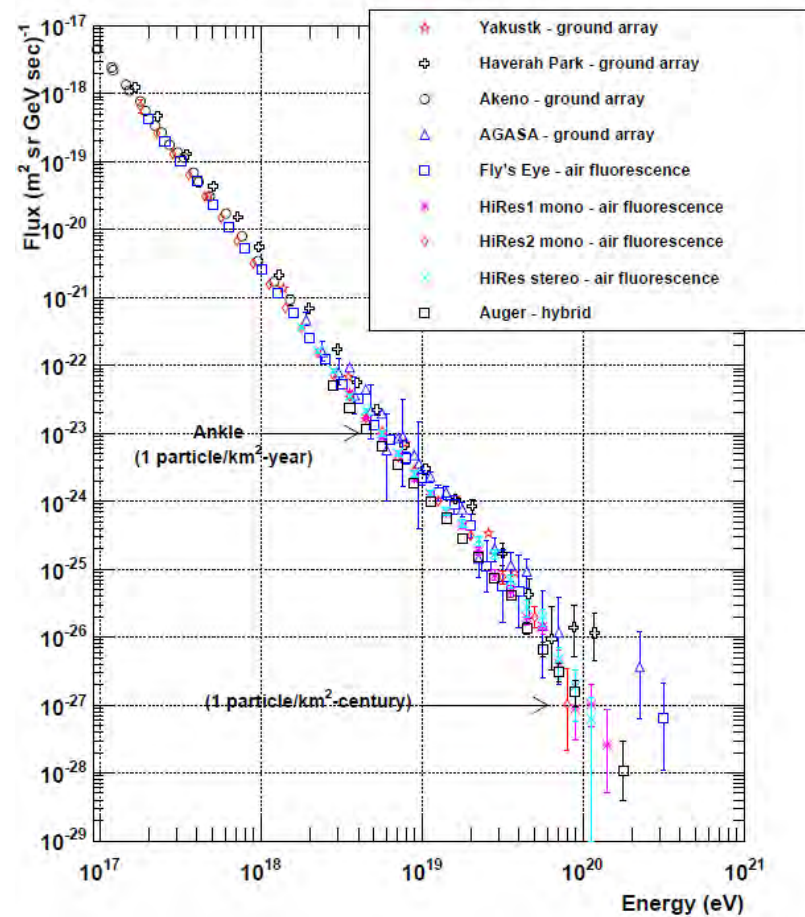
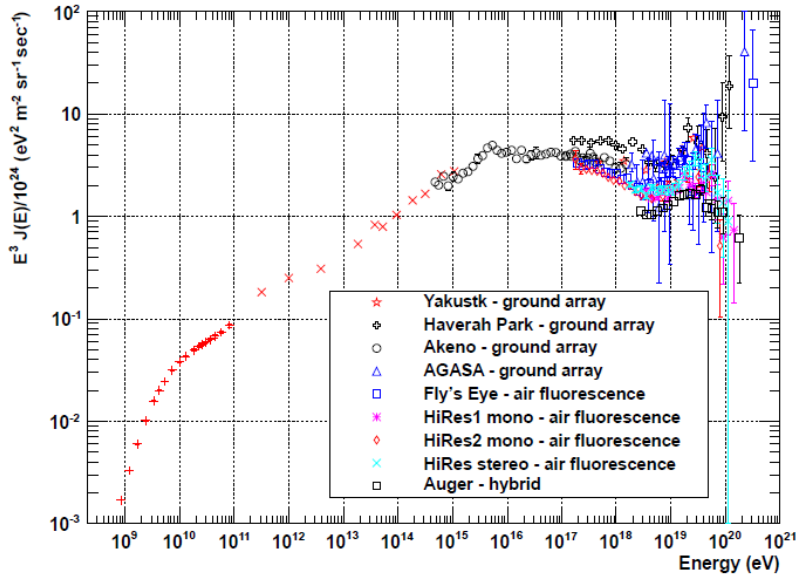


Figure 1.1: Cosmic ray energy spectra of various experiments. (Left) shows the cosmic ray energy spectrum to 10^8 eV. The green dashed line is an E^{-3} power law distribution. There are two spectral features known as the "knee," $E \approx 10^{15.5}$ eV, and the "ankle," $E \approx 10^{18.7}$ eV. Taken from Hanlon [17]. (Right) is the cosmic ray energy spectrum in the UHE regime ($E > 10^{17}$ eV). Taken from Elliot [10].

Cosmic Ray Spectra of Various Experiments



Cosmic Ray Spectra ($E^3 J$) of Various Experiments

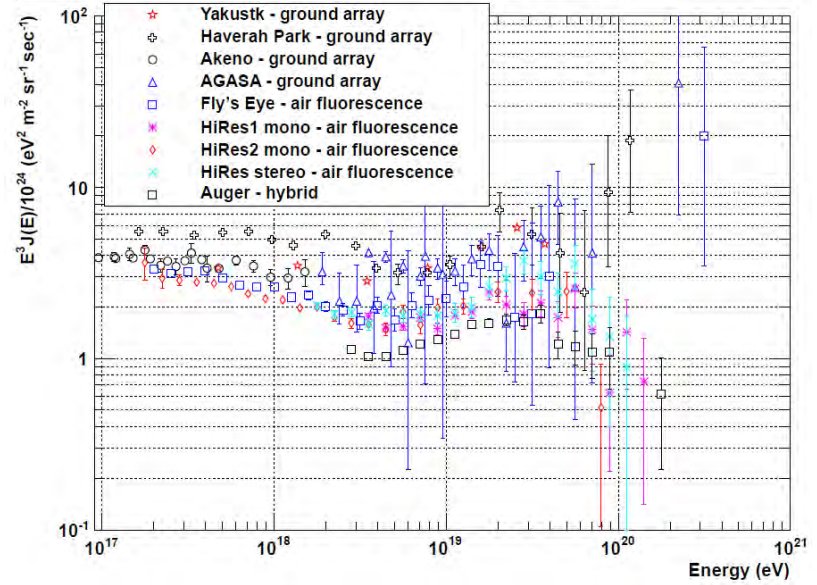


Figure 1.2: Cosmic ray energy spectra of various experiments, multiplied by E^3 . This effectively removes the E^{-3} power law trend seen in the cosmic ray spectrum. (Left) shows the cosmic ray energy spectrum down to 10^8 eV. (Right) is the cosmic ray energy spectrum in the UHE regime ($E > 10^{17}$). Plots taken from Elliot [10].

years after the star has gone supernova. In a process known as first-order Fermi acceleration, particles are accelerated by bouncing repeatedly across the shock front, gaining energy until they escape. This acceleration depends on the characteristic magnetic rigidity, $R_c = E/Ze$. The maximum energy of accelerated particles can be written as

$$E_{max}(Z) = Ze \times R_c = Z \times E_{max}^p. \quad (1.1)$$

When accelerated in a magnetic field, more heavily charged nuclei can achieve Z times higher energy than a proton. The knee feature might be explained as the maximum energy of galactic cosmic ray protons. In conjunction, the "2nd knee," at 10^{17} eV, is exactly 26 times higher in energy and might be interpreted as the maximum energy of galactic iron accelerated by the same sources. The region after the 2nd knee represents a transition from galactic to extragalactic cosmic rays.

Cosmic rays above $10^{18.0}$ eV are demonstrably extragalactic in origin because particles detected above this energy are shown to have a predominately protonic composition. At this rigidity, their arrival directions do not exhibit the anisotropy that would be expected if they were galactic [3].

Extragalactic astrophysical sources have stronger magnetic fields and are larger in size, allowing particles to be accelerated for longer periods of time and to higher energies. There are many candidate sources for extragalactic cosmic ray accelerators, including Supermassive Black Holes (SMBHs), Gamma-Ray Bursts (GRBs), Active Galactic Nuclei (AGN), and BL Lacertae (BL Lacs) objects.

The exact cause of the hardening of the spectrum at the ankle is still under debate; however, there are several plausible hypotheses, such as galactic/extragalactic cosmic ray transition point, a pair-production process of UHE protons interacting with the Cosmic Microwave Background (CMB), or an additional rigidity-dependent cycle of extragalactic sources.

At the highest end of the energy spectrum, the flux of cosmic rays drops significantly. The simplest explanation for this phenomenon is the Greisen–Zatsepin–Kuzmin (GZK) mechanism, where the interaction between UHE protons and Cosmic Microwave Background Radiation (CMBR) above the threshold energy of $10^{19.8}$ eV produce a Delta baryon, as shown in Equation 1.2.

$$\gamma_{CMB} + p \rightarrow \Delta^+(1232\text{MeV}) \rightarrow \begin{cases} p + \pi^0 \\ n + \pi^+ \end{cases} \quad (1.2)$$

The baryon decays via a pion production process that continues until the cosmic ray energy falls below this threshold. The GZK process limits the range of cosmic ray protons to about 50 Mpc, which is less than 1% of the extent of the visible Universe.

1.1.2 Composition

The chemical composition of cosmic rays has important ramifications for our understanding of cosmic ray sources and their propagation through the universe. Many of the features discussed in Section 1.1.1 can be explained by changes in composition. Measuring the composition of lower-energy cosmic rays can be done on an event-by-event basis by direct measurement; however, in the UHE regime, the chemical composition must be inferred from observables in EASs.

Chemical composition determines the statistical characteristics of the EAS development. Thus ground-based experiments, like TA, study the slant depth at which the EAS achieves the maximum number of charged particles, known as X_{\max} , to infer the composition of cosmic rays. The dependence of the average X_{\max} on composition has been observed to follow the approximate relation

$$\langle X_{\max} \rangle \propto \log_{10}(E_0/A), \quad (1.3)$$

where A is the atomic mass of the cosmic ray and E_0 is the energy of the primary cosmic ray. Thus, a shower created by a heavier-mass cosmic ray reaches X_{\max} earlier than an EAS initiated by a proton primary. This phenomenon can also be understood in terms of the different cross-sections. Heavier-mass cosmic rays have larger cross-sections and tend to interact higher in the atmosphere than lighter masses. In addition, heavier nuclei colliding with the atmosphere produce higher multiplicities of secondaries. These effects both contribute to a smaller X_{\max} , on average, for cosmic rays of heavier masses.

Figure 1.3 shows the average X_{\max} observed by recent experiments. There is general agreement of the $\langle X_{\max} \rangle$ below 10^{17} eV, but the distribution of $\langle X_{\max} \rangle$ at higher energies diverges. TA's data indicates a lighter composition for UHECRs, while Pierre Auger Observatory (PAO), the largest cosmic ray observatory in the Southern Hemisphere, shows indications of heavier composition. Currently, a joint working group between TA and

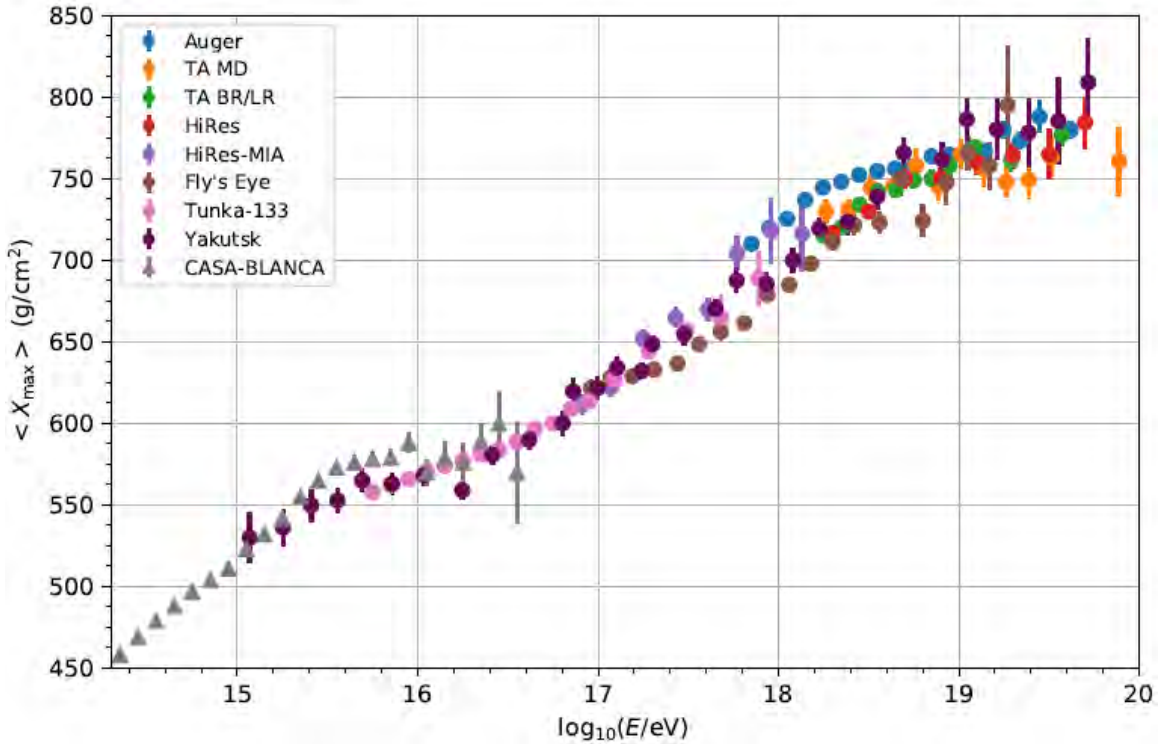


Figure 1.3: $\langle X_{\max} \rangle$ observed by recent experiments. The dependence of mean depth with $\log(E)$ over several decades of energy is apparent. Data from Aab et al. (2014), Abbasi et al. (2010), Abbasi et al.(2014), Abu-Zayyad et al. (2001), Bird et al. (1994), Fowler et al. (2001), Knurenko & Petrov (2015), Prosin et al. (2015), and Abbasi et al. (2018). Taken from Abbasi et al. (2018) [4].

PAO is examining this divergence in $\langle X_{\max} \rangle$ measurements and hopes to improve our understanding of the composition of UHECRs.

1.1.3 Anisotropy

Anisotropy refers to studies of the arrival directions of cosmic ray particles and their correlations with possible sources. Unfortunately, as charged particles, cosmic rays are subject to deflection from both galactic and extragalactic magnetic fields. Therefore, in order to estimate UHECRs trajectories, detailed simulations and models are needed to account for different strengths of magnetic fields at different distances from Earth. The greater energy a cosmic ray, the higher will be its magnetic rigidity, such that its trajectory is less magnetically deflected. Cosmic rays with $E > 10^{19}$ eV are expected only to be deflected by a few degrees over a scale of ~ 50 Mpc, assuming the intergalactic magnetic field strength is on the order of 1 nG [1].

Using the TA surface detectors, the Telescope Array has performed anisotropy searches in several different energy ranges. Cosmic rays' arrival directions with energies between 10^{18} eV to $10^{18.5}$ eV were found to be isotropic, with no excess along the galactic plane [3]. This implies that cosmic rays in this energy range are from extragalactic sources. At the highest energy range, $E > 5.7 \times 10^{19}$ eV, we have found a local cluster of high energy events that has become known as the "TA Hotspot." Figure 1.4 shows the hotspot is located near Ursa Major and $\sim 19^\circ$ from the supergalactic plane [1]. Although there are still no specific identified sources behind the hotspot, it is indicative of a possible localized UHECR source.

A recent anisotropy study using the TA surface detector (SD) data has found a "lower energy" excess of events with $E \geq 10^{19.4}$ near the center of the Perseus-Pisces Supercluster (PPSC) [30]. The PPSC is the closest supercluster to the Northern Hemisphere (70 Mpc away), other than the Virgo Supercluster, which our Milky Way Galaxy belongs to. Using Li-Ma oversampling analysis with 20° radius circles, the excess has a local significance of 4 sigma. Figure 1.5 shows the excess of events found near the PPSC. These results also suggest that the PPSC may be a source of UHECR.

1.2 Organization of the Dissertation

This dissertation focuses on measuring the cosmic ray energy spectrum in the UHE regime using TA's new fourfold expansion, TAx4, in hybrid mode. The measurement of the cosmic ray energy spectrum is important because it may give a hint of where UHECRs come from. This is because the spectral features, introduced in Section 1.1.1, give indications of the astrophysical sources of cosmic rays and their surrounding environments. However, the statistical power of the hybrid spectrum measurement, which requires clear, moonless nights, is only 10% that of the surface detectors alone. At a practical level, the measurement of the hybrid spectrum is a prerequisite step to expand the statistical power of our UHECR composition measurement. The latter is the primary purpose for adding the new fluorescence detectors to the TAx4 expansion.

The cosmic ray energy spectrum can be written as

$$J(E_i) = \frac{N(E_i)}{A\Omega(E_i) \times T \times \Delta E_i}, \quad (1.4)$$

where $J(E_i)$ is the flux of cosmic rays, $N(E_i)$ is the number of observed cosmic rays, $A\Omega(E_i)$

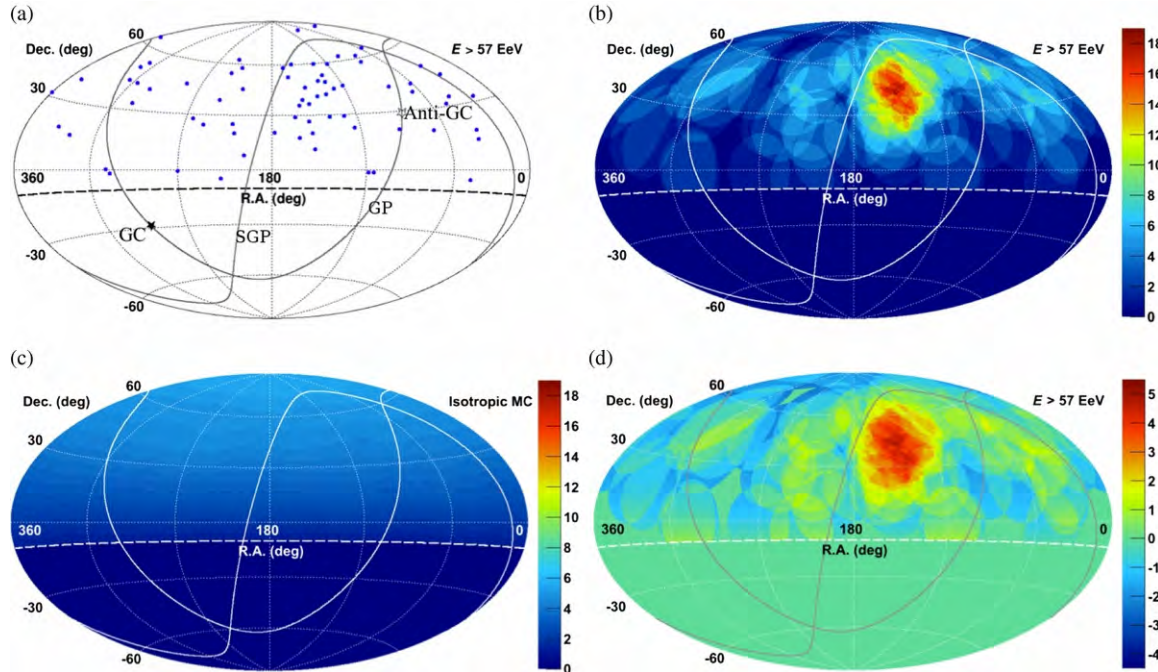


Figure 1.4: The significance map for the direction of the UHECRs observed by the TA surface detectors. UHECR sky maps in equatorial coordinates are shown. (a) The points show the direction of the UHECRs with $E > 57 \text{ EeV}$ ($E > 5.7 \times 10^{19} \text{ eV}$) observed by the TA surface detectors. Note the labeling of the location of the galactic and supergalactic planes (GP and SGP) as well as the galactic center (GC) and anti-galactic center (Anti-GC); (b) Color contours show the number of observed cosmic ray events summed over a 20° radius circle; (c) Number of expected background events from the geometrical exposure summed over a 20° radius circle; (d) Significance map is calculated from (b) and (c). The “Hotspot,” indicated with red colors, is near Ursa Major, just off of the supergalactic plane. Taken from Abbasi et al. (2014) [1]

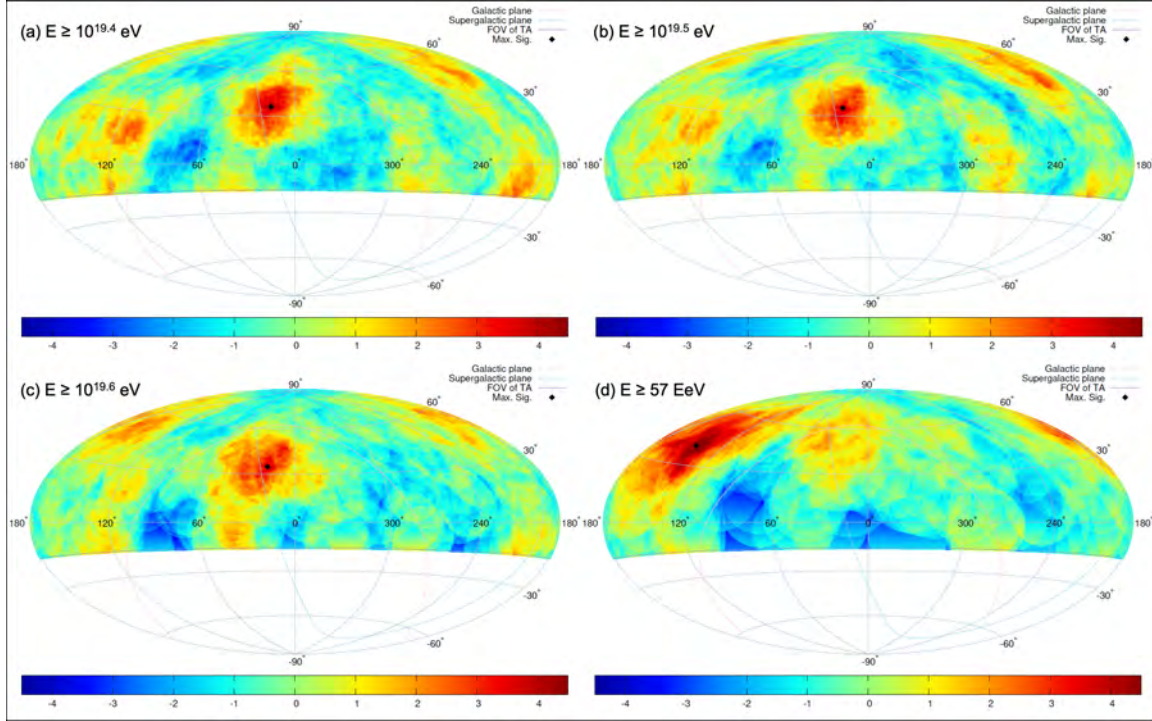


Figure 1.5: Sky maps in equatorial coordinates using Hammer projections. The color scheme indicates the Li-Ma significance and shows the excess (red) or deficit (blue) of events compared to isotropy at each grid point. The positions of maximum excesses are marked with the black diamonds. An intermediate angular scale of 20° -radius circles were used for oversampling analysis for different energy thresholds. The energy cut for each map is (a) $E \geq 10^{19.4}$ eV, (b) $E \geq 10^{19.5}$ eV, (c) $E \geq 10^{19.6}$ eV, and (d) $E \geq 57$ EeV. For three lower energies, (a) to (c), a new excess of events is consistently observed in the same direction. When the energy cut is raised to $E \geq 57$ EeV (d), the maximum significance moves to the previously observed hotspot; however, a smaller excess remains. Note that the right ascension of 0° is at the center of the sky map.

is the energy-dependent aperture calculated from Monte Carlo (MC) simulation, T is the detector ontime, and ΔE_i is the width of the i^{th} energy bin, E_i .

In Chapter 2, I will use simplified models to discuss Extensive Air Showers (EAS) in the atmosphere induced by cosmic rays. This chapter also introduces the different components of an EAS and how light is produced.

In Chapter 3, a general description of the Telescope Array (TA) and TAx4 experiments are given. The focus will be on TA’s newest sub-array, TAx4, so named because it quadruples the size of TA. This chapter will discuss TAx4’s fluorescence and surface detectors’ electronics, trigger design, and calibration.

In Chapter 4, the Monte Carlo simulations used in this work are discussed. It begins with an introduction to CORSIKA and its implementation in the Surface Detector (SD) and Fluorescence Detector (FD) simulations. Then I will show the MC set generated for this work, including the thrown and reconstructed event distributions. This MC set is used to produce the TAx4 detector resolutions.

In Chapter 5, I will discuss the format of the TAx4 data and introduce the TAx4 detector’s hybrid reconstruction chain. The relevant SD and FD monocular reconstruction passes will be presented before discussing how event geometries and energies are reconstructed in hybrid mode.

In Chapter 6, I describe how events are selected and verify that we understand our detector using MC simulations. This is done by data-MC comparisons of various parameters to assess the extent to which the data and MC agree.

In Chapter 7, the calculation of the cosmic ray flux measured by the TAx4 detector in hybrid mode is presented. A discussion of this work’s energy spectrum measurement compared to other cosmic ray experiments follows.

In Chapter 8, I summarize the result of the energy spectrum measurement, discuss the scientific importance of this result, and project the direction of future work.

CHAPTER 2

EXTENSIVE AIR SHOWER PHYSICS

At energies below 10^{15} eV, balloon and satellite experiments are used to measure and study cosmic rays directly at the top of the atmosphere; however, direct detection becomes impractical in the UHE regime because of the steeply falling flux of cosmic rays. For example, a 1 m^2 , 2π steradian detector would detect approximately one 10^{17} eV event every 50 years. Thus, an indirect detection method is needed to study UHECRs. Most of these methods exploit cosmic rays' interaction with Earth's atmosphere. When a primary cosmic ray particle collides with a nucleus in an air molecule high in the atmosphere, it initiates a cascade of relativistic secondary particles. Early in the cascade, the number of secondary particles grows as a power law until it reaches a maximum, approximately $2/3$ particles per GeV of primary energy [21]. The number of secondary particles also has a lateral extent on the order of hundreds of meters to several kilometers. This phenomenon is referred to as an Extensive Air Shower (EAS). The passage of the EAS particles through the atmosphere generates Cerenkov and scintillation (air fluorescence) light. The energy, particle type, and arrival direction of the primary cosmic ray can be inferred from the measured properties of the shower.

EASs develop in three channels: the hadronic core, the muon component, and the electromagnetic (EM) cascade. Figure 2.1 shows a diagram of an EAS. I will discuss each development channel in the following sections, beginning with simplified models. This will be followed by a discussion of their limitations.

2.1 Electromagnetic Cascade

The hadronic core of the EAS drives the EM cascade. A third of pions produced in hadronic collisions are neutral pions, π^0 , and they decay electromagnetically into two photons each ($\pi^0 \rightarrow 2\gamma$). These high-energy photons, in turn, initiate an EM cascade when they undergo pair production. Pair production results from the interaction between

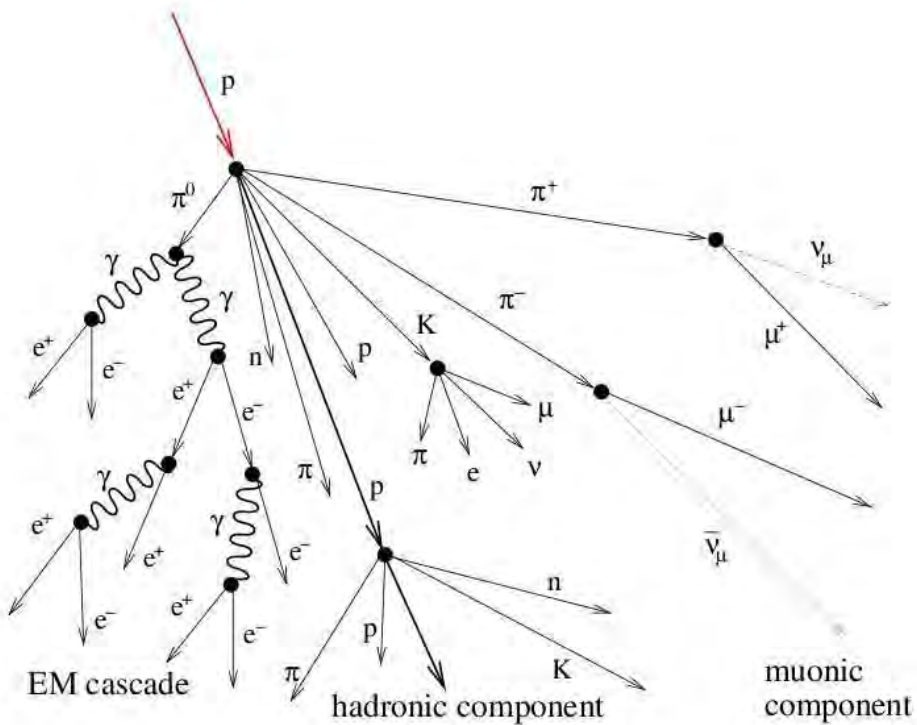


Figure 2.1: Cartoon of an Extensive Air Shower (EAS). There are three components to an EAS shower. The EM cascade is initiated by high-energy photons caused by the decay of neutral pions, π^0 . The cascade grows in size through bremsstrahlung and pair production to a maximum. The hadronic core produces mesons and fermions that feed the other two components of the shower. The EM cascade is responsible for fluorescence light detected by the telescopes. The muonic component rarely interacts in the atmosphere and reaches the ground. All three components produce a signal in the ground array, but the EM and muonic components contribute the most. Taken from M. Allen's Ph.D. thesis [9].

a high energy photon (≥ 1 MeV) and a charged nucleus A ($\gamma + A \rightarrow e^+ + e^- + A$). The resulting electron or positron can then radiate photons via bremsstrahlung in the vicinity of heavy nuclei ($e^{+,-} + A \rightarrow e^{+,-} + A + \gamma$). As the number of particles in the EM cascade grows, the energy of each particle decreases. The shower development continues until the average energy of shower particles falls below a critical energy (e.g., in air, $\epsilon_c^{em} = 85$ MeV [26]). Below this critical energy level, ionization becomes the dominant mode of energy loss rather than bremsstrahlung. Beyond this point, the number of particles decays exponentially. The shower maximum provides important information like X_{\max} , the slant depth to the shower maximum in g/cm², and N_{\max} , the maximum number of secondary particles in the shower.

Walter Heitler proposed a simple model for describing the general behavior of the EM cascade development [18]. The Heitler model has the electrons, positrons, and photons undergoing repeated splittings into two daughter particles, as depicted in Figure 2.2. Every particle splits after it travels a fixed interaction length, or more accurately, after a fixed interaction depth (measured in g/cm²), as defined by

$$X = \lambda_r \ln 2, \quad (2.1)$$

where λ_r is called the *radiation length*. The radiation length is dependent on the medium (e.g., in air $\lambda_r \approx 37$ g/cm² [26]), and the interaction length is defined in such a way that particles, on average, lose half their energy by radiation, as described by

$$\frac{1}{2}E = Ee^{-X/\lambda_r}. \quad (2.2)$$

After n interaction lengths of a cascade, indicated by a photon of energy E_0 , it has traversed

$$X_n = n\lambda_r \ln 2 \quad (2.3)$$

g/cm² of distance. The number of particles in the shower is now

$$N = 2^n = e^{X_n/\lambda_r}, \quad (2.4)$$

and each particle has an energy of

$$E_n = E_0/N. \quad (2.5)$$

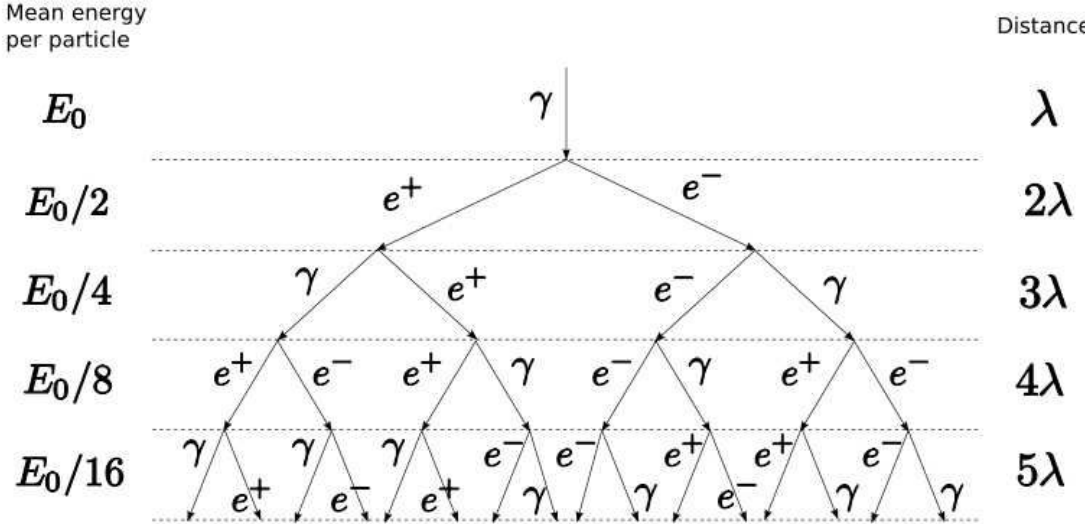


Figure 2.2: The first four splittings in a Heitler Model [18] of an EM cascade initiated by a high energy photon. The cascade continues, perpetuated by pair production and bremsstrahlung, until the energy per particle reaches a critical energy, ϵ_c^{em} , that is proportional to the medium.

The shower development stops after n_c interaction lengths, when the energies of the individual particles are too low for pair production or bremsstrahlung. We obtain from Equation 2.4 and 2.5 the maximum shower size, defined as

$$N_{max} = E_0 / \epsilon_c^{em} = 2^{n_c}, \quad (2.6)$$

where

$$n_c = \ln(E_0 / \epsilon_c^{em}) / \ln 2. \quad (2.7)$$

Since the fluorescence light emitted is proportional to the number of particles in the shower, the total light produced is directly proportional to the primary cosmic ray energy. The penetration depth, X_{max} , at which the shower reaches maximum size, is

$$X_{max}^\gamma = n_c \lambda_r \ln 2 = \lambda_r \ln(E_0 / \epsilon_c^{em}). \quad (2.8)$$

We see that X_{max}^γ evolves logarithmically with the energy of the primary cosmic ray. The measurement of X_{max} plays a critical role in identifying the composition of the primary cosmic ray.

Heitler's model is limited because of its many simplifying assumptions. It assumes that all the particle's cross-sections are independent of their energy, that the energy loss from

collisions is negligible, and that the energy will be evenly distributed among the secondary particles. All of these assumptions don't reflect what happens in reality. In addition, the ratio of electrons to photons is overestimated by about a factor of four. Despite this, the Heitler model gives the correct dependence on the observable such as N_{\max} and X_{\max} ; however, a more robust model is needed to describe EM cascades accurately. The general form used for fitting the development of charged particles in an EAS is known as the Gaisser-Hillas equation,

$$N(X) = N_{\max} \left(\frac{X - X_0}{X_{\max} - X_0} \right)^{\frac{X_{\max} - X_0}{\lambda}} \exp \left(\frac{X_{\max} - X}{\lambda} \right). \quad (2.9)$$

It describes the longitudinal development of an EAS using four parameters: N_{\max} , X_{\max} , X_0 , and λ . This formula was developed in 1977 using a simulation of the EAS process. The variable X , or slant depth, is used to describe the atmospheric depth that the shower has traveled through, defined by

$$X = \int \rho(X') dX'. \quad (2.10)$$

The use of slant depth for describing shower development allows us to compare showers in a way that is relatively independent of their zenith angles.

2.2 Hadronic Core

In a typical collision in the hadronic core of the shower, about 2/3 of the daughter particles produced are pions; about 10% are kaons, and the rest consist of heavier mesons and baryons. In the first few generations of secondary particles, the hadronic core is dominant. Still, roughly 20% of the energy is transferred to the EM cascade after each collision because a third of the pions produced are neutral. Neutral pions have a much shorter lifetime (8.5×10^{17} s) than charged pions, so the neutral pions decay almost immediately. The much slower decay of charged pions ($\pi^{+,-} \rightarrow \mu^{+,-} + \nu_\mu$), on the other hand, feeds a muonic component of the shower. If they haven't decayed, the charged pions and other hadrons undergo subsequent collisions and produce more hadrons. The hadron shower continues until it reaches the ground and produces a signal in the surface detectors.

The hadronic component of an EAS can be modeled in an approach similar to Heitler's. Consider a proton primary cosmic ray with total energy E_0 , depicted in Figure 2.3. After n interaction lengths,

$$X_n = n\lambda_{had} \ln 2, \quad (2.11)$$

where λ_{had} is the nuclear interaction length (e.g., for pions, $\lambda_\pi \approx 120\text{g/cm}^2$ [26]). Hadrons interact at each layer, producing N_{ch} charged pions, defined by

$$N_\pi = (N_{ch})^n, \quad (2.12)$$

as well as $\frac{1}{2}N_{ch}$ neutral pions. In this model, the neutral pions immediately decay to photons, and most of charged pions continue to interact at each level, with only a few decaying at the top of the atmosphere where the spacing between target nuclei is large. The energy is assumed to be equally divided during particle production, except that a third of the energy is lost at each step to the EM component. The energy of each charged pion is

$$E_\pi = \frac{E_0}{(\frac{3}{2}N_{ch})^n}. \quad (2.13)$$

After n_c interaction lengths, where

$$n_c = \frac{\ln(E_0/\epsilon_c^\pi)}{\ln(\frac{3}{2}N_{ch})}, \quad (2.14)$$

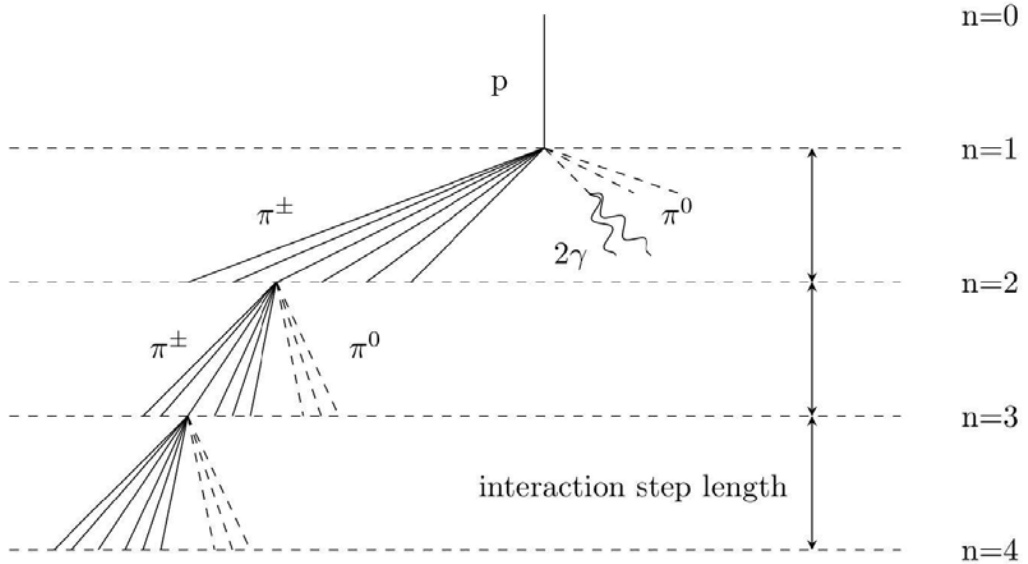


Figure 2.3: The first four splittings of a hadronic cascade induced by a cosmic ray proton. At each interaction length, charged pions, $\pi^{+,-}$, are created and neutral pions, π^0 , are produced. The neutral pions quickly decay into photons, which produce EM sub-showers. The hadronic cascade will continue until the energy per particle reaches a critical energy, ϵ_c^{had} , when the rest of the particles decay into muons.

the energy per particle reaches a critical energy, ϵ_c^π , and all remaining pions are assumed to decay to low-energy muons. The depth of the shower maximum is defined as

$$X_{\max}^p = X_0^p + \lambda_r \ln(E_0 / (3N_{ch}\epsilon_c^{em})). \quad (2.15)$$

The shower maximum depth, X_{\max}^p , depends both on the depth of the first interaction of the primary proton and the number of charged pions created in the first interaction of the hadronic cascade.

The energy of the primary cosmic ray is divided between N_{\max} electromagnetic particles and N_π pions, where the number of pions is equal to the number of muons ($N_\pi = N_\mu$). The total energy of the EAS is

$$E_0 = \epsilon_c^{em} N_{\max} + \epsilon_c^\pi N_\pi. \quad (2.16)$$

The relative contributions from N_{\max} and N_π is determined by their respective critical energies. This model assumes a proton primary, but different primary particles allocate energy differently between the electromagnetic and hadronic components. Equation 2.16 accounts for these differences.

Like Heitler's EM model, this Hadronic Heitler model oversimplifies the hadronic core interactions. The energy of secondary particles is taken to be equally divided; however, in reality, there are large fluctuations in the *multiplicity* and *inelasticity* of the secondary particles. Multiplicity is the number of particles produced for an incident particle that collides with a target particle of a given species. Inelasticity is the fraction of the incident particle's energy available for particle production. The proton-air cross-section is another important parameter in determining the shape of the shower development. It increases with energy and results in different shower maximum depth. All hadronic models describing air showers at the highest energies require the extrapolation of the accelerator measurements and rely on phenomenological models to estimate collision parameters in the UHE regime. This is a major source of uncertainty in interpreting the experimental EAS data [2].

2.3 Muonic Component

Muons in EASs are mainly produced via the decay of charged pions; however, charged kaons can also decay into muons, either directly or by producing charged pions. Due

to the relatively long mean lifetime of charged pions (2.8×10^{-8} s), most of the muonic component of the EAS is generated in the upper atmosphere. The air density in the upper atmosphere is such that charged pions have more of a chance to decay than to collide with air molecules. In general, the muonic component of the shower does not interact until it reaches the ground. As a result, there are very few high-energy muons in an EAS, and they make a negligible contribution to the Cerenkov and fluorescence light produced by shower particles. However, muons will contribute to the signal in the surface detectors because of their charge. In fact, muons will dominate in large zenith angle events where the EM and hadronic components have died out.

In the Heitler-like model described in Section 2.2, the number of muons produced is defined as

$$N_\mu = N_\pi = (N_{ch})^{n_c}. \quad (2.17)$$

These simplified models are important for showing the basic physics involved, but they don't reflect the complexities of reality. For example, we expect the total muon production to increase more quickly with the primary's energy than in our simple model. This discrepancy is because less energy is lost to the electromagnetic component at every interaction length. Calculating the correct total number of muons produced in a shower is important for determining the "missing energy correction." The missing energy correction corrects for the $\sim 10\%$ of the primary cosmic ray's total energy. This missing energy is carried away by charged pions or kaons decaying into muons and accompanying muon neutrinos.

2.4 Lateral Distribution

An EAS has a lateral width approximately described by the Nishimura-Kamata-Greisen (NKG) function [14]. This function describes the lateral distribution of electron density, represented by

$$\rho(r) = \frac{N}{r^2} f\left(s, \frac{r}{r_M}\right), \quad (2.18)$$

where f is the Nishimura-Kamata function, defined as

$$f\left(s, \frac{r}{r_M}\right) = \left(\frac{r}{r_M}\right)^{s-2} \left(1 + \frac{r}{r_M}\right)^{s-4.5} \left(\frac{\Gamma(4.5-s)}{2\pi\Gamma(s)\Gamma(4.5-2s)}\right), \quad (2.19)$$

where N is the total number of electrons, s is the shower age, and r_M is the Moliere radius for multiple scattering. The shower age

$$s = \frac{3X}{X + 2X_{\max}} \quad (2.20)$$

is a dimensionless variable that describes the shower's development relative to X_{\max} . It is defined such that $s = 0$ when $X = 0$, $s = 1$ at $X = X_{\max}$, and $s \rightarrow 3$ when $X \gg X_{\max}$.

2.5 Light Production

As the EAS develops, the secondary charged particles, mostly electrons and positrons, excite the nitrogen molecules in the atmosphere, producing ultra-violet (UV) fluorescence photons. The term "fluorescence" photons in this context is a misnomer that stems from the common application of this effect in fluorescent lights. Fluorescence refers to the process where a higher energy photon is absorbed by an atom/molecule into a metastable state and then subsequently emitted as a lower energy photon. In fluorescent lights, an electron beam passes through mercury vapor to emit UV luminescence photons, which is absorbed by white phosphor coating the bulb and then emitted as white light. The "fluorescence" light initiated by EASs is mainly produced by the energy deposited by electrons/positrons from the air shower in inelastic collisions with air molecules. The misused analogy is that in both cases light is produced by charged particles in gas. Despite it being more accurate to refer to these photons that are produced in EASs as "luminescence" or "scintillation" photons, I will follow the analogy and refer to them as fluorescence photons. These photons are emitted isotropically with wavelengths between 290 – 430 nm. In addition to the nitrogen molecules' radiative de-excitation, a competing process known as quenching caused collisions with non-excited molecules in the air. Quenching refers to any process that decreases the fluorescence intensity. Figure 2.4 shows the nitrogen fluorescence spectrum measured by multiple experiments. There is general agreement between the different experiments on the fluorescence spectrum.

The ultra-relativistic particles in the shower also produce Cerenkov light as they pass through a medium at speeds faster than the speed of light in that medium. Cerenkov photons are beamed forward along the shower axis and emitted at an angle

$$\theta_c = \cos^{-1} \left(\frac{1}{n\beta} \right) \quad (2.21)$$

with respect to the charged particle, where n is the index of refraction of light and $\beta = v/c$. This component of emitted light accumulates along the shower trajectory, resulting in an

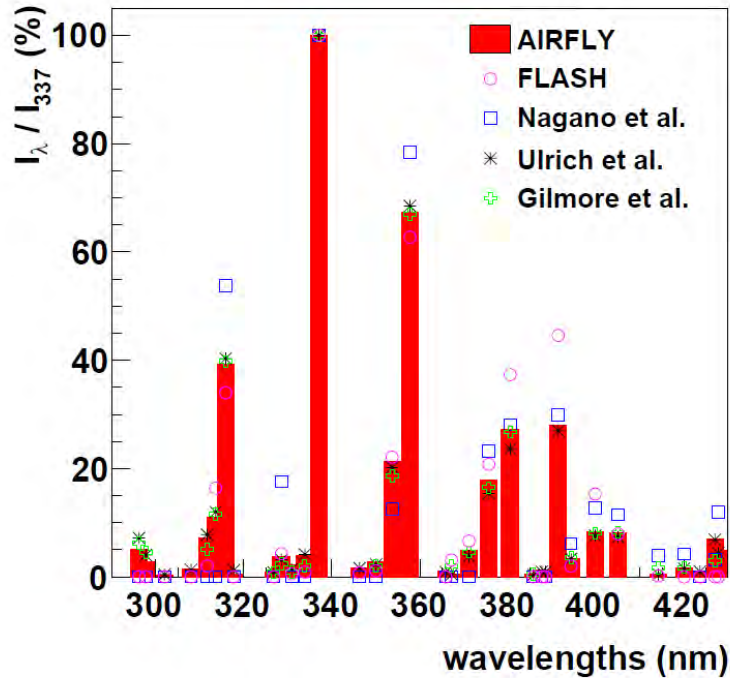


Figure 2.4: Relative fluorescence intensities of different experiments. The sum of the fluorescence yield in this wavelength range differs by 1.66% Ulrich et al., +2.08% Nagano et al., -1.7% FLASH, and -3.0% Gilmore et al. compared to the sum of the fluorescence yield obtained by AIRFLY. Gilmore et al. work's data points were calculated theoretically only for molecular nitrogen's emissions of the Second Positive (2P) system, a vibrational transition. Plot taken from Keilhauer et al. 2012 [22]

intense beam within a few degrees of the shower axis.

The fluorescence detection method primarily uses air fluorescence to measure the longitudinal development of an EAS. The energy of an EAS is inferred from the shower size, i.e., the amount of collected fluorescence light (Equation 4.1), after correcting for direct or scattered Cerenkov light. Section 4.2.3 describes the details of the calculations that are used in the data analysis.

CHAPTER 3

THE TELESCOPE ARRAY EXPERIMENT

As described in previous chapters, observing UHECRs indirectly through EASs requires an experiment to cover a large area to collect a sufficient number of cosmic rays at the highest energies to make statistically significant measurements. The Telescope Array (TA) experiment, seen in Figure 3.1, is the largest cosmic ray observatory in the Northern Hemisphere and is located in Millard County, Utah. TA was built by an international collaboration of universities and research institutions in the United States, Belgium, Japan, Russia, and South Korea. TA is designed to observe UHECRs with energies greater than 10^{18} eV using both fluorescence telescopes and scintillator surface detectors. This chapter will give a general description of the TA and its newest detector, TAx4. Then I will discuss both the TAx4 Fluorescence Detectors (FDs) and Surface Detectors (SDs) in detail, since they are used in conjunction for this dissertation's measurement of the cosmic ray energy spectrum in hybrid mode.

3.1 Overview of TA

TA is referred to as a hybrid detector because it uses information from the FDs and SDs to reconstruct cosmic ray events. Nitrogen molecules emit UV photons isotropically during the development of EASs and are detected by FDs at the periphery of the scintillator SD array. There are three telescope stations whose FDs' field of view overlook the SD array, thus allowing for coincident measurement of air showers by both. There is also overlap at the highest energies with one another to allow for stereo detection of UHECRs.

The Middle Drum (MD) station is located to the north, Black Rock (BR) to the southeast, and Long Ridge (LR) to the southwest of the SD array. MD consists of 14 telescopes repurposed from the High Resolution Fly's Eye (HiRes-I) experiment, while BR and LR each consist of 12 newly built telescopes for TA.

The scintillator SD array consists of 507 SDs and is shown in Figure 3.2. They are

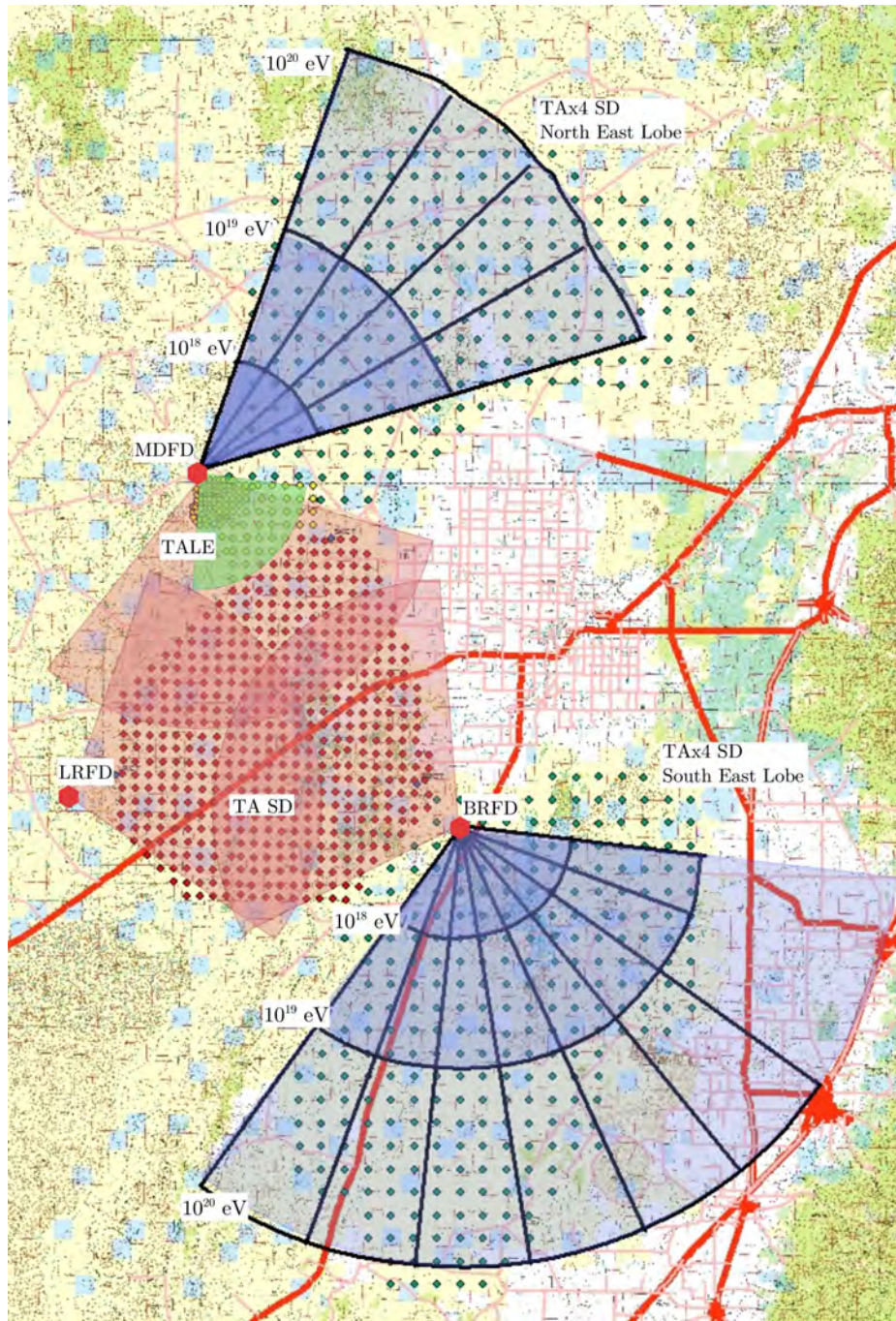


Figure 3.1: Map of TA. TAX4 SD sites are green dots, TA SDs are in red, and TALE SDs are in yellow. The approximate FOV of the FDs of TA is seen in red, TALE in green, and TAX4 in blue. Taken from G. Furlich Ph.D. thesis [13].

deployed in a square grid with 1.2 km spacing, covering an area of approximately 700 km². The SDs are used to sample the density of the shower particles that are produced in an EAS. Figure 3.3 shows a diagram of the inside of an SD. Each SD contains two layers of plastic scintillator material, 1.25 cm thick and 3 m². Embedded optical fibers transport the light to two PhotoMultiplier Tubes (PMTs), one for each scintillator layer.

In 2013, the Telescope Array Low Energy extension or TALE was added to extend TA’s energy range down to 10^{16} eV. TALE is also a hybrid detector and has an in-fill SD array of 103 counters arranged with spacing that increases with distance from the TALE FD. The TALE FDs were refurbished and upgraded from HiRes-II equipment and is located at the MD station. The TALE FDs view higher elevations ($31^\circ - 59^\circ$) in the sky because lower energy EASs reach their maximum development higher in the sky.

TA has found hints of anisotropy of UHECRs in the northern hemisphere, as discussed in Section 1.1.3. Using the TA SD data, there were 72 events found with $E > 57$ EeV (5.7×10^{19} eV) that showed a clustering of events with a 3.4σ significance. This clustering has been coined the *hotspot*. To better observe and understand the nature of the hotspot, TA is quadrupling its size. This expansion was accordingly named *TAX4*. TAX4 will increase TA’s detection aperture and increase the number of UHECR events detected. One of the primary goals of TAX4 is to improve the statistical significance of the hotspot and TA’s statistics overall at the highest energies.

3.2 TAX4 Fluorescence Detectors

Twelve new Fluorescence detector (FD) telescopes in total were added at the BR and MD FD station sites, four at MD and eight at BR. Figure 3.4 shows an aerial view of the MD and BR FD stations. TAX4MDFD, overlooking the TAX4 northern SD array, was completed in February of 2018; after several of months of detector commissioning, regular data-taking began. TAX4BRFD, overlooking the TAX4 southern SD array, was completed in July of 2019. Detector commissioning was extended because of the need to prepare this station for remote operation from Middle Drum. This effort was further delayed by the onset of the COVID-19 pandemic and the restrictions it imposed on work. Nevertheless, regular observation did start in July, 2020. In the following subsections, I will discuss in more detail various facets of the FD telescope system.

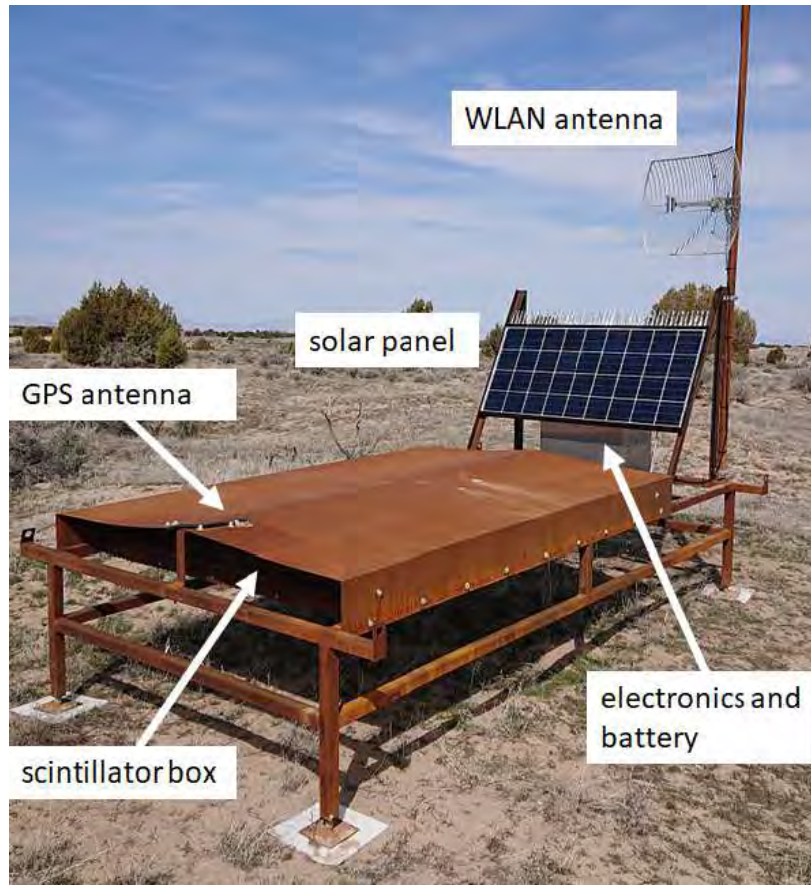


Figure 3.2: Photo of an SD used in the TA experiment (here, deployed for TAx4). The solar panel faces south, charging the battery in the stainless-steel box that supplies power to the electronics and other devices. The wireless LAN antenna is fixed to an antenna pole aiming at the communication tower, and a GPS antenna is placed on every SD for precise timing information. Taken from RU. Abbasi 2021 [5]

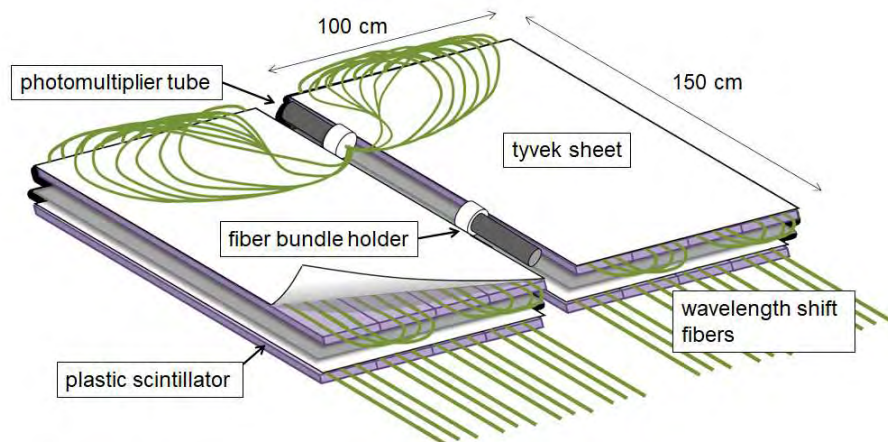


Figure 3.3: Schematic view of the SD's scintillator box. When charged particles pass through the plastic scintillator, it produces fluorescence light. This light is transported along the wavelength-shifting fibers (WLS) to the PMTs.



(a) TAx4MDFD



(b) TAx4BRFD

Figure 3.4: Aerial view of the TAx4 FD sites. (a) The northern FD site is located at the Middle Drum (MD) station. The MD station consists of three FDs: MD TA, TALE, and TAx4MD. (b) The southern FD site is located at the Black Rock (BR) station. The BR station has two FDs: BR TA and TAx4BR.

3.2.1 TAx4 Mirrors and PMTs

Each TAx4 FD telescope views $3^\circ - 17^\circ$ in elevation and a 15° span azimuth with a 1 square degree pixel size. These telescopes were refurbished from the HiRes experiment. The mirrors are composed of 4 spherical mirrors segments in a clover-leaf arrangement, giving a total collection area of about 5 m^2 , as seen in Figure 3.5a. Fluorescence light is focused on a flat 16x16 hexagonal PMT camera cluster, shown in Figure 3.5b. The focal-plane PMT camera consists of a closely packed 16x16 (256) cluster of hexagonal Philips XP3062/FL PMTs. The hexagonal tube shape was chosen in order to minimize the amount of dead space between PMTs. A full PMT package contains not only the photomultiplier tube but also a HV divider chain, a pre-amplifier, and an aluminum housing shown in Figure 3.6. These are 8-stage, linear-focused PMTs using a bi-alkali photocathode and borosilicate window. Both are designed to be sensitive to the range of 300-420 nm with a single photon time width of less than 2 ns [11]. Each camera is covered by a UV 300-420 nm passband filter.

For researchers to accurately understand the light produced by an EAS, both the systematic and optical effects like the reflectivity and curvature of the mirrors, the shadowing of the PMT cluster stand and shed doorway, the transmittance of the UV passband filter, the spacing and orientation of PMTs, and the quantum efficiency of the PMTs are included in both the detector simulation as well as in the event reconstruction codes.

3.2.2 Electronics and FADC Readout

Flash Analog Digital Converters (FADCs) are employed to read out the signal from the PMTs. The FADC system converts the continuous analog signal from the PMTs to digitized waveforms in a discrete-time series. The FADC system consists of 16 FADC boards that are monitored by a trigger-host board. Each FADC board reads out and digitizes the signal of each PMT in a vertical column of the PMT cluster. The FADC boards also perform a summation of the channels in the vertical columns and a summation of one of the rows in the PMT cluster. These summations are done twice with different gain values, once with a high gain and a low gain. The lower gain setting can provide a greater effective dynamic range in the case of saturation in individual PMTs. Thus each FADC has 20 channels: 16 PMT waveforms and four summations. The FADC converts the 16 PMT signal channels in



(a) Mirror composed of 4 segments.



(b) 16x16 PMT cluster camera with a UV bandpass filter.

Figure 3.5: TAx4 fluorescence telescope. (a) The mirror collects the fluorescence light generated in an EAS onto the PMT cluster camera. (b) The 16x16 PMT cluster camera covered with a UV bandpass filter.

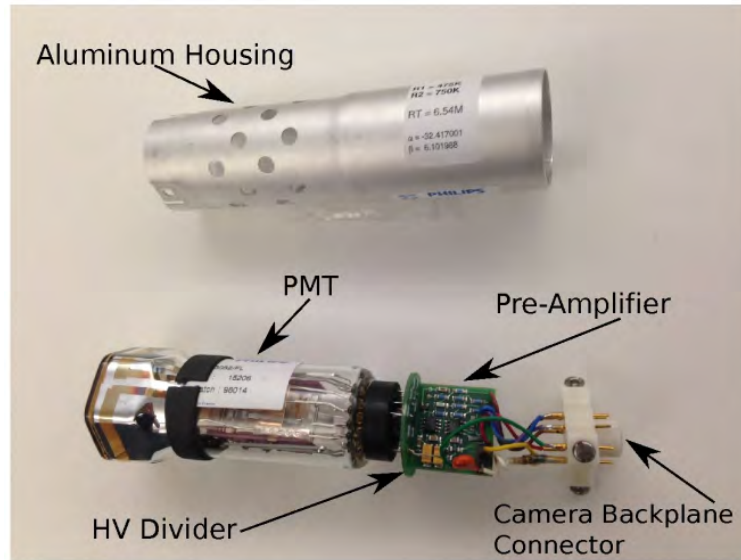


Figure 3.6: Philips XP3062/FL PMT Assembly Picture. This picture details the constituent parts of a PMT assembly. The entire assembly is housed within an aluminum shield. Taken from Z. Zundel Ph.D. thesis [33].

a column at a sampling rate of 10 Msps (100 ns time slices) and stores the output to an 820- μ s-long ring-buffer, which is designated M1. The high gain row and column summations channels are used as the input for the trigger logic. Any row or column summed to over 12 ADC counts (equivalent to 12 photons) is considered to be over the threshold. The trigger logic is described below in section 3.2.3.

In Figure 3.7, the front and back of the electronics racks are shown. These are controlled over Ethernet LAN. They provide, monitor, and control the HV and LV to the FADCs and the PMT cameras. The TAx4 FADC's are refurbished from the HiRes-II experiment, they control and readout from two telescopes packaged into a single rack. The racks link to a Central Timing (CT) module to obtain a common (10 MHz) clock. Each host/trigger board is also interfaced to a ARM-based processor running a Linux operating system (OS) which communicates with the main data acquisition (DAQ) computer over 100base-T Ethernet. Sensors in the electronics rack monitor the temperature and humidity within the rack and control a heat distribution system to keep the electronics from overheating. Each electronics rack controls two bay doors that open the telescopes to the night sky. A rain monitor is also installed on the back of each PMT cluster; if the rain sensor detects moisture, an automatic shutdown procedure is initiated that disables the HV and shuts the bay doors to protect the electronics.

3.2.3 Trigger

The TAx4 trigger condition for EAS tracks is the same as TALE's trigger condition. The trigger-host board contains four Programmable Logic Devices (PLDs) and a Digital Signal Processor (DSP). They scan the input trigger information for the row and column summations channels of the FADCs. The primary trigger condition is a three-fold coincidence in the vertical or horizontal summations, allowing for a skip of one. Figure 3.8 shows diagram of the three-fold coincidence triggering. Two of the four PLDs handle these calculations, one for the vertical sum channels and the other for the horizontal sum channels. These PLDs scan the channels sequentially in order to reconstruct the channel's position in the PMT cluster.

The PLD looks for a two-fold coincidence between a high value in one channel and a high value in at least one of the next two channels. The two-fold coincidence can be written

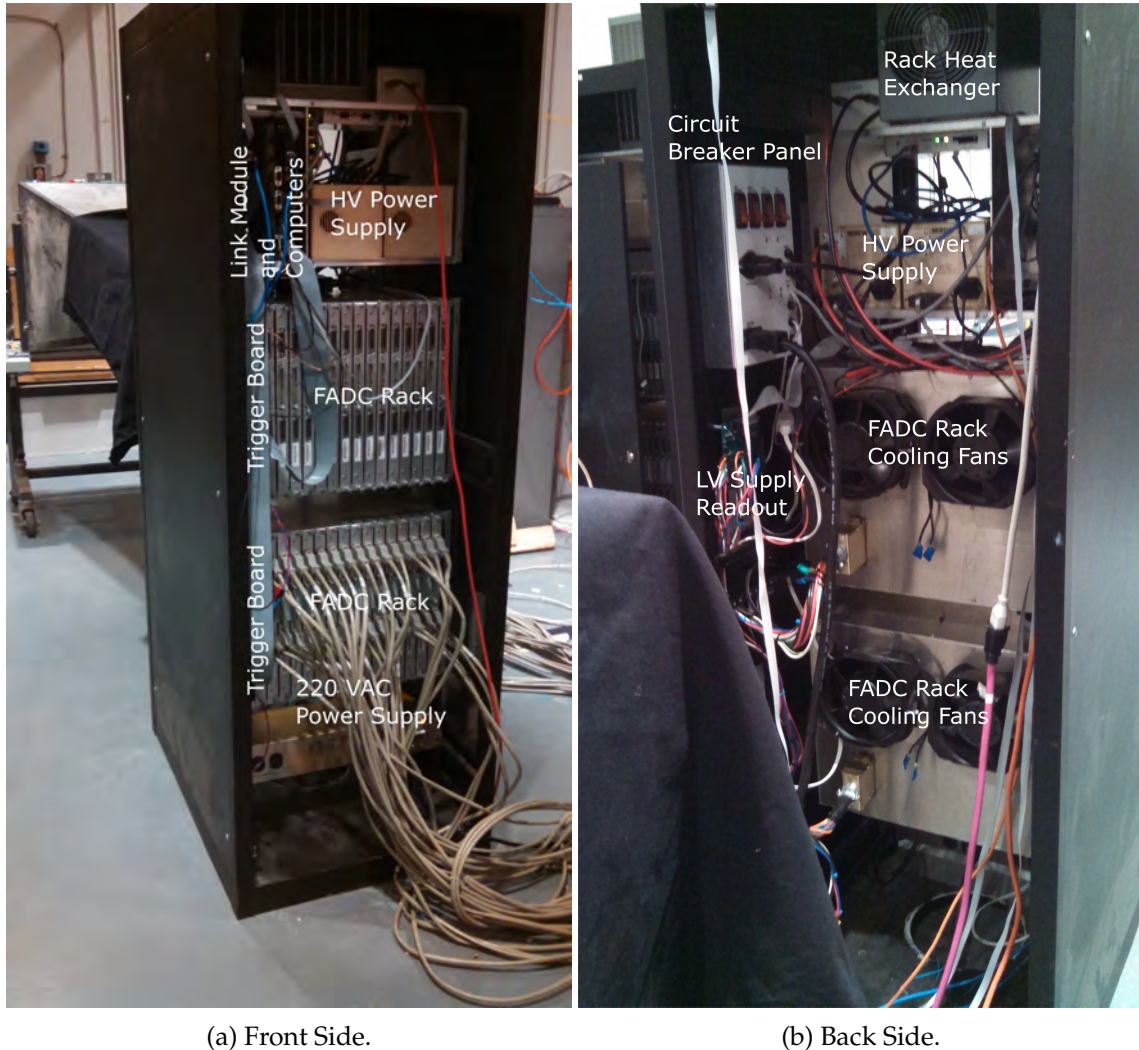


Figure 3.7: The TAx4 FADC electronics rack uses refurbished HiRes-II components. The components within the rack are labeled. Taken from G. Furlich's Ph.D. thesis [13].

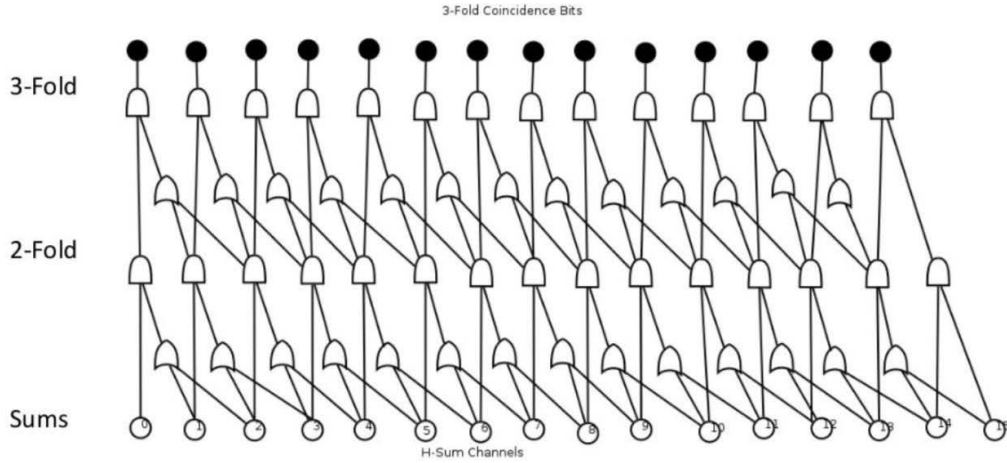


Figure 3.8: Diagram of the three-fold coincidence triggering in TAx4. Each signal sum starts with 16 signal sums and goes through logic operators to find two-fold coincidences. Fifteen signal sum channels of 2-fold coincidences go through more logical operators leaving 14 signal sum channels of 3-fold coincidences.

as a boolean equation for the i^{th} channel as:

$$2\text{Fold}_i = \text{Channel}_i \wedge \Delta(\text{Channel}_{i+1} \vee \text{Channel}_{i+2}) \quad (3.1)$$

where \wedge is the boolean AND operator, and the \vee is the boolean OR operator.

Next the 15 two-fold coincidence channels sums are checked for three-fold coincidences. The boolean equation for the i^{th} two fold coincidence channel is written as:

$$3\text{Fold}_i = 2\text{Fold}_i \wedge (2\text{Fold}_{i+1} \vee 2\text{Fold}_{i+2}) \quad (3.2)$$

After this logic operation, there are 14 signal sum channels for three-fold coincidences. These logical checks are in place to ensure that the candidate EAS track is long enough.

The trigger host board sends a store command to the FADC if the three-fold condition is met. This transfers data in M1 to another buffer called M2. The time window of the waveform is

$$2t_{coin} + 10\mu\text{s} \quad (3.3)$$

to a maximum of 200 μs where t_{coin} is the time difference between the three-fold coincidences. The M2 waveform is scanned for a signal above the threshold. If the FADCs finds a "track-like" series of PMT signals in space and time, the time corresponding to the start and stop of the signal and the integral of the FADC waveform are sent back to the trigger host board to be recorded.

The trigger system doesn't work well with events with vertical tracks. These events might only pass through one or two columns and will fail the three-fold coincidence condition described above, see Figure 3.9. A column thickener daughterboard, shown in Figure 3.11, was added to improve the detection of vertical tracks. It has two Complex Programmable Logic Devices (CPLD) that widen a single column high values into two columns. Each CPLD handles half of the 16 column channels before the three-fold coincidence check. One CPLD handles channels 0-7 but reads channel 8 to allow crossover. The second CPLD handles channels 8-15. The CPLD is programmed with three modes:

- **No thickening:** The CPLD leaves the column values unchanged. The boolean operation is written as

$$\text{Channel}_i^{out} = \text{Channel}_i^{in}. \quad (3.4)$$

- **Thicken all:** The CPLD thickens all high column values. The boolean operation is written as

$$\text{Channel}_i^{out} = \text{Channel}_i^{in} \vee \text{Channel}_{i+1}^{in}, \quad (3.5)$$

with the special case for channel 1 written as

$$\text{Channel}_1^{out} = \text{Channel}_0^{in} \vee \text{Channel}_1^{in} \vee \text{Channel}_2^{in}. \quad (3.6)$$

- **Hybrid:** The CPLD only thickens one high value channel only if the rest of the channels have low values. The boolean operation is written as

$$\text{Channel}_i^{out} = \text{Channel}_{i+1}^{out} = \text{Channel}_i^{in} \quad (3.7)$$

with the special case for channel 1 written as

$$\text{Channel}_1^{out} = \text{Channel}_0^{out} = \text{Channel}_1^{in}. \quad (3.8)$$

This upgrade was installed in May of 2019. Currently, the CPLD is running in the thicken-all mode.

The nearest neighbor trigger (inter-telescope) trigger upgrade was added to the detector in June of 2019. When a telescope generates a self trigger, its waveform that is saved to the M2 memory is analyzed to see if various conditions are met, indicating a continuation of the event onto another telescope, see Figure 3.10. Based on the scan results, the telescope

will either send out a Confirm or NoConfirm packet. The host computer receives the Confirm packets and re-sends them back to the neighboring telescope(s) to be written to their trigger boards. The corresponding waveform from M2 is recorded as well. This helps us not lose any small signals that appear in adjacent telescopes that may not have self-triggered.

3.2.4 Calibration

TAx4 uses an Ultra-Violet Light Emitting Diode (UVLED) for the photometric calibration of the PMTs. The UVLED module, shown in Figure 3.12, is placed at the center of each telescope to illuminate the PMT camera. The UVLED module is temperature stabilized to 45°C, then pulsed at 5 Hertz for 500 times at a wavelength of 355 nm. Using photon statistics, the variable gain amplifier attached to the PMT is adjusted so that all FADC channels have a nominal gain of one photoelectron per ADC count. The calibration is performed at the beginning and end of each night of observation with the doors closed to record the drift of the gain balance.

3.2.5 Operation Epochs

TAx4 data is split into three parts, or *epochs*, due to upgrades to the hardware and/or software changes. Each epoch is treated distinctly in the reconstruction and simulation of the data to reflect the conditions of the operating hardware and DAQ systems. These epochs are:

- **Epoch 0 (2018/06/08 - 2019/04/24):** The initial TAx4 FD epoch when it became operational and started collecting data every night.
- **Epoch I (2019/04/24 - 2019/06/08):** The column thickener daughter board was added to the trigger-host board for the four TAx4 telescopes at Middle Drum. The column thickener was set to the thicken all mode.
- **Epoch II (2019/06/26 - Present):** The current TAx4 FD epoch. The inter-mirror trigger was enabled in the TAx4 operations software.

Note that the eight TAx4 telescopes at Black Rock were fitted with the column thickening daughter boards before deployment. The work in this dissertation only analyzes data from

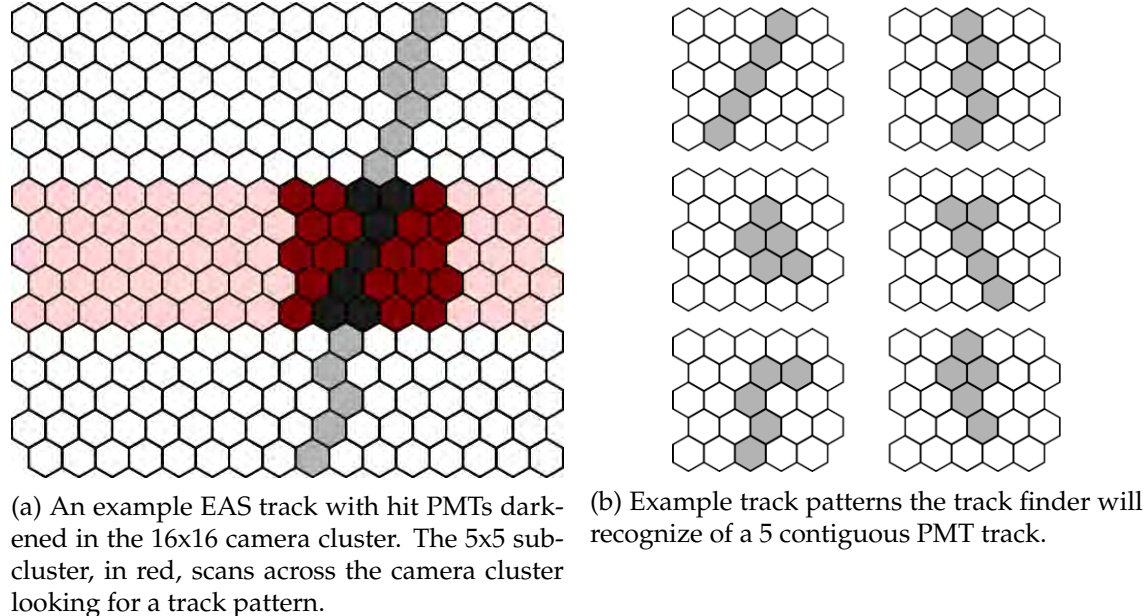


Figure 3.9: Vertical shower trigger code example and a subset of the possible track patterns found in the 5x5 sub-cluster. Taken from G. Furlich's Ph.D. thesis [13].

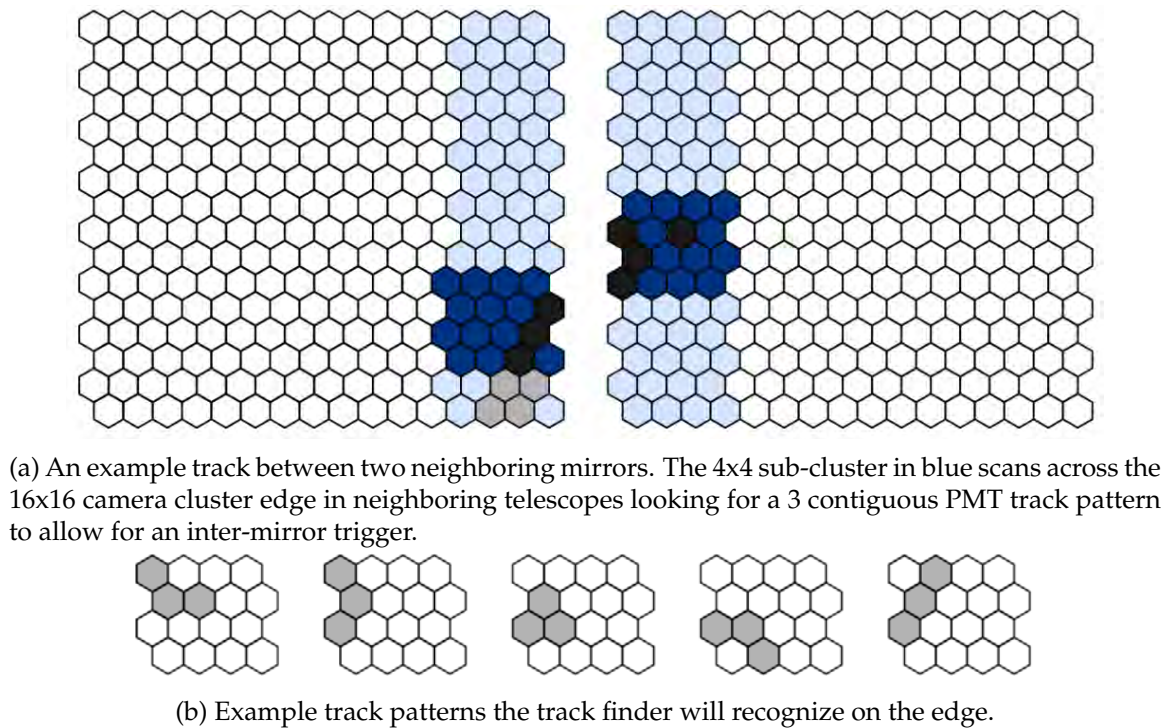


Figure 3.10: Inter-mirror trigger code example and a subset of the possible track patterns found in the 4x4 sub-cluster along the camera edge. Taken from G. Furlich's Ph.D. thesis [13].

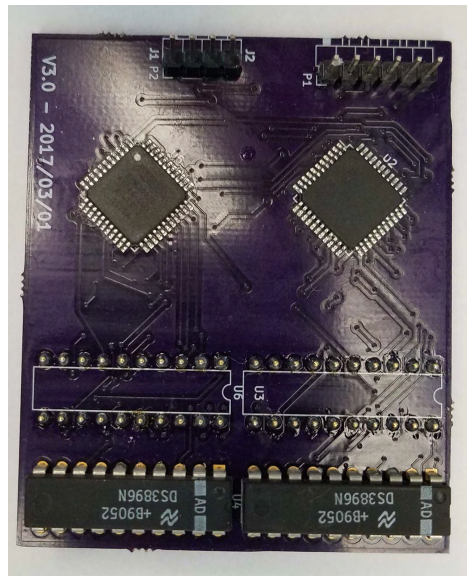


Figure 3.11: TAX4 FD trigger daughter board to recover near vertical EAS tracks.



Figure 3.12: The UVLED module mounted the center of telescope 25 of TAX4 North.

Epoch II after both the vertical shower and nearest neighbor trigger upgrades.

There have been several minor changes to the detector's timing and hybrid trigger, as discussed in Section 3.3.3, that don't merit a separate epoch but are important to consider during data analysis. The hybrid trigger gate width was widened to $128 \mu\text{s}$ from $32 \mu\text{s}$ for the SN and KM sub-arrays in March of 2020 and for the rest of the TAx4 sub-arrays in June of 2020. This change results in substantially more SD waveforms being recorded per event. Shortly after Epoch II began, it was found that there was a one integer second offset between the FD and SD event trigger times. In March 2020, a fix for this offset was applied to the hybrid trigger and TAx4 South FD trigger timing, but the fix wasn't enabled in the TAx4 North FD trigger timing until November 2020. This resulted in the hybrid triggers being sent to the SD array at the wrong time in the northern SD array; therefore, the TAx4 North hybrid trigger events during this period are excluded from my analysis. Table 3.1 shows a summary of these minor changes and their exact dates.

3.3 TAx4 Surface Detectors

TAx4 is in the process of quadrupling the area of the TA SDs by adding 507 SDs spread to the north and south of the main TA array. The two new TAx4 SD arrays can be seen in Figure 3.13. Currently, 257 of the planned 507 SDs are deployed. These SDs were deployed by helicopter in locations optimized for the detection of hybrid cosmic ray events. The deployment started in the early months of 2019, and data acquisition began in April of that year. The TAx4 arrays have been deployed with a 2.08 km spacing, a factor of $\sqrt{3}$ that of the 1.2 km for the original TA SDs. This arrangement is better for detecting cosmic rays with energies greater than $3 \times 10^{19} \text{ eV}$, while covering three times the detection area with

Date	Detector Changes
2018/06/08 - 2019/04/24	Epoch 0 - initial epoch
2019/04/24 - 2019/06/08	Epoch I - vertical shower trigger upgrade
2019/6/26 - Present	Epoch II - inter-mirror trigger upgrade
2020/3/3	Hybrid trigger trigger Gate Width SN and KM
2020/3/30	Hybrid trigger corrected for 1 integer second offset fix, resulting in it being sent to the SD at the wrong time
2020/6/6	Hybrid trigger Gate Width widened rest of SD sub arrays
2020/11/7	1 integer second offset fix enabled for FD timing

Table 3.1: Summary of the epochal and minor changes to the TAx4 detector.

the same number of detectors. In the following subsections, I will discuss in greater detail the TAx4 SDs.

3.3.1 Design

The basic design of the TAx4 SD is the same as that of a TA SD [7]. The essential component of an SD unit is a pair of plastic scintillator layers, each of 1.2 cm thick and 3 m² area. Each layer consists of eight 150 cm X 25 cm X 1.2 cm plastic scintillator sheets. The scintillation light from each layer is collected by 1 mm diameter wavelength shifting (WLS) fibers (Y-11 Kuraray S type [24]) and transported to the PMTs. The requirement of coincidence signals from both scintillation layers remove the low energy background and enhance the contribution of penetrating particles from extensive air showers.

The TAx4 SD electronics consists of a motherboard, a wireless LAN modem, and a charge controller. The motherboard includes electronics to read out signals, generate triggers, and communicate with a GPS receiver. The host electronics collect the data from each SD at its corresponding communication tower using 2.4 GHz wireless LAN communication. There are six of these communication towers, and each tower collects the data from a sub-array of SDs (Keg Mountain (KM), Desert Mountain (DM), Smelter North (SN), South Cricket (SC), Sand Ridge (SR), BR FD (BF)).

The TAx4 SDs differ in design from the original TA SDs in a few ways. The TAx4 wireless LAN module has a modified circuit to produce a more stable ADC baseline and added diodes to avoid excessively large signals. The wireless communication protocol was changed from the proprietary protocol to the standard User Datagram Protocol (UDP). This wireless communications system is similar to that used by the TALE SDs [27]. The TAx4 SDs uses 76% fewer WLS fibers than the TA SDs. The cost-saving modification was achieved by increasing by increasing the fiber spacing from 2 cm to 4 cm, the fiber length from 5 m to 6.1 m, and decreasing the number of fiber on each layer from 104 to 28. The TAx4 SD PMTs (R8619 Hamamatsu) have a higher quantum efficiency than the TA SDs PMTs. The plastic holder of the WLS fiber bundle attached to the PMT surface has also been changed from a transparent acrylic to a white polyacetal resin; this increased the number of photons incident on the PMT by 11% [6]. The WLS fiber bundle location in the holder has also been modified so that only the center of the photocathode of the PMTs is

used. As a result of these modifications, the average number of photoelectrons from the TAx4 SD PMTs is similar to that of the TA SD's PMTs.

3.3.2 Trigger

In both TA and TAx4 SDs, event triggering is accomplished by dividing the logic into three levels. The SDs use a 12-bit flash ADC to convert signals to ADC values every 20 ns to obtain waveforms. A threshold of 15 ADC counts corresponding to approximately 1/3 of the single-muon peak above baseline (the mode value of the 8 bin, 160 ns, sum of the ADC values in the previous second) constitutes a Level-0 trigger, which results in a window of 128 samples (i.e., 2.56 μ s) saved to a temporary buffer to be analyzed. If the saved window contains over 150 time-integrated ADC counts above baseline, then a Level-1 trigger is sent to the communication tower and onto the central computer for evaluation by a Level-2 trigger logic. The central computer searches for three adjacent Level-1 SD triggers within 14 μ s of one another, including those that cross the boundaries of the sub-arrays reporting to each tower. When this condition is met, the central computer passes a command to the SDs in a sub-array to record and transfer all Level-0 waveforms within $\pm 32 \mu$ s of the Level-2 trigger time. Figure 3.14 shows an example of a Level-2 SD event footprint and the detector's ADC waveforms.

3.3.3 Hybrid Trigger

In addition to the self triggering of the SD array as described above, the array can be triggered by the FDs via a *hybrid* trigger. The FD FADC event scans are analyzed to find the number of good PMTs, track length, and crossing time to determine if an event passes a set of conditions. Below is the minimum conditions need for a hybrid trigger:

- Event must be downward going (i.e., no upward going events from lasers, flashers, etc.).
- The number of good PMTs is ≥ 5 .
- The number of good PMTs per degree < 5.0 .
- All events that have a crossing time ≥ 500 ns, every 20th event if the crossing time is ≥ 200 ns, and every 200th event if the crossing time is < 200 ns.

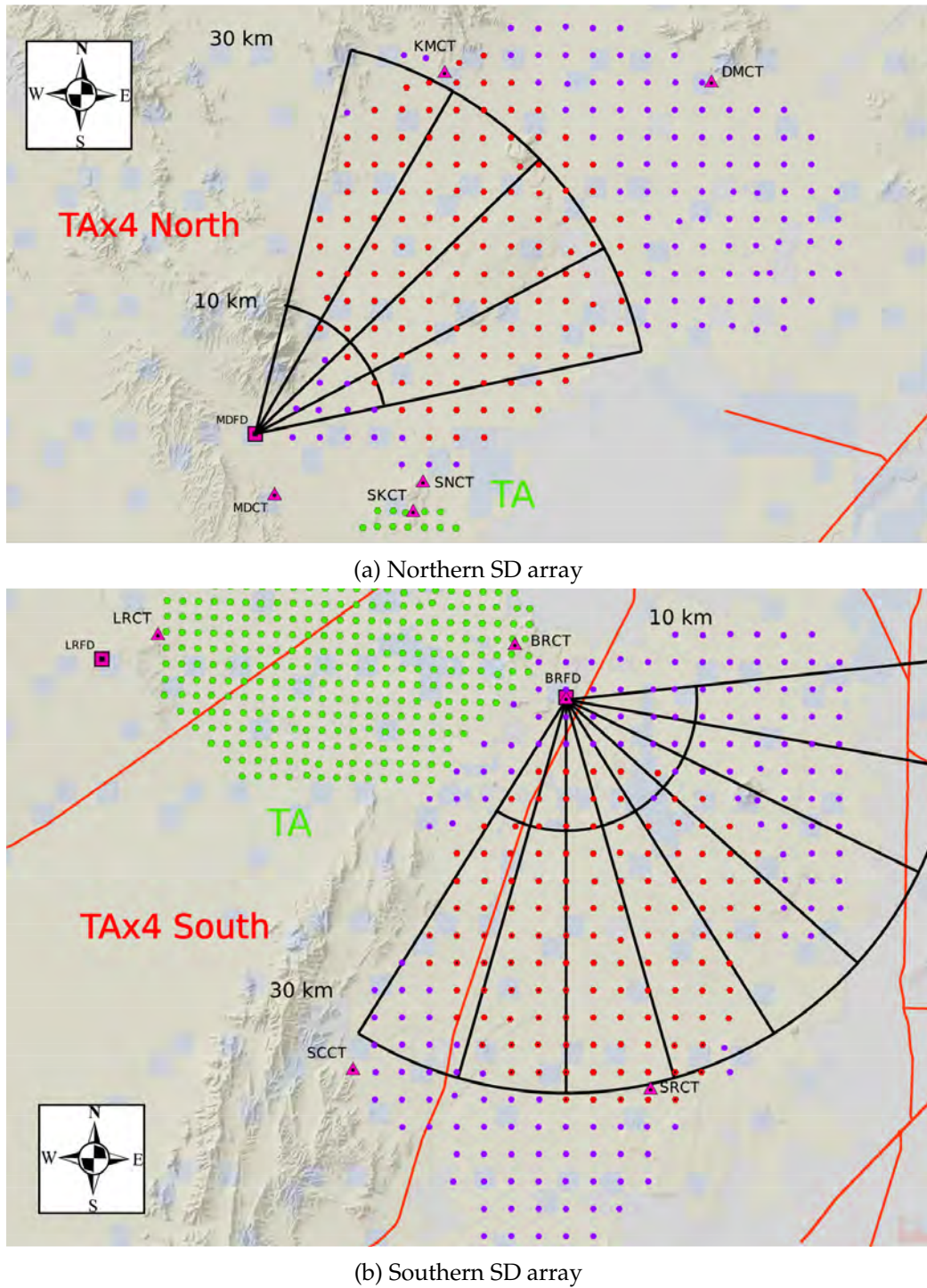


Figure 3.13: The TAx4 SD array plans to have 507 SDs with 2.08 km spacing. The red dots are the 257 deployed TAx4 SDs and the purple dots are the planned locations of the remaining 250 SDs. The triangles are the 6 SD communications towers: KM, DM, SN, SC, SR, BF. The squares show the FD station sites. The TAx4 sites show the FOV of each telescope.

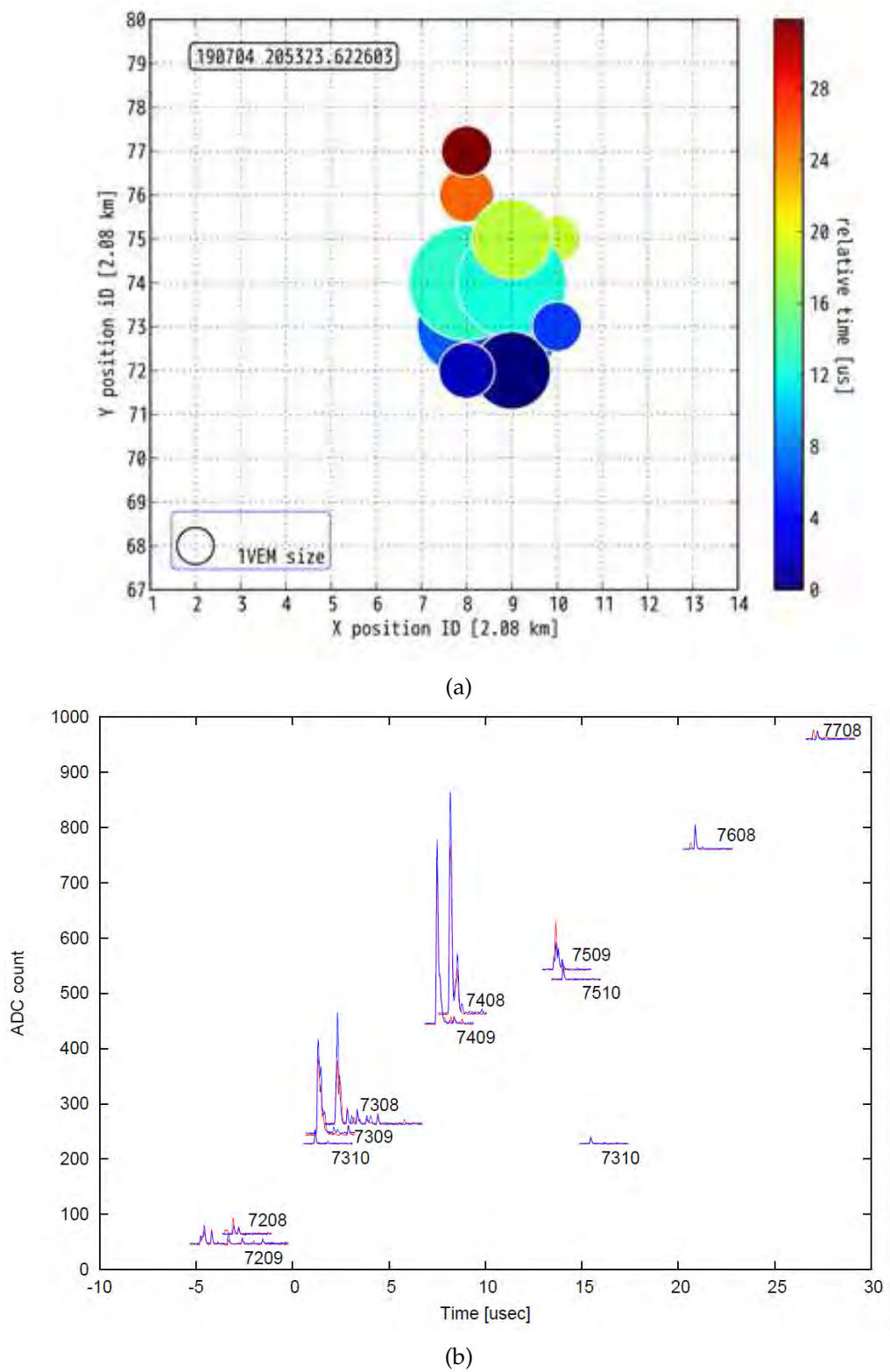


Figure 3.14: (top) TAx4 SD footprint of a detected air-shower event. The circle area corresponds to the logarithmic size of the signal. (bottom) Flash ADC waveforms of the SDs in the event. Plots taken from R.U. Abbasi 2021 [6].

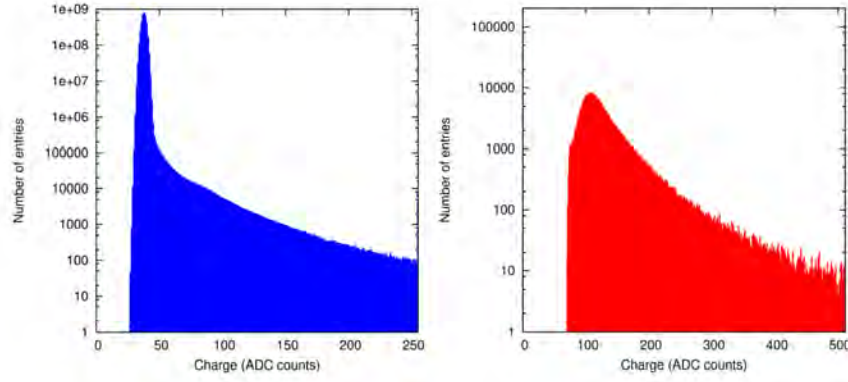


Figure 3.15: Left figure: A typical ADC distribution for the pedestal. The distribution was generated by integrating ADC values over 160 ns that were buffered for ten minutes. The tail of the histogram is from particle signals. Right figure: A sample of a typical ADC distribution for calibration with single muons. The distribution was generated by integrating ADC values over 240 ns that were buffered for ten minutes. Plots were taken from R.U. Abbasi 2021 [6].

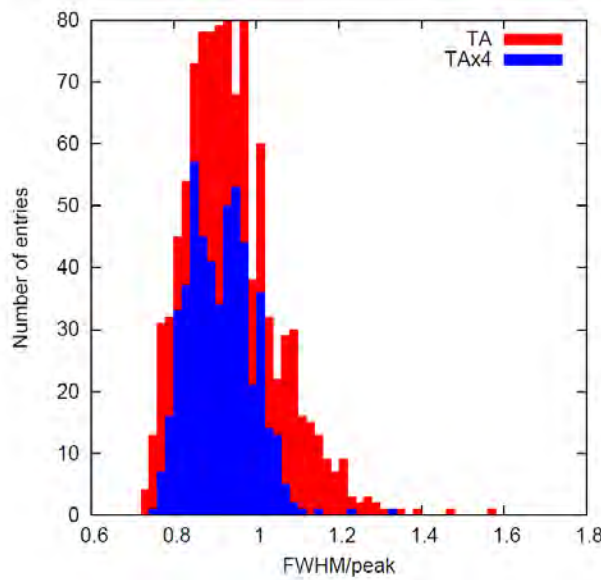


Figure 3.16: The distributions of the FWHM/peak of the ADC distributions of the TA and SDs. The mean FWHM/peak of the TA SDs is 0.94, with the RMS width 0.12. The mean FWHM/peak of the TAx4 SDs is 0.91, with the RMS width 0.08. The total number of entries of the TA SDs is 1014 (2 layers \times 507 SDs); that of the TAx4 SDs is 514 (2 layers \times 257 SDs). Plot taken from R.U. Abbasi 2021 [6].

When these minimum conditions are met a trigger packet is sent to the TAx4 SD sub-arrays to capture the footprint of the event. The hybrid triggering increases the trigger rate of the TAx4 SDs and enables them to capture lower energy events that wouldn't otherwise have induced a self trigger.

3.3.4 Calibration

Atmospheric muons provide a stable source for the calibration of the SDs. Using CORSIKA[12] to simulate low energy showers and using GEometry ANd Tracking (GEANT4 [31,32]) to simulate the energy deposition in the TAx4 SD scintillators, the average single muon was found to deposit 2.4 MeV [6]. The 12-bit flash ADC digitizes the waveforms from each PMT every 20 ns for twelve continuous-time slices, and then the ADC counts are integrated to obtain the single-muon peaks. A low-pass filter with a -3 dB cutoff frequency of 9.7 MHz is used to shape the analog signal. The left plot of Figure 3.15 shows an example of a typical ADC distribution of the pedestal, and the right plot shows a clear single-muon peak.

The uncertainty in the single-muon peak represents the primary statistical fluctuation in the number of photoelectrons from the photocathode of the PMT. The number of photoelectrons is given by

$$N_{pe} = N_\gamma \times \sigma_{qe} \times \sigma_{ce}, \quad (3.9)$$

where N_γ is the number of photons collected by the PMT, σ_{qe} is the quantum efficiency, and σ_{ce} is the collection efficiency [16]. The number of photoelectrons corresponding to the single-muon peak was measured using a gain of 5×10^6 . Despite the scintillator-box design changes, the TAx4 SD's number of photoelectrons corresponding to the single-muon peak is comparable to that of the TA SDs.

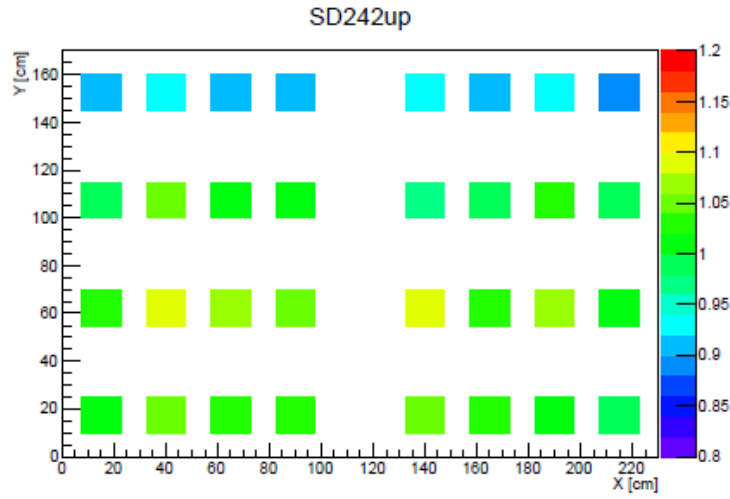
The single-muon peak was adjusted to approximately 50 ADC counts to equalize the signal response of the detectors after they were deployed. The distribution of the Full Width at Half Maximum (FWHM) of the ADC distribution of coincidence signals divided by the single-muon peak (FWHM/peak) of the same ADC distribution is seen in Figure 3.16. This is a direct measurement of the fluctuation of the peak. Since no TAx4 SD has a FWHM/peak outside of the distribution of the TA SDs, they can be operated in the same way as the original TA SDs. The mean of FWHM/peak for the TAx4 SD is 0.91, and the

mean of FWHM/peak for the TA SD is 0.94.

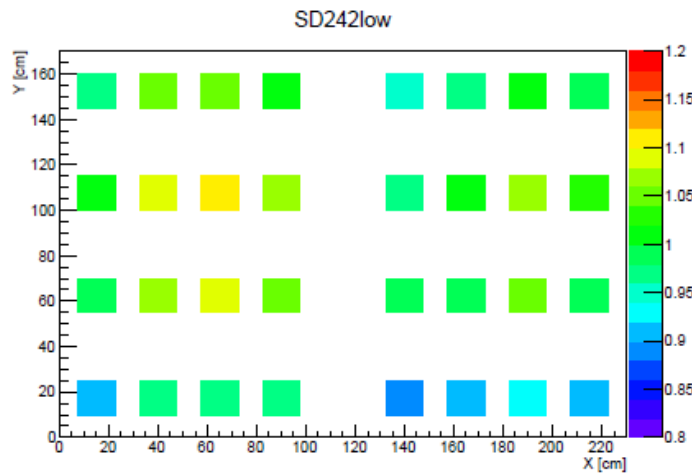
The positional dependence of the single-muon peaks was measured in the laboratory by placing trigger probes on the scintillator box of seven arbitrarily selected TAx4 SDs. The probes were placed such that approximately a quarter of each detector's area was covered. Figure 3.17 shows the position dependence of 32 single-muon peaks relative to the mean of the 32 peaks in each respective scintillation layer. The positional dependence of the single-muon peaks shows that a minimum occurs near the edge of the y-axis on each layer. This is the result of the attenuation length of the WLS fibers, which have opposing/complementary arrangements in the upper and lower layers. The WLS fibers here are bent with the smallest radius of curvature (12.5 cm) to lay them in the grooves (25 cm between grooves) of the scintillator surface. Figure 3.18 shows that the dependence of the single muon peaks on position for the TAx4 SDs is smaller than that for the original TA SDs, primarily because to the increased photon sensitivity of the new TAx4 SD PMTs and the new placement of fibers on the PMT face.

The nominally 50 MHz internal clock oscillators of each SD module differ from one another and are temperature-dependent in the actual frequency produced. To provide synchronization over the array and over long periods the internal clock of each SD is continuously calibrated using against the one pulse-per-second (PPS) signal from the GPS receiver (M12M i-Lotus) in the SD electronics. A test pulse is sent to the SDs from a function generator to verify the calibration accuracy. Using the SD electronics and GPS receiver with the serial number RD4569 as a standard reference, the relative difference in the trigger times was measured. Figure 3.19 shows the typical distribution of the trigger timing differences. The mean offset from the standard reference was -3.6 ns with an RMS width of 5.1 ns. The systematic uncertainty of the determination for the arrival direction caused by this offset is expected to be within 0.2 degrees, much smaller than the angular resolution of the TAx4 SDs (2.2 degrees). Therefore, it is adequate for TAx4 SD event reconstruction and doesn't require firmware adjustment.

The linearity of the PMT signals was measured after assembling the SDs. Each SD has four LEDs for calibrating the PMT linearity: two for the upper layer and two for the lower layer. The pulse linearity of all the PMTs was measured in the same way as the TA SDs. First, the PMT signal's pulse height, A , was measured by the flashing one LED.



(a) Upper scintillation layer.



(b) Lower scintillation layer.

Figure 3.17: Position dependence of the single-muon peaks for the upper layer of a typical surface detector. The colors represent the peak ADC values relative to the mean of the peaks in each respective layer. Plots taken from R.U. Abbasi 2021 [6].

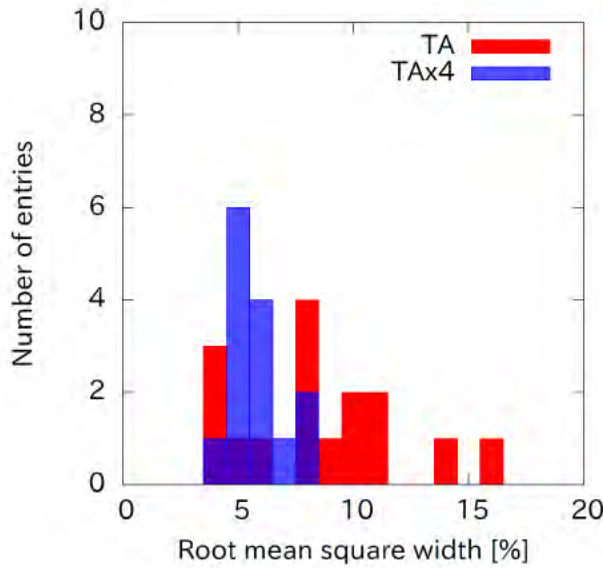


Figure 3.18: RMS widths of the position dependence of the single muon peaks relative to the mean peaks for the TA SDs and TAx4 SDs. Plots taken from R.U. Abbasi 2021 [6].

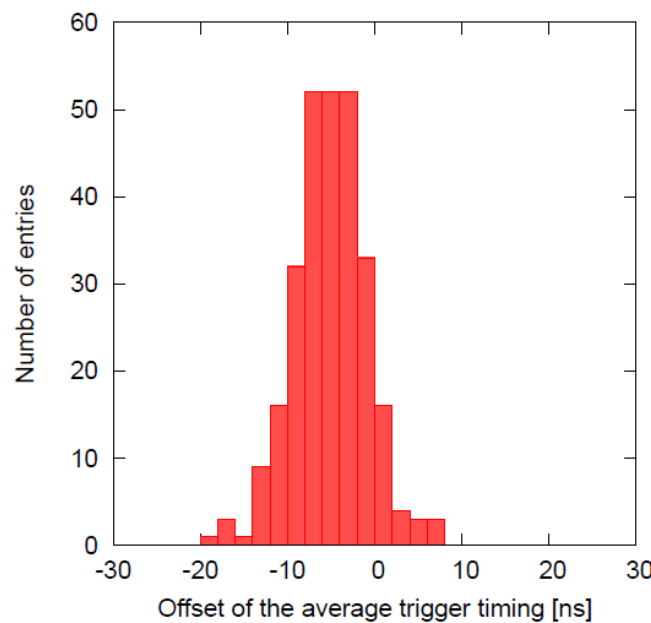


Figure 3.19: The distribution of the mean relative trigger timings of 374 different GPS receivers. The mean offset from the standard reference was -3.6 ns with a RMS width of 5.1 ns. Plots taken from R.U. Abbasi 2021 [6].

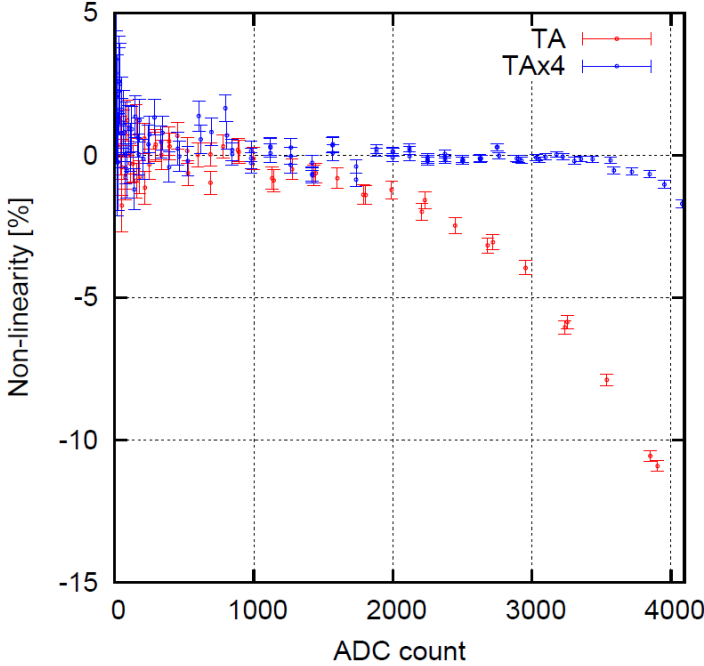


Figure 3.20: Non-linearity of typical photomultiplier tubes for the TA and TAx4 surface detectors, measured using the on board LEDs in the detector. Each ADC count corresponds to 0.01 mA. Plots taken from R.U. Abbasi 2021 [6].

Then the pulse height, B , of the PMT signal is measured by flashing the other LED. Finally, pulse height, C , was measured by flashing the two LEDs simultaneously. In the absence of non-linearity (as defined in Equation 3.10), one would expect $C = A + B$.

$$\frac{C - (A + B)}{A + B}. \quad (3.10)$$

The pulse heights are sampled every 20 ns and converted to ADC counts. Figure 3.20 shows the typical non-linearity results for the TA and TAx4 SDs. The TAx4 SD PMT non-linearity is within 5% for the entire range from 0 to 4095 ADC counts, in contrast with the TA SD PMTs non-linearity that is greater than 5% after 2930 ADC counts. When the PMT signals aren't linear, the signals are excluded from fitting the lateral distribution in event reconstruction.

CHAPTER 4

MONTE CARLO SIMULATION

For an accurate measurement of the flux of UHECRs, we must properly calculate the acceptance of our experiment. To this end, both a cosmic ray's interactions in the atmosphere and the detector's response must be simulated using the Monte Carlo (MC) Method. The development of the extensive air shower in the atmosphere is modeled by a simulation package called CORSIKA, which is discussed in Section 4.1. Combining CORSIKA with a detailed detector simulation allows for detector trigger efficiencies, acceptance, aperture, and reconstruction resolutions to be understood. These coupled simulations are intended to produce MC data that makes a faithful representation of the experimental data. The simulations include details that are important to the calculation of the exposure of the experiment. The MC events are then reconstructed using exactly the same procedure as the data. The validity of the MC can be determined by comparing distributions of reconstructed observables produced with the data to those from the MC. A full discussion on data-MC comparisons can be found in Section 6.2. Since this work concerns hybrid analysis, both FD and SD simulations are discussed below in Sections 4.2 and 4.3 respectively.

4.1 CORSIKA

CORSIKA (COsmic Ray Simulations for KAscade) is a complex MC program that can produce EAS simulations with any chemical composition and energy. A user is able to specify a number of parameters that control how the simulation develops an air shower (i.g., choice of hadronic interaction model), tracks particles, and monitors energy deposited in the atmosphere and on the ground. The program follows secondary particles, recording their positions, momentum vectors, particle type, and other parameters. These particles are tracked until a particle falls below a user-defined cutoff energy, where then CORSIKA tallies the energy deposition of the shower.

For cosmic rays above 10^{18} eV, the number of secondary particles becomes too numerous to record individually in practice, even with large cutoff energies. In fact, a single EAS produced by 10^{18} eV cosmic ray can take several days to simulate in standard CORSIKA. To mitigate this, CORSIKA has a statistical thinning option, where a single particle proxy is followed that represents many particles with a weight to conserve energy and momentum. This thinning option accepts parameter ϵ_{Th} , the thinning level. This quantity defaults to 10^{-6} . At any point during the EAS development, if the energy of the secondary particles falls below the thinning energy, $\epsilon_{Th}E_0$ (where E_0 is the primary energy), CORSIKA will combine the energies of the particles into a weight factor and track only one secondary particle. In this work, CORSIKA showers were generated using 10^{-5} eV thinning level.

While thinning the simulation reduces computation time significantly, it is at the cost of some information. Any amount of thinning level exaggerates the fluctuations in the particle densities away from the shower core where the particle densities are low. Figure 4.1a shows two lateral distributions of CORSIKA simulations, one using thinning and the other using no thinning. Despite the fluctuations, thinned showers work well in simulating air showers for FD simulations since the production of fluorescence photons depends only on the overall energy deposited. However, thinned showers in SD simulations can't be used directly because SDs measure the lateral distribution of particles. The TA collaboration has developed a "dethinning" technique, discussed in section 4.1.1, that recovers some of the information lost from thinning, allowing for the use of thinned showers in SD simulations.

4.1.1 Dethinning

Dethinning a CORSIKA simulation begins with selecting a weighted particle that reaches the ground. A vertex is chosen off the EAS axis that represents where the thinned particle was created. A two-dimensional Gaussian cone is constructed at the vertex, and the weights of the thinned CORSIKA particles are distributed randomly on the surface of the cone. An example of the vertex and resulting Gaussian cone used to spread the weighted particles can be seen in Figure 4.2.

Figure 4.1b shows the lateral distributions for a dethinmed and non-thinmed CORSIKA simulation. The dethinmed lateral distribution is in agreement with the non-thinmed lateral distribution.

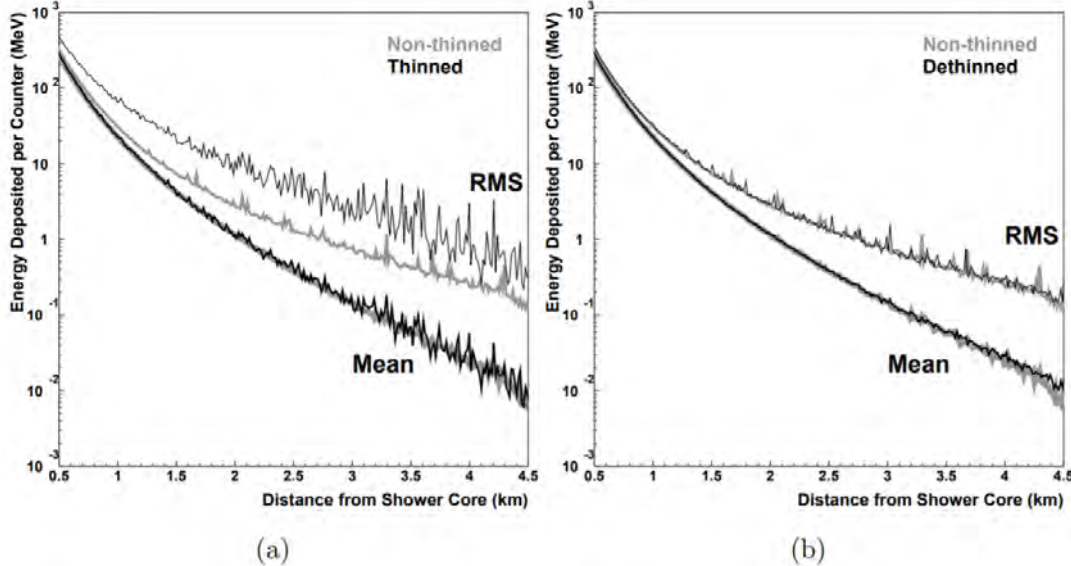


Figure 4.1: A comparison of energy deposition per counter versus perpendicular distance-to-core for a non-thinned and a thinned simulation before (a) and after (b) the dethinning procedure is applied. Both simulations are of a proton with a primary energy of 10^{19} eV and a primary zenith angle of 45° . While the mean energy deposition agrees in all cases, the variation in the energy deposition (RMS) shows much better agreement after dethinning. Plots were taken from M. Allen's Ph.D. Thesis [9]

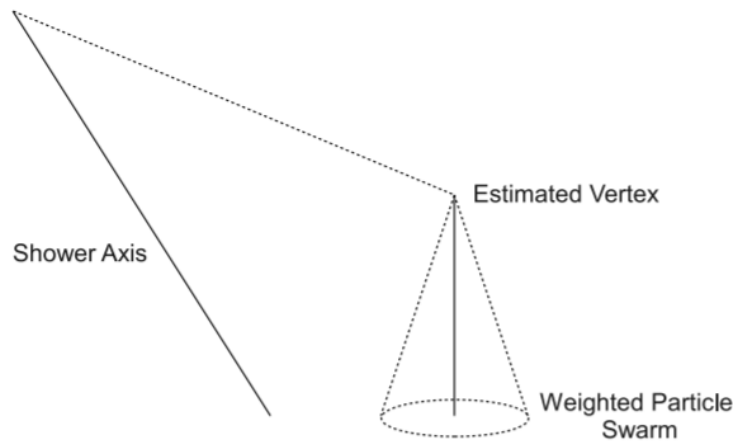


Figure 4.2: The basic geometries for distributing weighted particles from thinned CORSIKA showers in the dethinning process

4.2 Fluorescence Detector Simulation

The FD simulation is generated using the MC2K12 program, which is part of a set of software tools called *UTAFD*. The *UTAFD* software was primarily developed by T. AbuZayyad and is used for both FD event simulation and event reconstruction based on the TA programs established by D. Rodriguez [8, 29]. The MC2K12 program simulates events by sampling a library of CORSIKA generated showers based on a user-supplied input card. The light generated as the EAS propagates through the atmosphere and the detector response are both simulated. All the information generated by the program about the energy, size, shape (the so called Gaisser-Hillas [15]) parameters, unit vectors of the track and impact parameters, triggered mirrors and tubes, photoelectrons received by tubes per event, and timing of the shower are recorded in the MC04 DST bank.

4.2.1 Input

The MC2K12 program also accepts some twenty input parameters that determine how the events will be simulated and to facilitate book-keeping for the simulation effort. They are listed and described below, along with the values used for this work.

- **setNr** : 10 digit code that contains date information and data part number corresponding to actual experimental data.
- **use DB** : Select whether the calibration database will be used, YES OR NO. If YES, the UVLED tube gains and GDAS weather information are used for calibration. If NO, it uses nominal values for calibration. Set to YES.
- **isseed** : Random negative 9 digit seed number.
- **detector** : Detector configuration setting. If simulation is for TAx4 North this is set to ta_md_tax4.conf, for TAx4 South is set ta_br_tax4.conf.
- **shift origin** : Shift the event coordinates from the detector frame to the Central Laser Facility frame. Set to YES.
- **nevt** : The number of events to be simulated. This number is adjusted for the length of the data part.
- **event type** : Type of event to be generated. Set to SHOWER.

- **ipot_spectr** : Number of energy power law spectra to be simulated. Set to 1.
- **gamma** : The generated power law's spectral index. Set to 2 (i.e., we are generating a single E^{-2} spectrum to enhance the statistics at the higher energies).
- **minEnrgy** : Minimum shower energy in eV. Set to 1E+17 eV.
- **maxEnrgy** : Maximum shower energy in eV. Set to 1E+21 eV.
- **primary** : The hadronic model and chemical composition of the cosmic ray primary. Set to qgsjetii-03,proton.
- **rpmin** : Minimum impact parameter in meters. Set to 100 m.
- **rpmax** : Maximum impact parameter in meters. Set to 5E+4 m. (50 km)
- **thesh1** : Minimum zenith angle in radians. Set to 0.0.
- **thesh2** : Maximum zenith angle in radians. Set to $7\pi/18$ (70°).
- **phish1** : Minimum azimuthal angle in radians. Set to $-\pi$.
- **phish2** : Maximum azimuthal angle in radians. Set to π .
- **dxlim** : Limit of depth tracing in g/cm². Set to 2000.0.
- **hceil** : The atmospheric ceiling in meters. Set to 47000.0 m. (47 km)

An example input card for the MC2K12 program is shown on Table 4.1. An input card was created for every data part and input into the simulation program to produce the MC set.

4.2.2 Event Weighting

The MC was thrown as E^{-2} power law in order to increase the statistics of simulated events at the highest energies. However, in reality, the energy spectrum does not follow a simple power law. It has several spectral features such as the 2nd knee, ankle, and GZK cutoff, each with a different power-law exponent, see Table 4.2. I used the TA SD combined energy spectrum that was presented at the International Cosmic Ray Conference (ICRC) in 2019 as a spectral reference [20]. During the generation of the energy spectrum, the thrown MC events are weighted according to this spectrum, normalizing the flux at 10^{17} eV.

Example Input Card	
setNr:	2021020713
use DB:	YES
isseed	-621020713
detector:	ta_md.tax4.conf
shift origin:	YES
nevt:	50209
event type:	SHOWER
ipot_spectr:	1
gamma:	2
minEnrgy:	1E+17
maxEnrgy:	1E+21
primary:	qgsjetii-03,proton
rpmin:	100
rpmax:	50000
thresh1:	0.0
thresh2:	$7\pi/18$
phish1:	$-\pi$
phish2:	π
dxlim:	2000.0
hceil:	47000.0

Table 4.1: An example of an input card for the MC2K12 program. This input card was used in the simulation of data part 13 on 2021/02/07.

Spectral Feature	Energy Range	Spectral Index
2nd Knee	$10^{17.1} > E > 10^{18.65}$	-3.3
Ankle	$10^{18.65} > E > 10^{19.75}$	-2.7
GZK Cutoff	$E > 10^{19.75}$	-5.1

Table 4.2: Name, energy range, and spectral index of the features seen in ICRC 2019 TA combined energy spectrum [20]

4.2.3 Light Production

Two types of light are produced in an EAS, fluorescent and Cerenkov. Fluorescent light is emitted isotropically due to the interaction of the charged secondary particles and the nitrogen molecules in the atmosphere. This light has wavelengths between 290-420 nm and peaks in the spectrum at 337, 357, and 391 nm. The number of fluorescent photons produced per unit length per unit solid angle is given by,

$$\frac{d^2N_\gamma}{dld\Omega} = \frac{YN_e}{4\pi} \quad (4.1)$$

where Y is the fluorescent yield, and N_e is the number of electrons in the shower (Baltrusaitis et al. 1985). The measurement of the fluorescent yield is based on Kakimoto et al. 1996, and it is defined as the number of photons produced by a charged particle per meter of travel in the air. The measurement used electrons with energies 1.4 MeV, 300 MeV, 650 MeV, and 1000 MeV passing through the air at various temperatures and pressures to obtain the formula of fluorescent yield defined by,

$$Y = \frac{\left(\frac{dE}{dx}\right)}{\left(\frac{dE}{dx}\right)_{1.4\text{MeV}}} \rho \left[\frac{A_1}{1 + \rho B_1 \sqrt{t}} + \frac{A_2}{1 + \rho B_2 \sqrt{t}} \right] \quad (4.2)$$

where $\left(\frac{dE}{dx}\right)$ is the electron energy loss, $\left(\frac{dE}{dx}\right)_{1.4\text{MeV}}$ is the energy loss of electron having an initial energy of 1.4 MeV, ρ is the air density, t is temperature, and A_1, A_2, B_1, B_2 are constants. With this measurement, the systematic uncertainty in the energy determination of cosmic ray primaries improved from $\sim 30\%$ to $\sim 10\%$. The MC and reconstruction programs also take into account the small dependence on altitude.

Cerenkov light is emitted when a charged particles travels through the atmosphere above the local speed of light. This light is emitted in a narrow cone around the particles direction of travel and depends on the number of electrons with energies above the threshold energy for Cerenkov production. The number of Cerenkov photons produced per unit length is given by,

$$\frac{dN_\gamma}{dl} = \frac{2\pi\alpha}{c} \int d\nu \int_{E_t}^{\infty} dE f(E) \left(2\delta - \frac{m^2 c^4}{E^2} \right) \quad (4.3)$$

where α is the fine structure constant, ν is the frequency of the emitted radiation, and $f(E)$ is the electron energy distribution. The lower limit of the second integral is the threshold energy given as,

$$E_t = \frac{mc^2}{\sqrt{2\delta}} \quad (4.4)$$

where m is the electron mass, and $\delta = n - 1$, where n is the index of refraction in air. The electron energy distribution, $f(E)$, is defined by the integral relation,

$$F(E) = \int_E^{\infty} f(E') dE' \quad (4.5)$$

where $F(E)$ is the fraction of the electrons in the shower with energies greater than E ,

$$F(E) = \frac{34.8}{(40.4 + E)(1 + 10^{-4}E)^2} \quad (4.6)$$

where E is the electron energy. Using the approximation $m^2c^4 \ll E^2$, the number of Cerenkov photons produced per unit length simplifies to,

$$\frac{dN_\gamma}{dl} = 4\pi\alpha\delta F(E_t) \int \frac{dv}{c} \quad (4.7)$$

The angular distribution of Cerenkov photons is given by,

$$\frac{dN_\gamma}{dld\Omega} = \frac{dN_\gamma}{dl} \frac{e^{-\theta/\theta_0}}{2\pi \sin \theta} \quad (4.8)$$

where θ is the angle of the Cerenkov cone, and $\theta_0 = 0.83E_t^{-0.67}$ depends on the Cerenkov threshold energy, E_t .

4.2.4 Light Propagation

Both fluorescence and Cerenkov light suffer attenuation by scattering from the air molecules and aerosols, and from absorption by Ozone from the EAS to the detector. These attenuation factors are discussed in depth in section 4.2.4.1, 4.2.4.2, and 4.2.4.3, respectively. For each attenuation factor a transmission factor is calculated. The overall transmission factor, T , of a light beam propagating from the EAS to the detector is defined by,

$$T = T_R T_A T_{O_3}, \quad (4.9)$$

where T_R is Rayleigh transmission factor, T_A is the aerosol transmission factor, and T_{O_3} is the ozone transmission factor, see equations 4.12, 4.15, 4.17 respectively.

4.2.4.1 Rayleigh Scattering

Rayleigh scattering refers to the scattering of light by air molecules. The number of photons, N_γ , per unit length that are scattered is a strong function of the wavelength,

$$\frac{dN_\gamma}{dl} = -\rho \frac{N_\gamma}{x_R} \left(\frac{400}{\lambda} \right)^4, \quad (4.10)$$

where ρ is the atmospheric density and $x_R = 2970 \text{ g/cm}^2$ is the mean free path for scattering at 400 nm . The angular distribution (for unpolarized light) is given by,

$$\frac{d^2N_\gamma}{dld\Omega} = \frac{dN_\gamma}{dl} \frac{3}{16\pi} (1 + \cos^2 \theta), \quad (4.11)$$

where θ is the scattering angle.

The Rayleigh transmission factor, T_R , is given by,

$$T_R = \exp \left[\frac{-\Delta x}{x_R} \left(\frac{400}{\lambda} \right)^4 \right], \quad (4.12)$$

where Δx is the slant depth between the light source and the detector.

4.2.4.2 Aerosol Scattering

Aerosol scattering, modeled after Mie scattering, differs from Rayleigh scattering in a couple ways. The size of the scattering particles are significantly larger than the wavelength of light being scattered, and the particles have a variable distribution. This combined with the fact that concentrations of aerosols are not known and vary with location and time makes an analytic solution difficult. For this reason a simple parametric model is used, where the number of scattered photons per unit length is defined by,

$$\frac{dN_\gamma}{dl} = -\frac{N_\gamma}{L_M} \exp \left[\frac{-h}{H_M} \right], \quad (4.13)$$

where $L_M = 25$ km is the typical Mie scattering mean free path at the wavelength 360 nm, and $H_M = 1.0$ km is the scale height. The angular distribution of light scattered from the Cerenkov cone for angles between $5^\circ - 60^\circ$ is approximately,

$$\frac{d^2N_\gamma}{dl d\Omega} \simeq -\frac{dN_\gamma}{dl} 0.80 \exp \left[\frac{\theta}{\theta_M} \right], \quad (4.14)$$

where $\theta_M \simeq 26.7^\circ$.

The aerosol transmission factor, T_A , is given by,

$$T_A = \exp \left[\frac{-\Delta s}{L_M} \right], \quad (4.15)$$

where Δs is the reduced slant depth.

4.2.4.3 Ozone Absorption

Light attenuation due to Ozone absorption is given by,

$$\frac{dN_\gamma}{dl} = N_\gamma \rho_{O_3}(h) A_{O_3}(\lambda), \quad (4.16)$$

where A_{O_3} is an attenuation coefficient at a given wavelength, and ρ_{O_3} is the height-dependent ozone density.

Transmission through Ozone is treated in a similar way to scattering. The ozone transmission factor, T_{O_3} is given by,

$$T_{O_3} = \exp [-\Delta x_{O_3} A_{O_3}], \quad (4.17)$$

where Δx_{O_3} is the integrated ozone slant depth between the light source and the detector.

4.3 Surface Detector Simulation

The SD MC is added to the existing FD MC after it has been produced. This is done by the `t1_1sd_hy_simulation` program, which is part of a set of analysis tools called `tlanalysis` developed by D. Ivanov. As the name of the SD simulation program implies, this is a simple 1 SD MC; however, 4 SDs surrounding the shower axis are simulated for this purpose, allowing for a boundary cut later in the analysis. The program uses a reverse reconstruction technique to simulate the signals in the SD counters. Using the energy information in the MC04 DST bank, the S800 (SD energy estimator) for a given energy is calculated. From the S800, the full lateral profile of the event can be extracted, and once the lateral profile is known, then the signals in the SDs are known. These signals can then be simulated with a Poisson fluctuation using typical SD calibration values (the mean calibration values over all layers overall SDs in 2014/05/11). Then basic FADC traces can be constructed for four simulated SDs. This MC method was validated by showing that the resolutions from a full SD MC and this method roughly agree.

This SD simulation is incomplete in a two respects. First, the real-time calibration information isn't accounted for in the MC. Second, SD self trigger efficiency is set at 100%, when in reality sometimes the array won't trigger; however, the hybrid trigger, discussed in detail in Section 3.3.3, is assumed to be 100% efficient above $10^{18.5}$ eV and, we don't consider the SD self-trigger efficiencies for this analysis.

4.4 Monte Carlo Set

The MC2K12 program is used to generate the MC Set. Before generating a large set of MC events, the thrown distributions of energy, impact parameter, zenith angle, and azimuthal angle are compared with predicted theoretical distributions. These comparisons are discussed in more detail in Section 4.4.1. After verifying that the MC agrees with the predicted theoretical distributions, we generate a large MC set. The MC set consists of QGSJetII-03

protons thrown at energies between $10^{17} - 10^{21}$ eV with shower cores (point where the shower axis intersects the ground) distributed uniformly in a 50 km circle around the detector site. The MC set is then processed through the same reconstruction programs as the data, see Chapter 5. This simulated event set is used to determine the reconstruction resolution of the detector, see Section 4.4.2.

4.4.1 Thrown Distributions

The MC thrown distributions are intrinsically continuous, but in this work they are plotted in histograms. Each distribution is dependent on the total number of events simulated, N , the minimum and maximum limits simulated for that MC parameter, and the bin size of the histograms. Since the energy is thrown using the power law, $E^{-2.0}$, the energy distribution, Figure 4.3, is given by,

$$f(E_i) = \frac{N}{2(E_{\min}^{-1} - E_{\max}^{-1})} E_i^{-1} (10^{\Delta E} - 10^{-\Delta E}), \quad (4.18)$$

where E_{\min} is the minimum energy simulated; E_{\max} is the maximum energy simulated; E_i is the energy bin in a given histogram bin; and ΔE is the histogram bin size. The impact parameter is thrown uniformly inside a circle of radius $R_{p\max}$, and its impact parameter distribution, Figure 4.4, is given by,

$$f(R_{p_i}) = \frac{2N\Delta R_p}{(R_{p\max}^2 - R_{p\min}^2)} R_{p_i}, \quad (4.19)$$

where $R_{p\min}$ is the minimum distance simulated; $R_{p\max}$ is the maximum distance simulated; R_{p_i} is the impact parameter distance in a given histogram bin; and ΔR_p is the histogram bin size. The zenith angle is thrown using a $\sin \theta$ distribution, Figure 4.5, and is given by,

$$f(\theta_i) = \frac{2N}{1 - \cos \theta_{\max}} \sin \theta_i \sin \left(\frac{\Delta \theta}{2} \right), \quad (4.20)$$

where θ_{\max} is the maximum zenith angle simulated; θ_i is the zenith angle in a given histogram bin; and $\Delta \theta$ is the histogram bin size. The azimuthal angle is thrown using a flat distribution. The azimuth angle distribution, Figure 4.6, is given by,

$$f(\phi_i) = \frac{N}{i}, \quad (4.21)$$

where i is the total number of histogram bins.

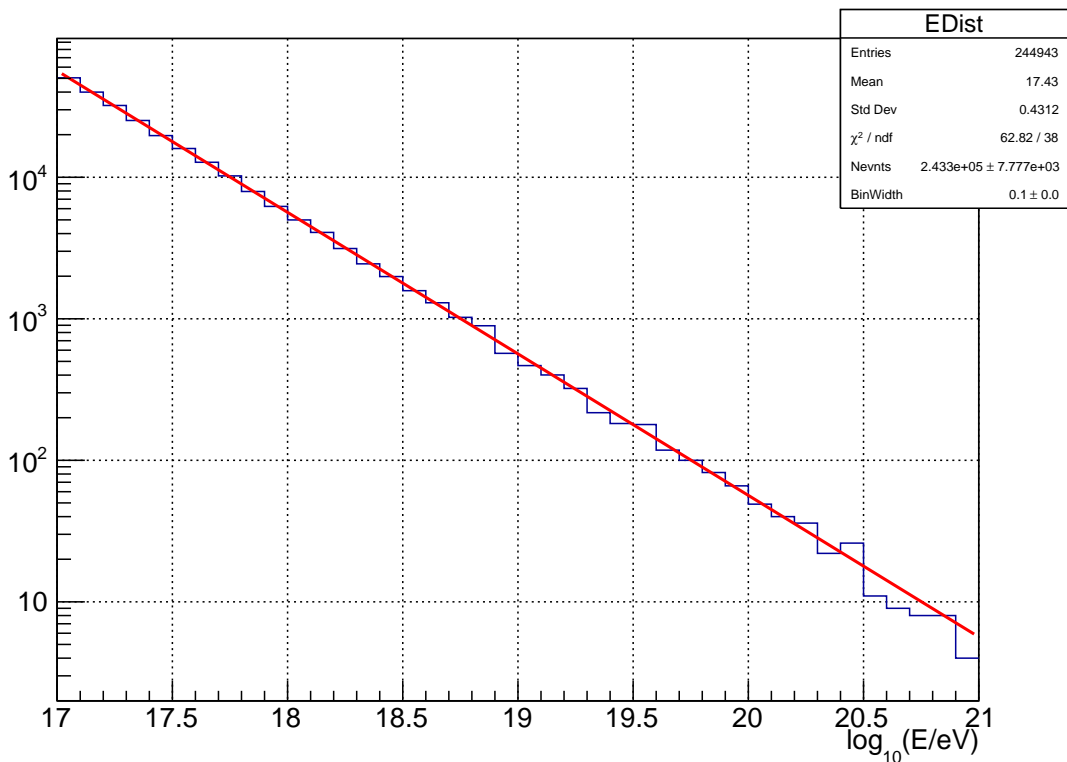


Figure 4.3: Thrown Energy Distribution. Blue histogram shows the thrown distribution. The red line shows the expected theoretical distribution, described by Equation 4.18, fitted to thrown the thrown data. The fit agrees with the number of events and the width of the histogram bins.

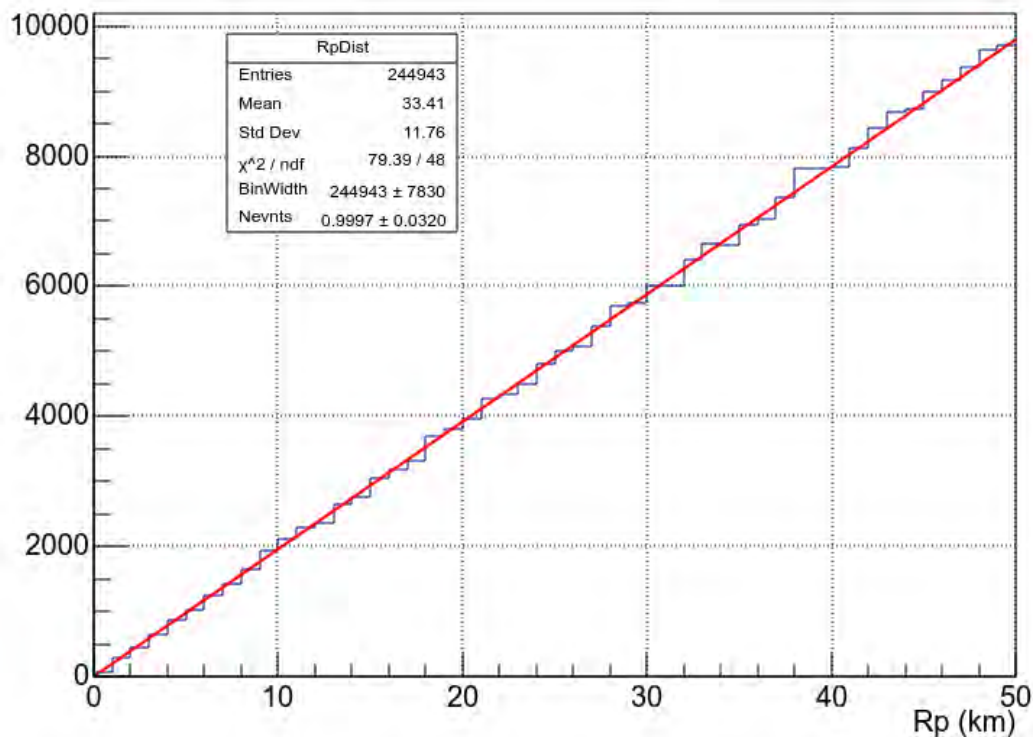


Figure 4.4: Thrown Impact Parameter (R_p) Distribution. Blue histogram shows the thrown distribution. The red line shows the expected theoretical distribution, described by Equation 4.19, fitted to thrown the thrown data. The fit agrees with the number of events and the width of the histogram bins.

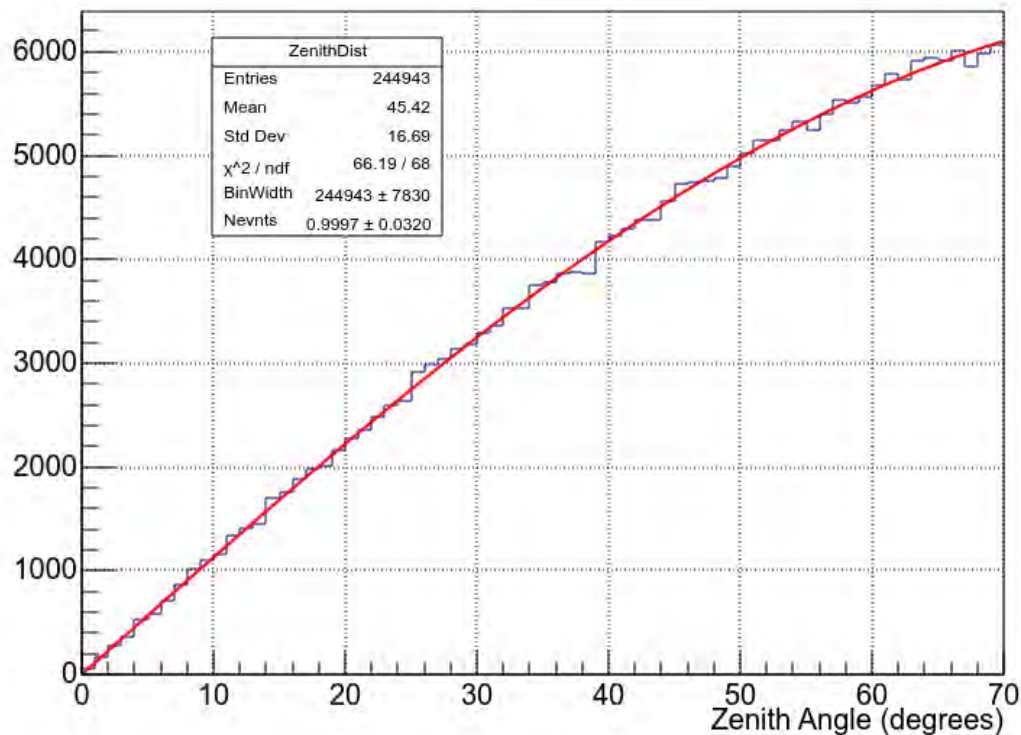


Figure 4.5: Thrown Zenith Angle (θ) Distribution. Blue histogram shows the thrown distribution. The red line shows the expected theoretical distribution, described by Equation 4.20, fitted to thrown the thrown data. The fit agrees with the number of events and the width of the histogram bins.

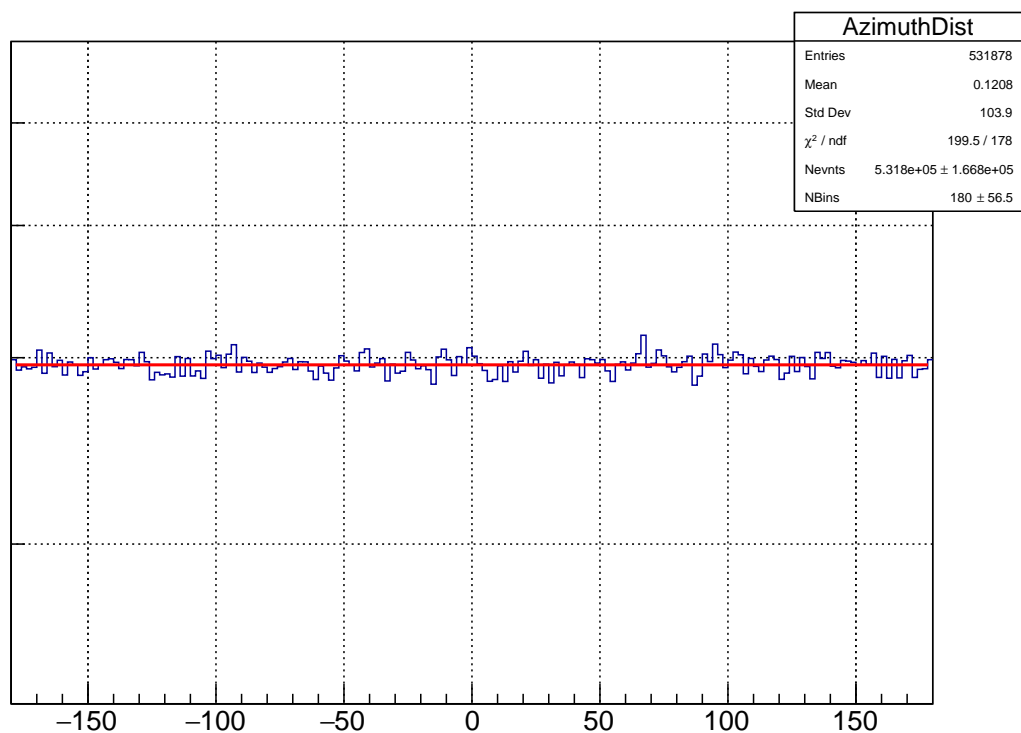


Figure 4.6: Thrown Azimuthal Angle (ϕ) Distribution. Blue histogram shows the thrown distribution. The red line shows the expected theoretical distribution, described by Equation 4.21, fitted to thrown the thrown data. The fit agrees with the number of events and number of histogram bins.

4.4.2 Resolution

MC events are reconstructed using the same code and process as the data, to be discussed in detail in chapter 5. To understand the resolution of event reconstruction, reconstructed parameters are compared to the parameters thrown in the MC. For each parameter, X , a histogram is made of the difference between the reconstructed and thrown values. For parameters whose reconstructed values span more than two orders of magnitude, such as energy or R_p , it is more appropriate to use percentage difference instead. In this work, the natural logarithm of the ratio is used to calculate the percent difference instead of the traditional formula for the percent difference. Equation 4.22 shows that to first order, these formulae are equivalent using a Taylor series expansion.

$$\ln\left(\frac{X_{\text{REC}}}{X_{\text{THR}}}\right) = \ln\left(1 + \frac{X_{\text{REC}} - X_{\text{THR}}}{X_{\text{THR}}}\right) \approx \frac{X_{\text{REC}} - X_{\text{THR}}}{X_{\text{THR}}} \quad (4.22)$$

The resolutions plot for TAx4 North are shown in Figures 4.7-4.11 (the resolutions of TAx4 South are similar). The width of the distributions measures the resolution and represents an average reconstruction precision. The mean of these distributions is referred to as the reconstruction bias and is the average amount that a parameter is systematically misreconstructed. A Gaussian is fitted to the distribution for each reconstructed parameter, and the fit parameters are used to determine the resolution and reconstruction bias. Additionally, a two-dimensional histogram of the parameter's resolution plotted as a function of energy, where color indicates the number of events, is overlaid with a profile plot fitted with a line fit. This work examines the following reconstructed parameters: energy, zenith angle, in-plane angle, impact parameter, and X_{max} .

Figure 4.7a shows the energy resolution histogram by evaluating $\ln\left(\frac{E_{\text{REC}}}{E_{\text{THR}}}\right)$. The mean value of the histogram is centered at 2%, which means there is a small energy bias is observed, and the spread of the distribution is about 9.3%. The bias of the energy resolution as a function of energy is shown in Figure 4.7b. It shows that the bias does change as a function of energy, but these biases average out to approximately 0 over the energy range of this work.

Figure 4.8a shows the zenith angle, θ , resolution histogram by evaluating $\theta_{\text{REC}} - \theta_{\text{THR}}$. The mean value of the histogram is centered at 0.3 degrees, and the spread of the distribu-

Parameter	Monocular Resolution	Hybrid Resolution
Energy, E	19.93%	9.2%
Zenith Angle, θ	3.03°	0.8°
In-plane Angle, ψ	6.98°	0.9°
Impact Parameter, R_p	10.68%	0.7%
Depth of Shower Maximum, X_{\max}	85.56 g/cm^2	35 g/cm^2

Table 4.3: TAx4 resolution comparison between TAx4 in monocular and hybrid mode. TAx4 monocular resolutions taken from my ICRC(2019) proceeding [28]

tion is slightly less than a degree. The bias of the zenith angle resolution remains constant in this works energy range, shown in Figure 4.8b.

Figure 4.9a shows the in-plane angle, ψ , resolution histogram by evaluating $\psi_{\text{REC}} - \psi_{\text{THR}}$. The mean value of the histogram is centered 0.8, which means there is a small amount of ψ bias observed, and the spread of the distribution is slightly less than a degree. The bias of the zenith angle resolution remains constant in this work's energy range, shown in Figure 4.9b.

Figure 4.10a shows the impact parameter, R_p , resolution histogram by evaluating $\ln\left(\frac{R_p,\text{REC}}{R_p,\text{THR}}\right)$. The mean value of the histogram is centered at 0, which means no R_p bias is observed, and the spread of the distribution is 0.7%. The bias of the R_p resolution remains constant until $10^{19.9}$ eV. Beyond this energy the reconstructed R_p is less than the thrown value meaning it is "under-reconstructed." This is likely the result of the limited extent of the current SD array so that at the highest energies, the reconstruction of events thrown at or beyond the edge of the SD are biased towards the edge of the SD array. Which represents a smaller R_p value.

Figure 4.11a shows the X_{\max} resolution histogram by evaluating $X_{\max,\text{REC}} - X_{\max,\text{THR}}$. The mean value of the histogram is centered at -15.2 g/cm^2 , which means there is a slight bias in X_{\max} , and the spread of the distribution is 35 g/cm^2 . The bias of the X_{\max} resolution remains constant in this works energy range, shown in Figure 4.11b. The resolution of X_{\max} could be improved by adding a bracketing cut (X_{\max} is seen by the FDs), but since this work is focused on the energy spectrum, not composition, this cut has been removed to increase hybrid event statistics.

Table 4.3 shows a summary of the TAx4 monocular resolutions, from my ICRC(2019) proceeding [28], compared to that of the hybrid resolutions. The hybrid resolutions are

smaller than the monocular resolutions, indicating better reconstruction of cosmic ray events. The hybrid resolutions are similar to Dr. M. Allen's TA hybrid analysis of the MD detector [9], but the resolutions are approximately twice as large. This can be understood by considering MD is a "two-ring" detector (pairs of FD telescopes view two separate elevations at the same azimuth), while TAx4 is a "one-ring" detector (all FD telescopes view the same elevation). This work's resolutions show that the reconstruction program reconstructs parameters reasonably well.

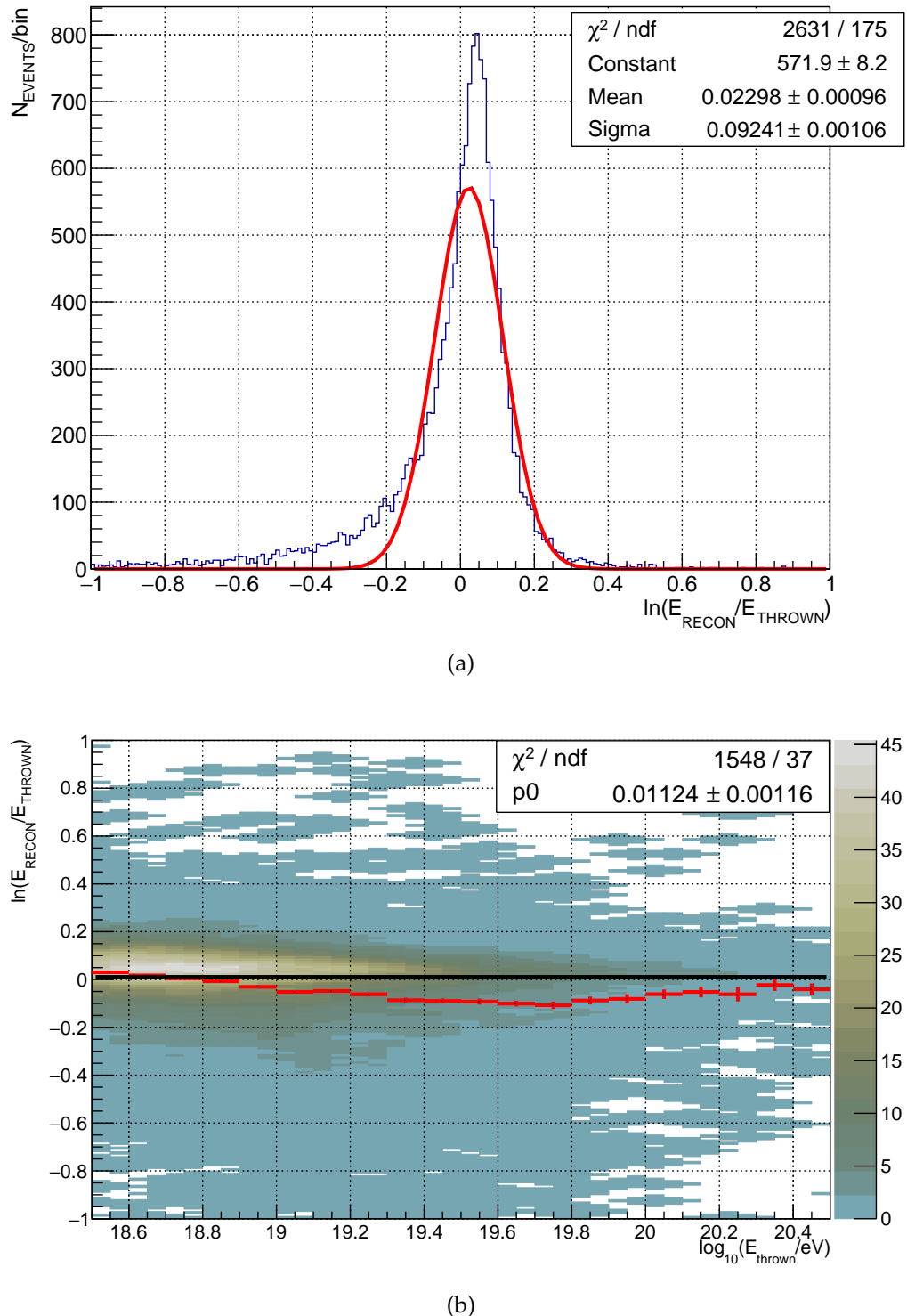


Figure 4.7: The energy resolution histogram and energy resolution as a function of energy. (a) The energy resolution histogram. The red line is a Gaussian fit of the histogram. The fit parameters are displayed in the statistics box. (b) The energy resolution as a function of energy.

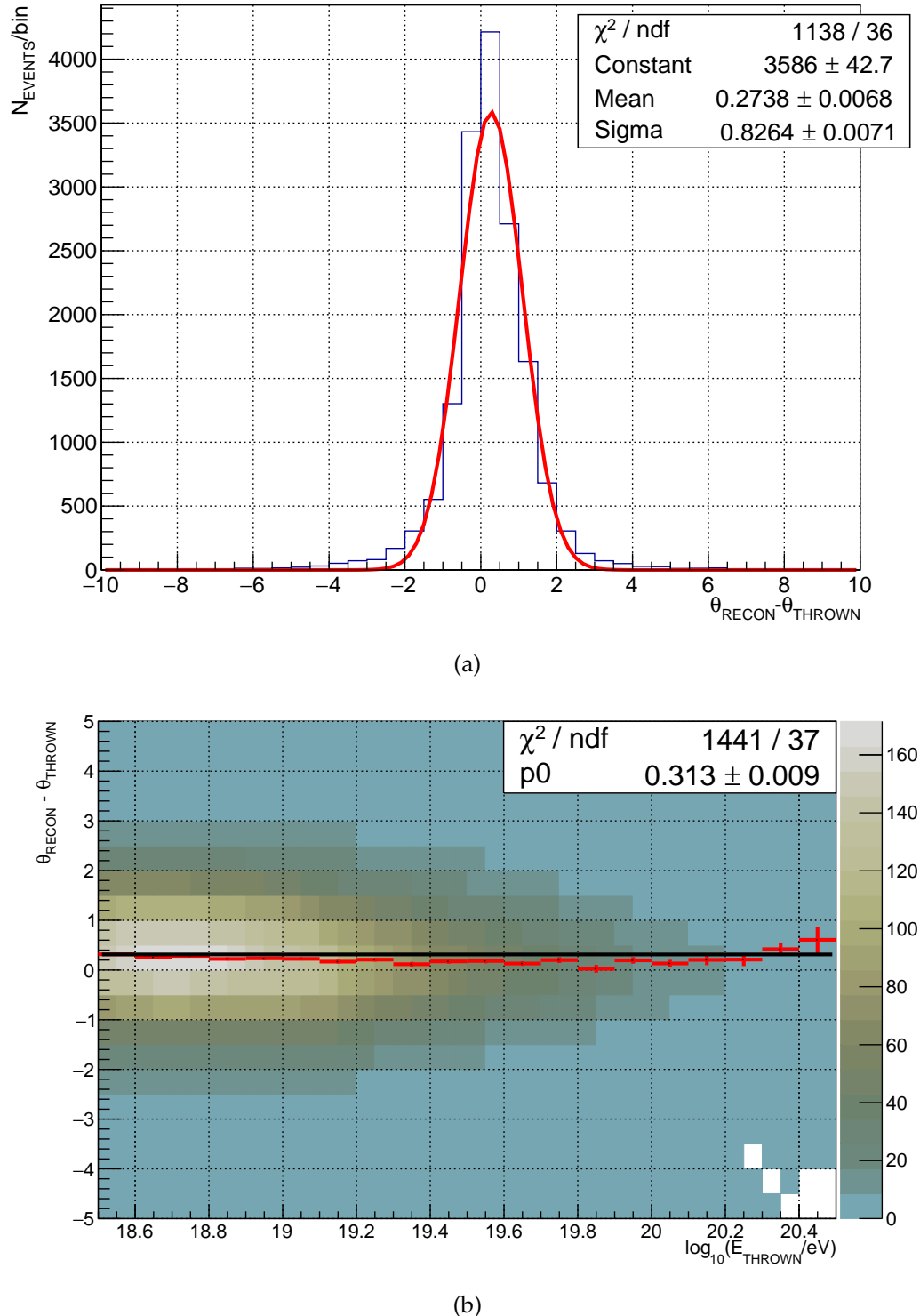


Figure 4.8: The zenith angle resolution histogram and zenith angle resolution as a function of energy. (a) The zenith angle resolution histogram. The red line is a Gaussian fit of the histogram. The fit parameters are displayed in the statistics box. (b) The zenith angle resolution as a function of energy.

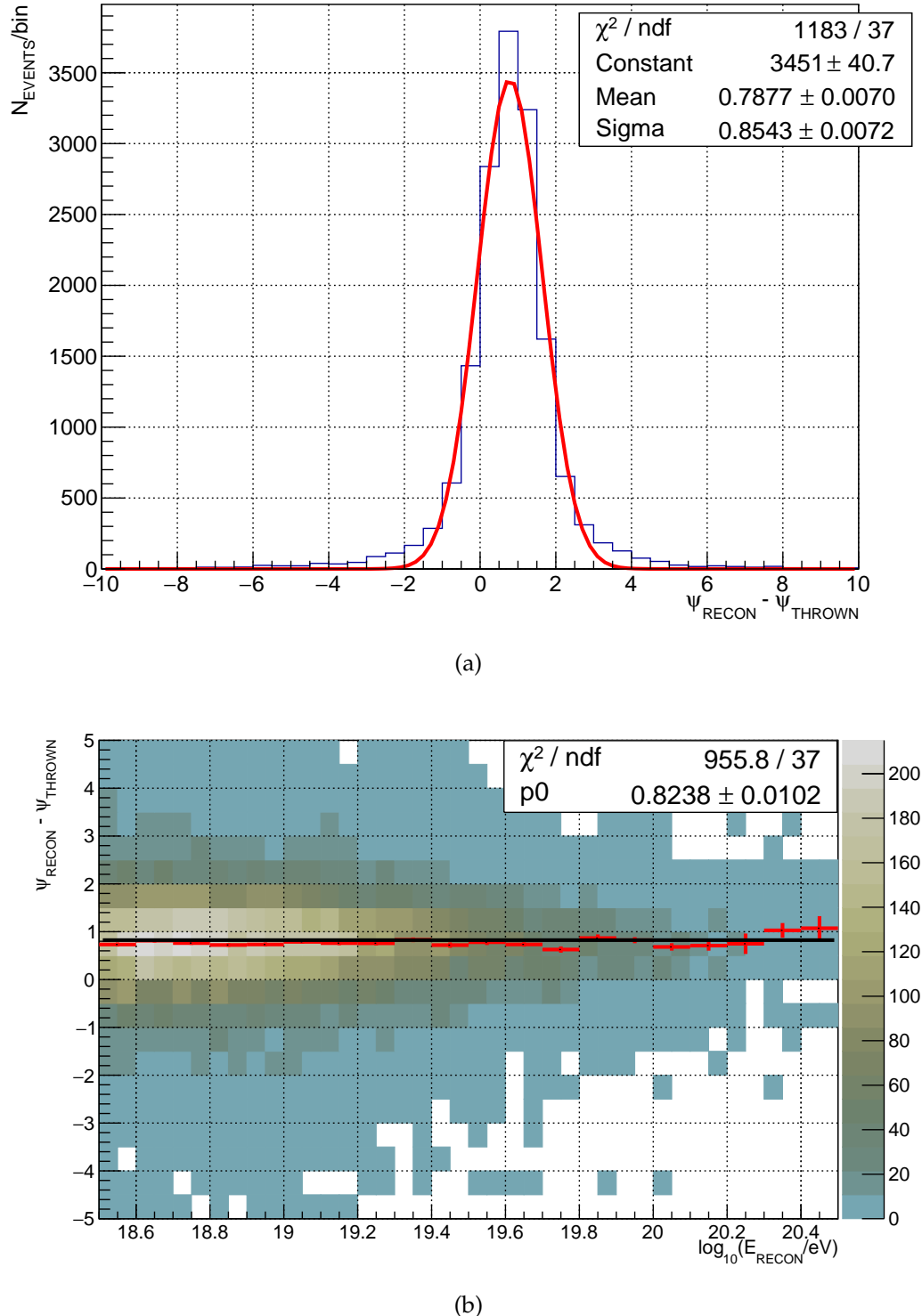


Figure 4.9: The in-plane angle resolution histogram and in-plane angle resolution as a function of energy. (a) The in-plane angle resolution histogram. The red line is a Gaussian fit of the histogram. The fit parameters are displayed in the statistics box. (b) The in-plane angle resolution as a function of energy.

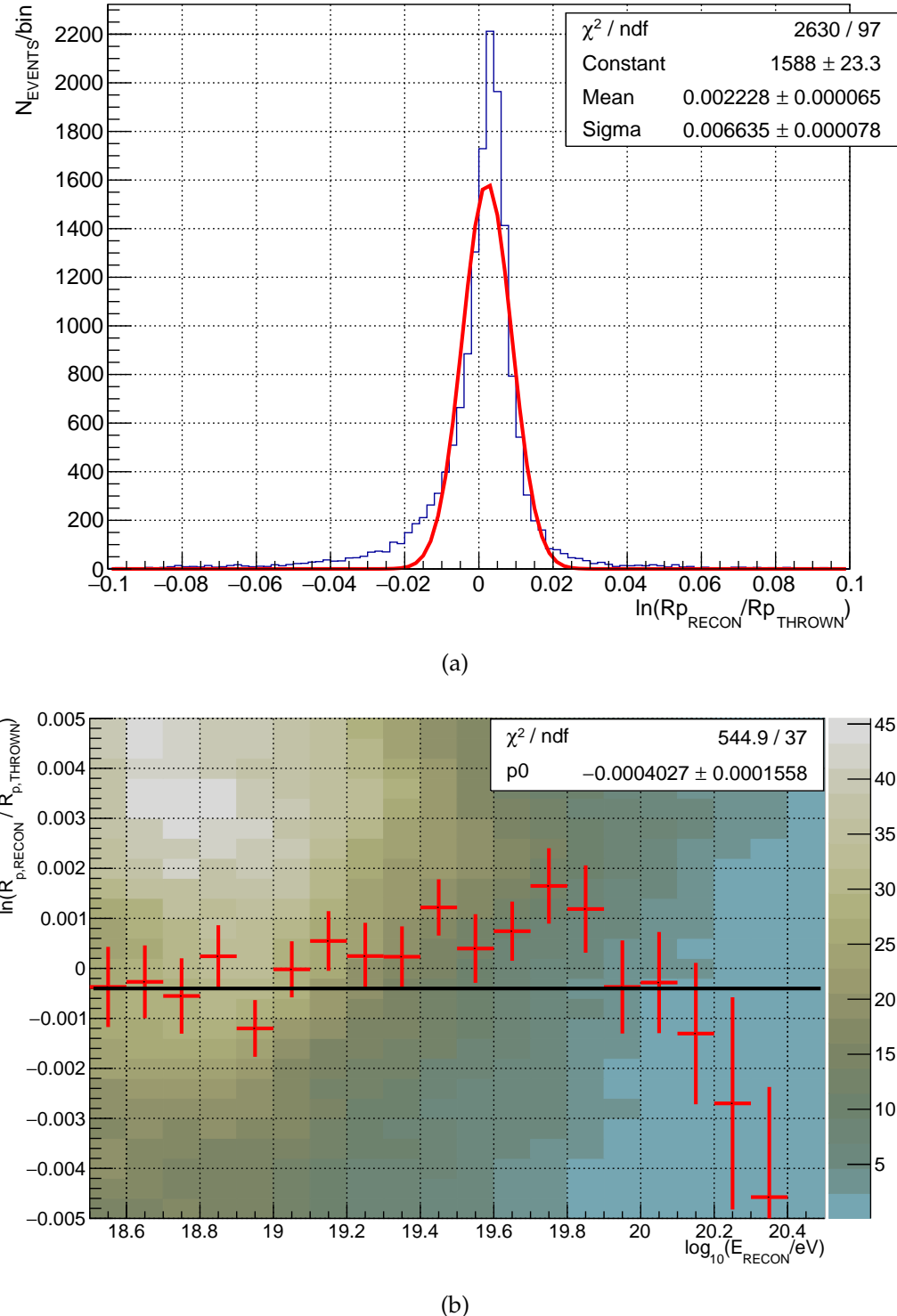


Figure 4.10: The impact parameter resolution histogram and impact parameter resolution as a function of energy. (a) The impact parameter resolution histogram. The red line is a Gaussian fit of the histogram. The fit parameters are displayed in the statistics box. (b) The impact parameter resolution as a function of energy.

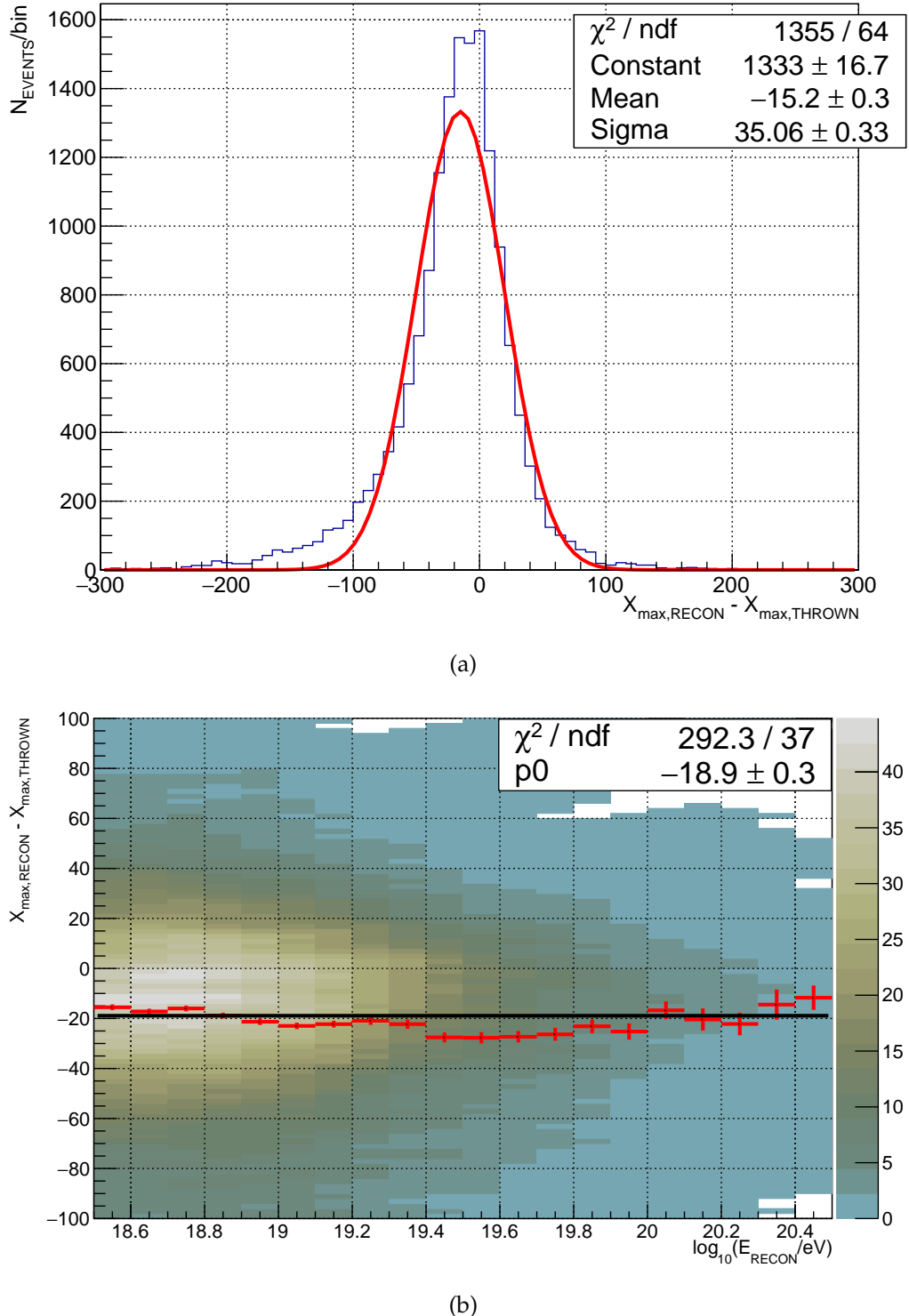


Figure 4.11: The X_{\max} resolution histogram and X_{\max} resolution as a function of energy. (a) The X_{\max} resolution histogram. The red line is a Gaussian fit of the histogram. The fit parameters are displayed in the statistics box. (b) The X_{\max} resolution as a function of energy.

CHAPTER 5

EVENT RECONSTRUCTION

Hybrid reconstruction pairs up coincident FD and MD events using a time-matching program described in Section 5.4. The advantage of hybrid analysis is that it improves the geometric reconstruction by adding the SD's timing information as constraints during fitting. The SDs also provides an accurate measurement of the shower core position and are used to further constrain event reconstruction. The improved geometrical reconstruction provides an improved energy measurement and gives a more reliable spectrum measurement than either the monocular FD or SD measurement. In this chapter, I will describe the data storage format for TAx4, the necessary FD and SD monocular reconstruction programs, along with the hybrid analysis programs used to create the hybrid event set.

5.1 Data Format

TAx4 data is stored and manipulated in the form of Data Storage Tape (DST) banks. A DST bank is similar to a FORTRAN common block or a C structure, with associated functions to read, write, and view the structure. At each processing step, new DST banks are created to store the results of that step. These new DST banks are appended to the existing collection of DST banks, which comprise an event. Each event is bound by START and STOP banks, which are simple banks that contain only a "start" or "stop" string.

Below is a discussion of the different DST banks that are used at different stages of reconstruction:

- **FRAW1:** stores the timing and signal information of all tubes that observe an event. All triggered mirrors and their 320 channels are recorded. Channels 1 to 256 represent the signals from each of the PMTs. Channels 257 to 272 are high-gain summations for columns 1 to 16, and channels 273 to 288 are low-gain summations for columns 1 to 16. Channels 289 to 304 are high-gain summations for rows 1 to 16, and channels

305 to 320 are low-gain summations for rows 1 to 16.

- FTRG1: contains the state of the mirrors, trigger codes, and row or column pattern coincidences per event.
- FPH01: is similar to the FRAW1 DST bank. It includes tube timing and signal information like the number of photoelectrons with the pedestal subtracted.
- FSCN1: records the information from the FADC scan. This information includes the pedestal, number of time slices in the pulse, and tube flags that tell if tubes are good, rejected by the scan, or have no signal.
- TLWEAT: stores the FD operator's weather code. This weather code is taken hourly during FD operations. Each weather code is 7-digits long and represents the seeing conditions during that event.
- STPS2: includes variables used to calculate the Rayleigh vector. This determines if an event is noise or an actual cosmic ray event. A small magnitude for the Rayleigh vector indicates a random or noise event, while a large magnitude indicates a real cosmic ray event.
- STPLN: contains the plane normal vector, track length, time difference between the last and first good tubes in microseconds. It is filled after fitting the shower detector plane (SDP) during pass 2, see section 5.2.3.
- HCTIM: contains information of shower track geometry. This includes the date, time, zenith angle, azimuthal angle, core position, angle in the SDP, the distance of closest approach, track length, crossing time, and the total number of photoelectrons. This bank is filled after the geometry fit of reconstruction, see section 5.4.1.
- HCBIN: contains the binned light flux as a function of shower depth in units of photoelectrons/m²/degree.
- PRFC: contains four shower profile parameters of the Gaisser-Hillas function: N_{max} , X_{max} , X_0 , and λ . This bank also contains information about the energy of the primary cosmic ray.

- MC04: contains the output of the Monte Carlo simulation. This bank has information about the thrown energy, Giasser-Hillas parameters, primary particle type, geometrical parameters, and the number of mirrors and tubes that are triggered.
- TALEX00: stores the timing and signal information of the SD FADCs. This bank is filled during the pass 0 of SD reconstruction, see Section 5.3.1.
- TLFPTN: contains the pattern recognition of SDs that are contiguous in both space and time and the SD core information.

5.2 FD Reconstruction

The FD reconstruction is handled by the *UTAFD* programs. These programs were originally written for the HiRes experiment [8] and have been modified for the Telescope Array geometry. The first three reconstruction “passes” of hybrid reconstruction are the same as the monocular reconstruction passes. They involve creating events from the raw data, identification of events, and the calculation of the shower detector plane. Each reconstruction pass is discussed in detail in the following sections.

5.2.1 Pass 0

The first reconstruction pass consists of time matching between event packets to build events. Triggered events from individual telescopes are matched using a GPS timing window of $100 \mu\text{s}$ to form an event. Events can be single mirror or multi-mirror. The data from adjacent telescopes are compared for telescope events that occur within $100 \mu\text{s}$ of each other and then are combined to form multi-mirror events. The event information is written in the FRAW1 bank for TAx4 by the TLFDP0 program.

This program also fills the FTRG1, FPH01, FSCN1, and TLWEAT DST banks. While it fills these banks, files are created with information parsed from the raw data. These files are described below.

- Calibration: These files contain the PMT’s gain and pedestal values based on the Roving Xenon Flasher (RXF) calibration and/or UVLED calibration. This works only uses the UVLED calibration files. Two of these files are generated for each mirror, one for the UVLED calibration at the start and for the UVLED calibration at the end of the observation period.

- Weather: These files, one for every data part, contain the weather code information entered by the on-shift FD runner. The files are formatted as follow - [??] [Weather code before part start] [Weather code during part] [Weather code after part stop] [time difference in seconds before start time] [time difference in seconds after start time] [time difference in seconds after stop time]. If no weather code was recorded during a data part, then the time after start is set to -1. An example of a weather file from 2021/10/11 part 1 is below

```
18249 0000001 0000001 0000001 2774 -1 -2774
```

If a weather code is recorded during the data part, then that is the weather code for the part; otherwise, the worse of the two before and after is used.

- Ontime: These files, one for every data part, contain the calculated ontine of all the telescopes. The files are formatted as follows - [UTC start in seconds] [UTC end in seconds] [part total ontine (hrs)] [m## percentage of time the mirror was on] [m## ""... etc. An example of an ontine file from 2021/10/11 part 1 is below.

```
14130 15325 0.33194 1.00000 1.00000 1.00000 1.00000
```

These files are used to calculate the ontine of the TAx4 detector.

- DAQ settings: These files contain information on the DAQ settings of the detector.

These files are used during future passes of reconstruction and the ontine calculation of the TAx4 detector. After the ASCII files are generated, the files are uploaded to an SVN repository, located on the TA Data SERVer (TADSERV), that forms a database of all the TAx4 calibration information.

5.2.2 Pass 1

The second reconstruction pass processes events through the STPS2 program to determine the probability that each event is a true cosmic ray event. This is done by determining the probability that an event was triggered by noise (e.g., airplane lights, flashers, fluctuations in the night sky, etc.) using a Rayleigh filter. Each pair of neighboring triggered tubes has unit vectors drawn from it to earlier triggered tubes. The sum of all such unit vectors forms a Rayleigh vector. If an event is caused by a cosmic ray, the magnitude of the

Rayleigh vector will be large, while a noise event will have a short Rayleigh vector. This pattern recognition method is based on a Rayleigh probability density function, defined by

$$p(r) = \frac{r}{\sigma^2} \exp\left[-\frac{r^2}{2\sigma^2}\right]. \quad (5.1)$$

where r is the magnitude of the Rayleigh vector after N steps of adjacent pairs of tubes with spatial separation less than 1.5° and time separation less than 14 ns, and $\sigma = N/2$. Integrating Equation 5.1 gives the probability that the magnitude of vector r is greater than a randomly chosen magnitude, R , defined as

$$\text{Prob}(r > R) = \int_R^\infty p(r)dr = \exp\left[-\frac{R^2}{2\sigma^2}\right]. \quad (5.2)$$

From this equation, the useful parameter P_{\log} can be defined as

$$P_{\log} = -\log_{10}(\text{Prob}(r > R)) = \frac{R^2}{N \ln 10}. \quad (5.3)$$

Events with a $P_{\log} > 2$ correspond to a $\leq 1\%$ probability that the event was generated by random noise. Figure 5.1 shows an example of a random noise event and a real event.

The Rayleigh vector can also be used to determine the approximate direction of the event (e.g., up, down, horizontal). Most cosmic ray events are downward going; therefore, events that are upward going or within 20° of horizontal are excluded from this work's analysis. All the results of this reconstruction pass are filled to the STPS2 DST bank.

5.2.3 Pass 2

The third reconstruction pass uses the STPLN program to calculate the Shower Detector Plane (SDP) using the pointing directions of the PMTs. The SDP plane fitting is done by minimizing a χ^2 function assuming a line source (i.e., air shower has no lateral distribution) and all telescopes are located at one point. The χ^2 function to minimize is

$$\chi^2 = \sum_i \frac{(\hat{n} \cdot \hat{n}_i)^2 \cdot w_i}{\sigma_i^2}, \quad (5.4)$$

where \hat{n} is the shower detector unit normal, \hat{n}_i is the pointing unit vector of the i^{th} tube, w_i is the number of photoelectrons seen by the i^{th} tube, and σ_i is the angular uncertainty of the i^{th} tube. The angular uncertainty of all the PMTs is set to 1° , the viewing angle of an individual PMT, because we can't determine where a photon hit on the face of the PMT. The geometry of the SDP is shown in Figure 5.2.

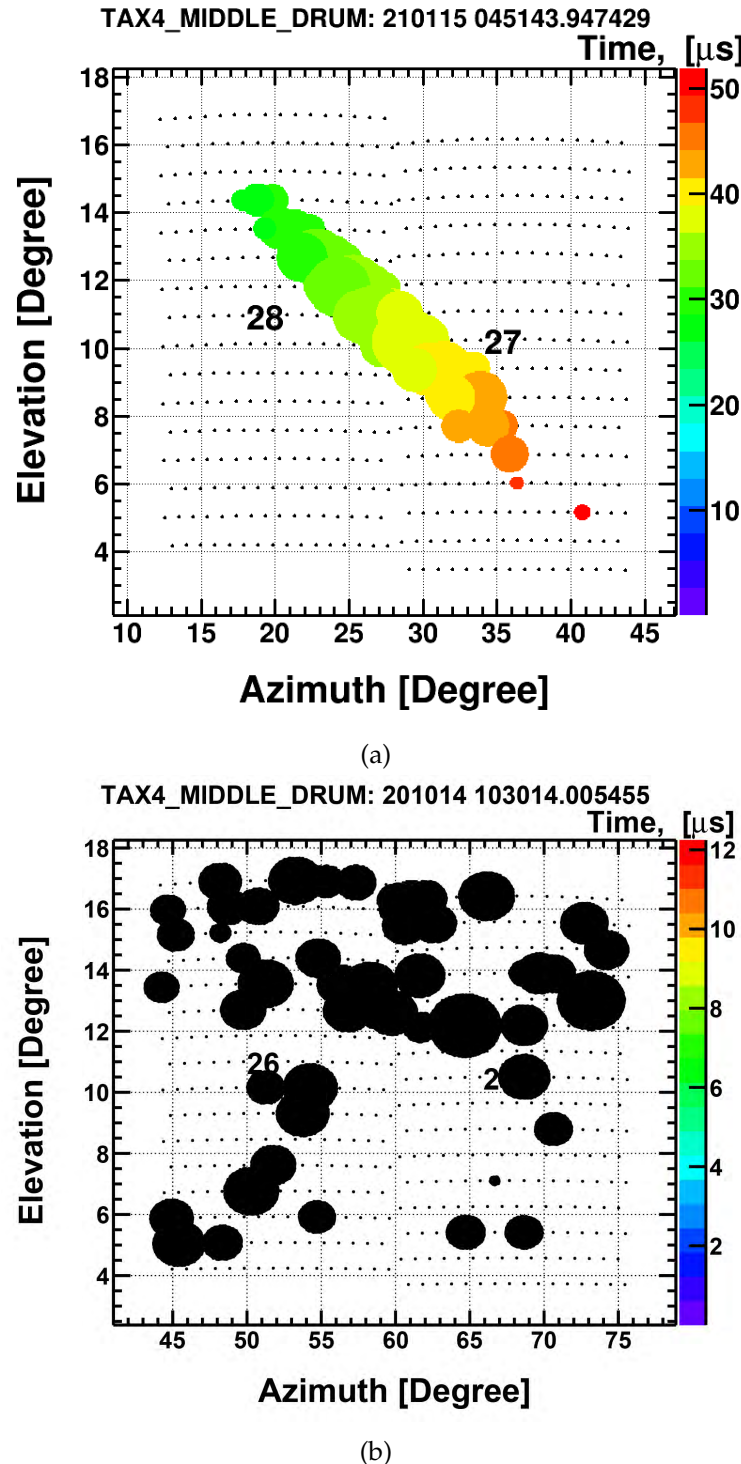


Figure 5.1: Examples of a track-like event and a random noise event. (a) Is an example of a track-like event. The size of the circles are proportional to the tube's signal size and the color represents the tube's timing. This is an FD event from the TAX4 North on 2021/01/15 at 4:51:43.95 UTC. (b) An example of a noise event. All bad tubes appear black in the event display. These tubes all have the same trigger time.

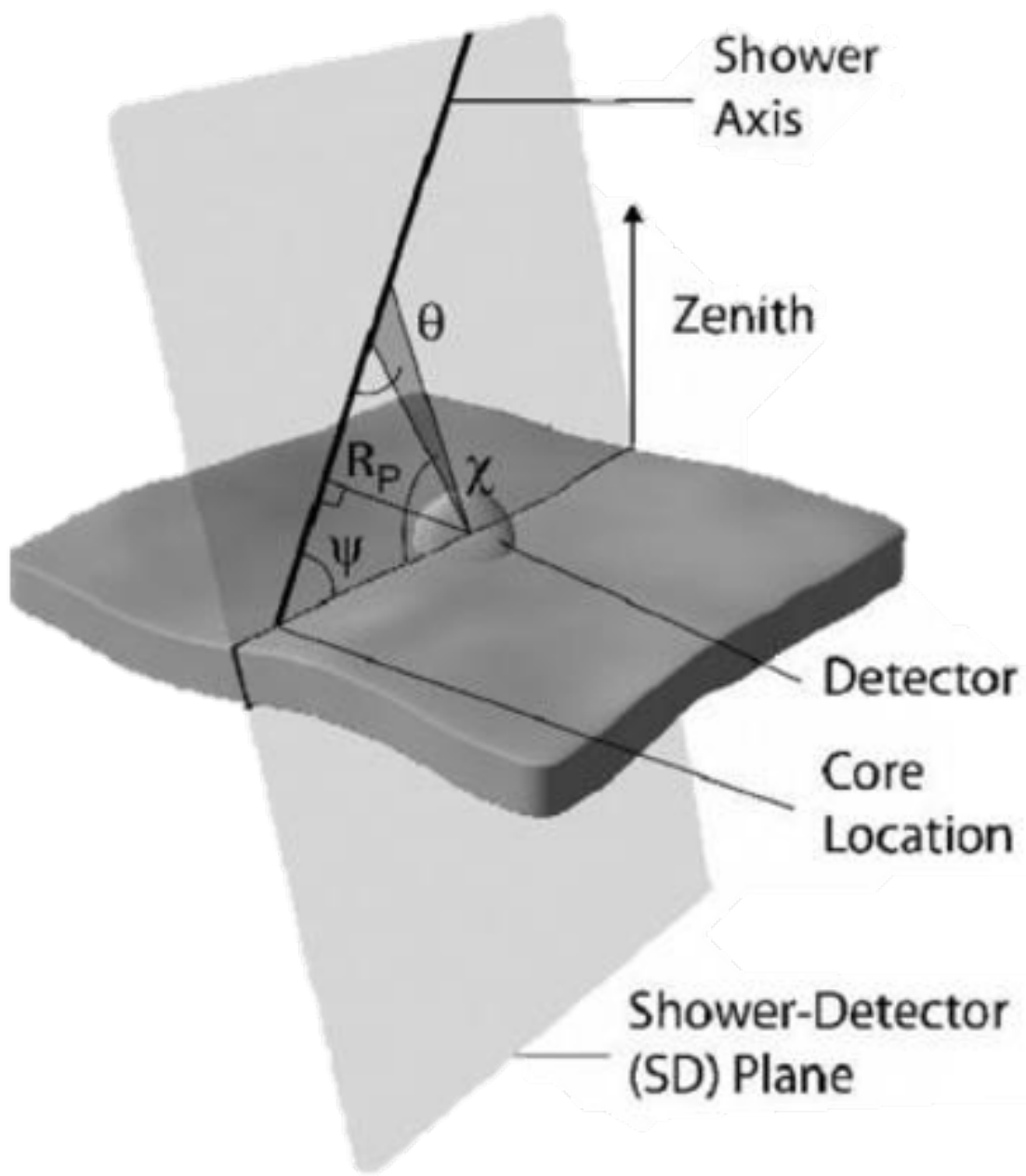


Figure 5.2: Shower-Detector Plane (SDP) diagram.

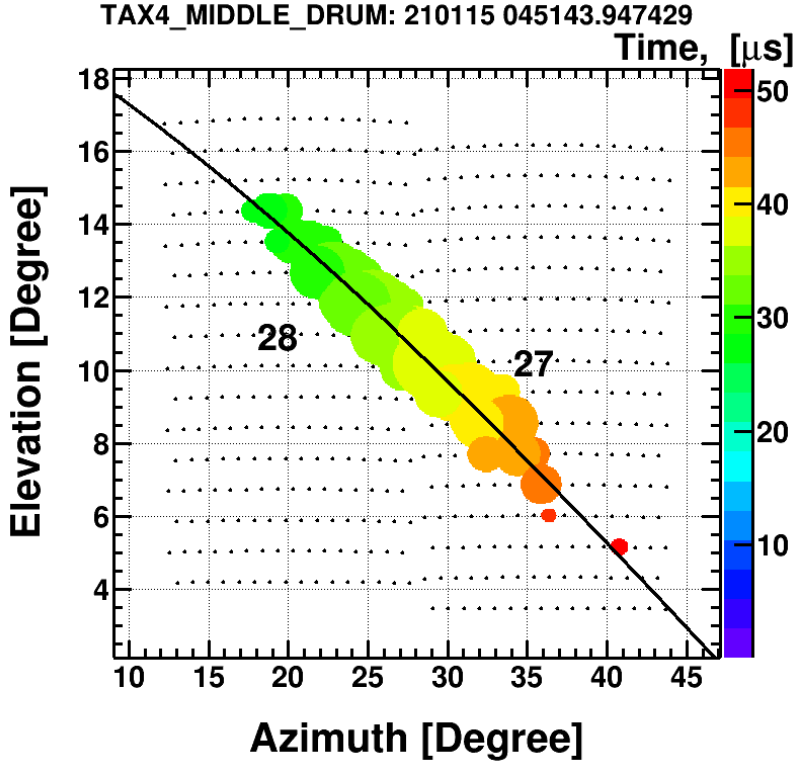


Figure 5.3: An FD event display with the SDP fitted, indicated by the black line, to the event track. The size of the circles are proportional to the tube's signal size and the color represents the tube's timing. This an FD event from the TAx4 North on 2021/01/15 at 4:51:43.95 UTC.

During the plane fitting, noise tubes are identified and removed from the fit using an iterative procedure that continues until no further tubes are removed. Noise tubes are defined as tubes with a two μs time residual between the tube's triggering time and the majority of the tubes in the track, or as tubes that have a spatial correlation more than 5° from the plane. Once the SDP is identified, the normal vector of the SDP, track length, crossing time, and inverse angular speed are calculated and stored in the STPLN DST bank. An example of SDP fit can be seen in Figure 5.3 as a black line projected on the FD display.

5.3 SD Reconstruction

The TAx4 SD raw data contains trigger and waveform information about the secondary particles from EAS passing through the scintillator and producing light that is detected by the PMTs. The TAx4 SD reconstruction consists of two passes that parse the raw data to extract the FADC waveforms and determine the geometry of the event. The SD

reconstruction is handled by the *tlanalysis* programs. These programs were developed by D. Ivanov to handle SD data reconstruction from all the arrays in the TA experiment.

5.3.1 Pass 0

The UTSDPASS0 program parses the raw SD data by scanning the FADC traces and finding the time of the signals. It also calibrates the signals using the TA SD nominal calibration. The program was set to have an event recombination widow of 100 μs and a duplicate event removal time window of 200 μs . Figure 5.4 show the PMT waveform from an TAx4 SD event, counter 7412, for an event observed on 2021/01/15 at 4:51:43.95 UTC. All results of this reconstruction pass are filled in TALEX00 DST bank.

This program also generates DST files with SD monitoring information automatically. These DST files contain monitoring cycle information such as pulse charge histograms, pulse height histograms, pedestal histograms, detector status variables, GPS error flag information, and other monitoring information for the SDs. Since these files aren't used in the analysis, I won't discuss them in further detail.

5.3.2 Pass 1

The second reconstruction pass is processed through the TLFPTN program. This program handles the information from the triggered events and fits the geometry of the shower. First, the program determines which counters are part of the event and which are due to electronic noise or stray muons. This is done by only including counters which are considered contiguous in both space and time. Counters are considered contiguous in space if they are within $\sqrt{2} \times$ the counter spacing. This ensures that SDs that are diagonal are included. SDs are contiguous in time if their trigger time difference divided by the speed of light is less than or equal to their spacing. Counters that don't fit this pattern recognition criterion are removed from the analysis.

Using the assumption that shower particles travel at the speed of light, the program finds the shower track vector using the trigger times of each SD in the event. Figure 5.5 shows a diagram of SD event geometry, and shows shows useful variables for determining the geometry of the shower. The program minimizes a χ^2 equation, defined as

$$\chi_{geom}^2 = \sum_{i=0}^N \frac{(t_i - t_i^F)^2}{\sigma_{t_i}^2} + \frac{||R - R_{COG}||^2}{\sigma_{R_{COG}}^2}, \quad (5.5)$$

by varying the parameters T_0, R_x, R_y, θ and ϕ . In Equation 5.5, R represents the shower core position on the ground, R_{COG} is the core position as calculated by the Center Of Gravity (COG) calculation. The COG is calculated using the pulse heights of the signals from each of the triggered detectors and is as the starting point for the SD core calculation.

The timing fit function, t^F , and the uncertainty in the timing, σ_t are defined as,

$$t^F = T_0 + \frac{l}{c} + \tau \quad (5.6)$$

$$\sigma_t = \sqrt{\sigma_e^2 + \sigma_\tau^2} \quad (5.7)$$

where τ is the time delay of the shower front to the i^{th} counter, c is the speed of light, and T_0 is the time when the shower core hits the SD plane. The distance l is defined as the distance along the propagation axis from the shower core to the i^{th} counter, defined as

$$l = (\mathbf{r} - \mathbf{R}) \cdot \hat{\mathbf{n}}(\theta, \phi), \quad (5.8)$$

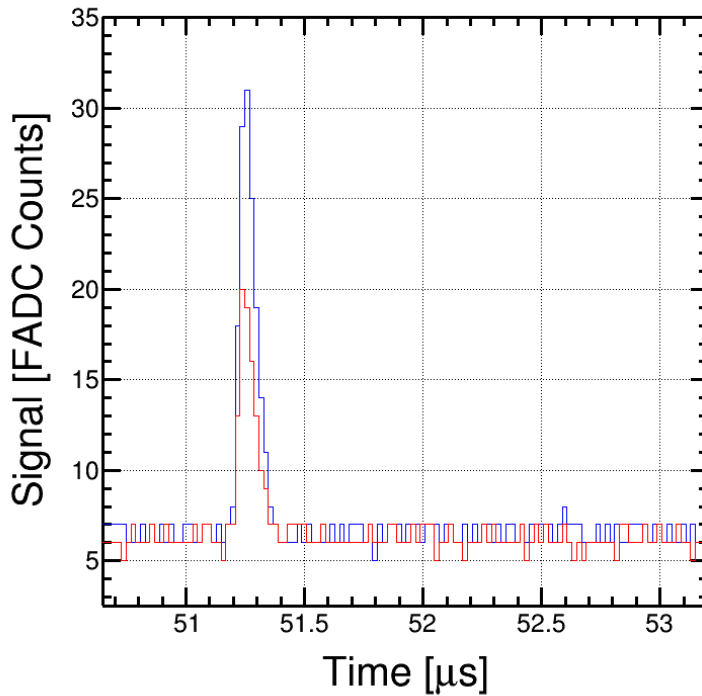


Figure 5.4: FADC signal waveform from SD counter 7412. This FADC trace is from an SD event in the northern array on 2021/01/15 at 4:51:43.95 UTC. The blue and red lines represent the signal seen in the upper and lower scintillator layers respectively.

where \mathbf{R} is the position of the shower core on the ground relative to the CLF, \mathbf{r} is the position of the i^{th} counter on the ground, and $\hat{\mathbf{n}}(\theta, \phi)$ is the unit vector in the direction of the shower core. The time delay function, τ , defined as

$$\tau = a \left(1.0 - \frac{l}{20.8 \times 10^3} \right)^{1.05} \left(1.0 + \frac{s}{30} \right)^{1.35} \rho^{-0.5} \quad (5.9)$$

is modeled as a modified Linsley time delay function [25]. The uncertainty of the time delay function is defined as

$$\sigma_\tau = (1.56 \times 10^{-3}) \left(1.0 - \frac{l}{20.8 \times 10^3} \right)^{1.05} \left(1.0 + \frac{s}{30} \right)^{1.5} \rho^{-0.3}. \quad (5.10)$$

In Equations 5.9-5.10, s is the lateral distance of the i^{th} counter, and ρ is the pulse height per unit area of the signal. The factor $\left(1.0 - \frac{l}{20.8 \times 10^3} \right)^{1.05}$ was added due to a preliminary analysis of TA SD data by D. Ivanov [19] and modified for the increased spacing between the TAx4 SDs. Figure 5.6a shows an example of a TAx4 SD time fit and Figure 5.6b is the resulting SD event display after the timing fit. All the results of this reconstruction pass are filled in the TLFPTN DST bank.

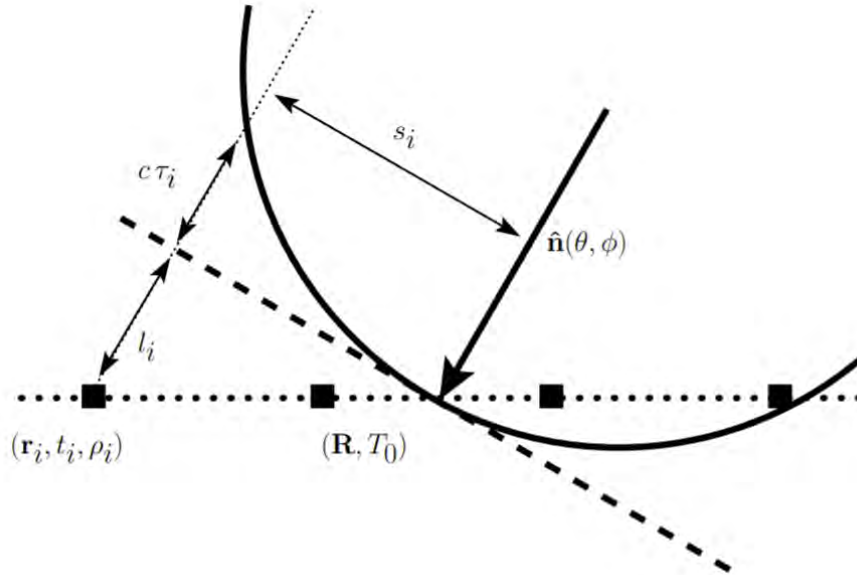


Figure 5.5: Schematic of the shower front as it hits the SD array. A unit vector in the direction of the shower axis is represented by $\hat{\mathbf{n}}(\theta, \phi)$, R is the position where the shower core crosses the SD plane, and T_0 is the time that the shower core hits the SD plane. Plot taken from M. Allen's Ph.D. thesis [9].

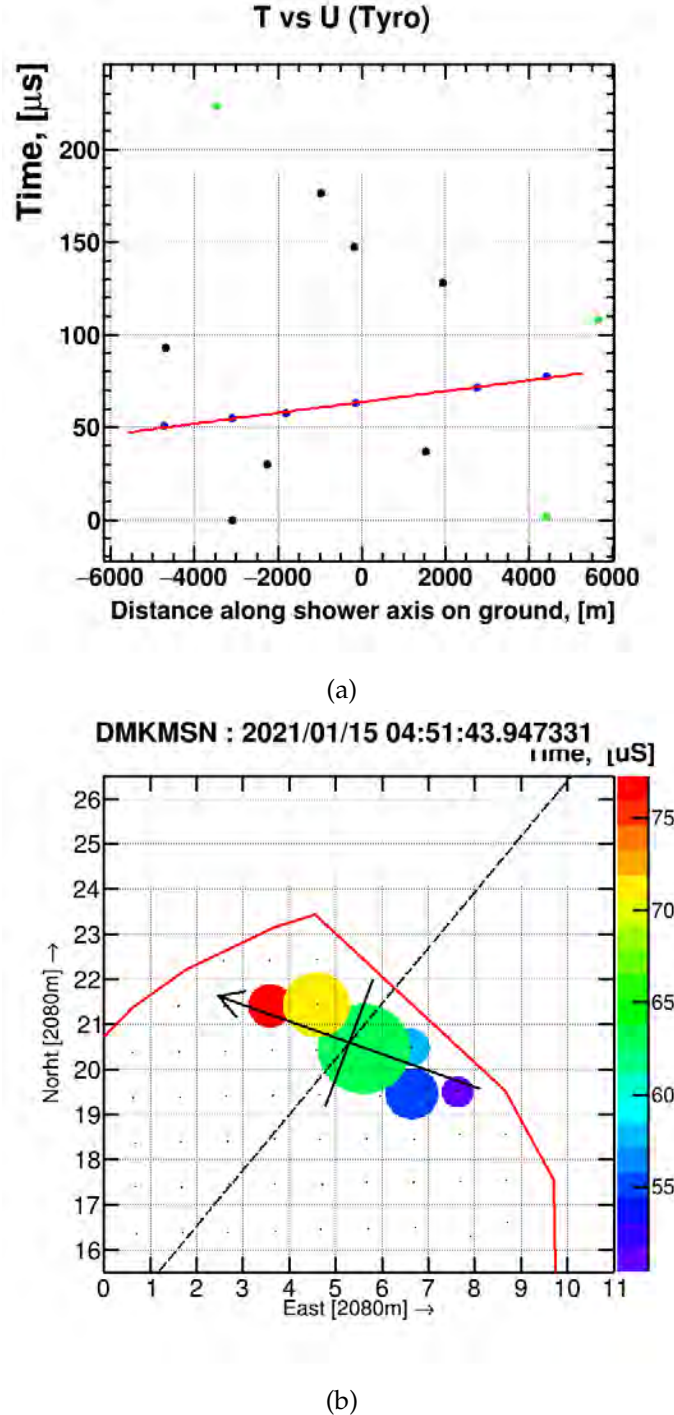


Figure 5.6: SD timing fit and event display. (a) The time of the counters hit plotted as a function of distance along the projection of the shower axis on the ground. The black dots are triggered SDs, the green dots are SDs contiguous in space, the blue dots are SDs contiguous in space and time, and the red line represent the timing fit to the SDs that are contiguous in space and time. (b) An SD event display of an event on 2021/01/15 at 4:51:43.97331 in the northern array. The black arrow shows the results of the timing fit for the shower core, and the dashed line represents the projection of the SDP onto the SD plane.

5.4 Hybrid Reconstruction

As I have described in previous sections, the SD and FD parts of the hybrid events are reconstructed separately through SD pass1 and FD pass 2. The hybrid reconstruction utilized programs from both *UTAFD* and *tlanalysis* to combine the information from the SD and FD into a single hybrid event and calculate the hybrid geometry and energy.

First, a time matching program, TMATCH, compares the timing information of each event. As described in Section 3.2.5, before 2020/11/07, there was a known one integer second offset between the FD and SD event timing; thus, if the relative timing of the SD and FD event is within 2.0002 s of each other, the events are considered a match. These matched events are combined into a single common event. The broad time matching window ensures that events are matched despite the one integer second offset between the detectors; however, this time window is problematic for hybrid trigger events from March to November of 2020. This is because the hybrid trigger was being sent to the SD array at the wrong time. These events are removed from the analysis during event selection, described in Chapter 6.

5.4.1 Hybrid Geometry Reconstruction

The time-matched event's geometry is determined using information from both detectors with the TLHYBGEOMNP program. To determine the best hybrid geometry, a χ^2 function defined as

$$\chi^2 = \chi_{FD}^2 + \chi_{SD}^2 + \chi_{core}^2, \quad (5.11)$$

is minimized. This equation takes into account the FD timing, SD timing, and the position of the core of the EAS as determined by the SDs.

An accurate geometrical reconstruction can be calculated by fitting the tube viewing angles within the SDP as a function of the arrival time of the light at the tubes from the EAS. Figure 5.7 shows an "in-plane" view of the SDP's geometry. The fit function is defined as,

$$t_i = t_0 + \frac{R_p}{c} \tan\left(\frac{\pi - \psi - \chi_i}{2}\right), \quad (5.12)$$

where t_i is the trigger time of the i^{th} tube, t_0 is the time the shower reaches the impact parameter (R_p), ψ is the angle of the shower track within the SDP, and χ_i is the tube viewing angle within the SDP. Equation 5.12 is then minimized by

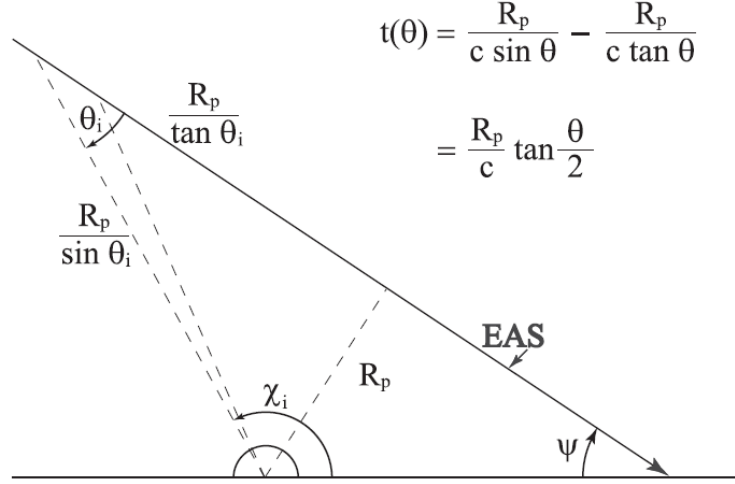


Figure 5.7: SDP in-plane geometry diagram with parameter labels. The diagram shows how the PMT trigger time is related to a given pointing angle within the SDP. Plot taken from M. Allen [9].

$$\chi_{FD}^2 = \sum_i \frac{1}{\sigma_i^2} \left[t_i - \left(t_0 + \frac{R_p}{c} \tan \left(\frac{\pi - \psi - \chi_i}{2} \right) \right) \right]^2. \quad (5.13)$$

An example of this fit, known as a Timing vs. Angle plot, can be seen in Figure 5.8a. This figure shows the monocular Timing vs. Angle plot. The χ^2 minimization is used to determine the in-plane angle (ψ), impact parameter (R_p), and time to reach R_p (t_0).

The timing information from the SDs is used to constrain the Timing vs. Angle fit seen in Figure 5.8b. This figure shows the hybrid Timing vs. Angle plot. The triggered SD closest to the shower core is treated as a virtual PMT located at the TAx4 detector site. The trigger time for this SD is adjusted by the following equation:

$$t_{SD} = t_{SD_{trig}} + \frac{d_{SD}}{c} \quad (5.14)$$

where t_{SD} is the time that a virtual PMT would trigger at the detector site, $t_{SD_{trig}}$ is the actual trigger time of the counter, d_{SD} is the distance to the SD from the TAx4 site, and c is the speed of light. An example of Hybrid Timing vs. Angle plot can be seen in Figure 5.8b. Equation 5.14 is then minimized by

$$\chi_{SD}^2 = \sum_i \frac{1}{\sigma_i^2} \left[t_i - \left(t_0 + \frac{R_p}{c} \tan \left(\frac{\pi - \psi - \chi_i}{2} \right) \right) \right]^2. \quad (5.15)$$

Notes this equation is the same as Equation 5.13; however, the difference is that the observed time, t_i , is calculated for each SD. The times of the SD signals arrive later than the

PMTs because the SDs are sampling the shower on the ground, and the light takes time to get from the shower core to the telescope. The additional information from the added SD counter extends the range in time and angle of the calculation, which yields a more accurate calculation of the geometrical parameters of the EAS.

The final constraint of the hybrid analysis is the core constraint. The minimization to determine the x and y coordinates of the shower core is defined as

$$\chi^2_{core} = \sum_i^2 \frac{||R_i - R_{COG}||}{\sigma_{R_{COG}}^2}, \quad (5.16)$$

where R_{COG} is the reconstructed core position from the SD Center of Gravity (COG), R_i are the trial parameters, and $\sigma_{R_{COG}}^2$ is set to 170 m. Note that $i = 1$ represents the x-coordinates and $i = 2$ corresponds to the y-coordinates of the SDs.

The five parameters ψ, θ, R_p, R_x , and R_y are varied incrementally and used to minimize Equation 5.11. The results of the fitting give the hybrid geometry of the cosmic ray event and are stored in the HCTIM DST bank. Using the calculated hybrid geometry in the HCTIM DST bank, the program converts the viewing angles of each "good" tube into slant depth, in g/cm², and stores the results in the HCBIN DST bank.

5.4.2 Energy Reconstruction

The hybrid energy reconstruction is performed by the STPFL12 program. The signal seen by each tube is plotted as a function of shower depth (values taken from the HCBIN DST bank) to produce a profile of the shower. Then the contribution to the fluorescence light from Rayleigh scattering, aerosols, direct scintillation light, and Cerenkov light is calculated. Figure 5.9 shows an example of a profile from a TAx4 North event on 2021/01/15 at 4:51:43.95 UTC. After the profile is generated, the energy of the shower is calculated using an inverse Monte Carlo (MC) technique. All the results of the STPFL12 program are stored in the PRFC DST bank.

The inverse MC technique involves generating Monte Carlo shower parameters parametrically using Poisson statistics and using them as inputs in the profile fitting given by the Gaisser-Hillas parameterization function, defined as,

$$N_e(x) = N_{\max} \left[\frac{x - X_0}{X_{\max} - X_0} \right]^{\frac{X_{\max} - X_0}{\lambda}} \exp \left[\frac{X_{\max} - x}{\lambda} \right]. \quad (5.17)$$

Here, N_e is the number of charged particles at a given slant depth, X_{\max} is the slant depth where the number of secondary particles reaches its maximum, N_{\max} is the maximum number of particles at X_{\max} , and λ is a fit parameter related to the width of the shower profile. The values of $X_0 = -100\text{g/cm}^2$ and $\lambda = 70\text{g/cm}^2$ are fixed [23], while X_{\max} and N_{\max} are varied. The impact parameter is also varied for a given ψ to further improve the profile fit further. New geometry information is calculated and updated in the HCTIM DST bank. This process is iterated until the profile fit χ^2 function, defined as

$$\chi^2_{profile} = \sum_i \frac{1}{\sigma_i^2} \left(S_i^{\text{observed}} - S_i^{\text{predicted}} \right)^2, \quad (5.18)$$

is minimized. Here, S_i^{observed} is the observed signal and $S_i^{\text{predicted}}$ is the predicted signal of the i^{th} tube based on shower parameters from the inverse MC technique. The minimized χ^2 values give the MC shower that best matches the observed shower. The energy of that MC shower is then stored as the calculated hybrid energy of the real EAS.

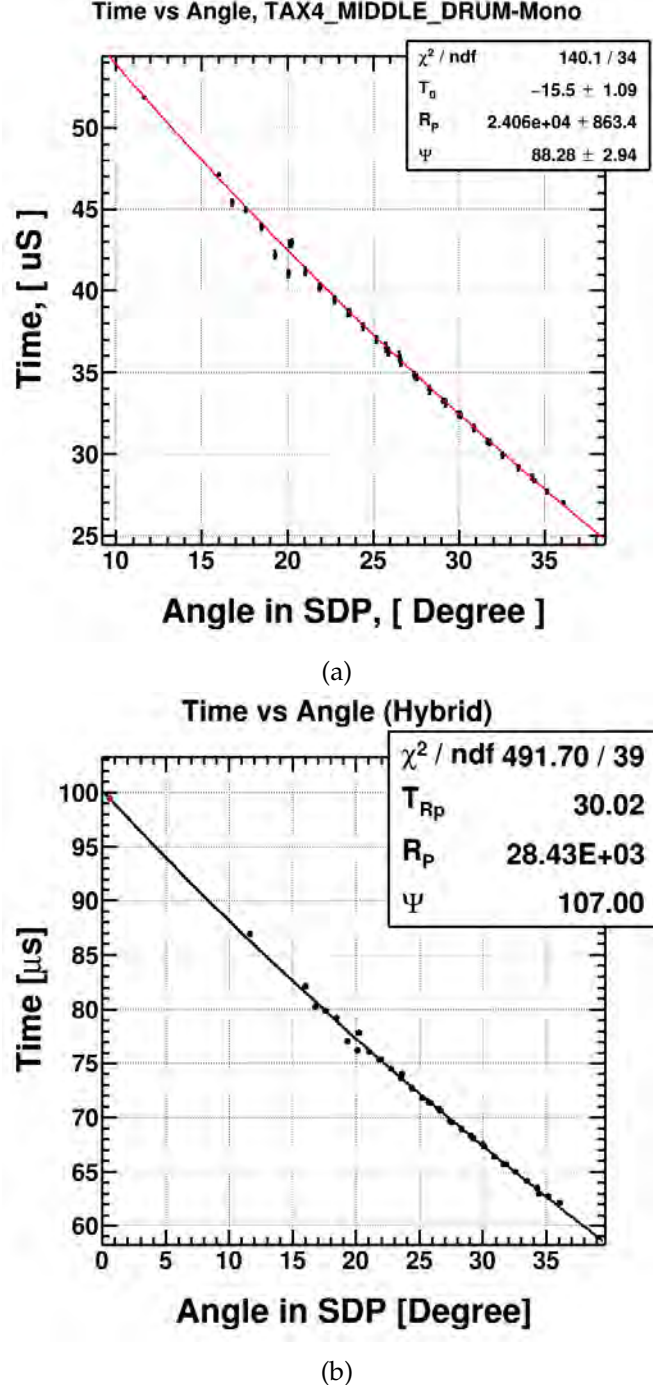


Figure 5.8: Monocular and Hybrid timing vs angle fit for the same event on 2021/01/15 at 4:51:43.95 UTC. The PMT tube timing, black points, are plotted as a function of elevation angle within the SDP. Fitting the curvature provides the timing and impact parameter, which combined with the SDP, give directional information of the primary cosmic ray. The tubes are fit to a quadratic function and those which deviate too far from the fit are removed. (a) Monocular time verse angle fit. (b) Hybrid time verse angle fit. A virtual PMT is created using information from the SD counter closest to the core, represented by the red point.

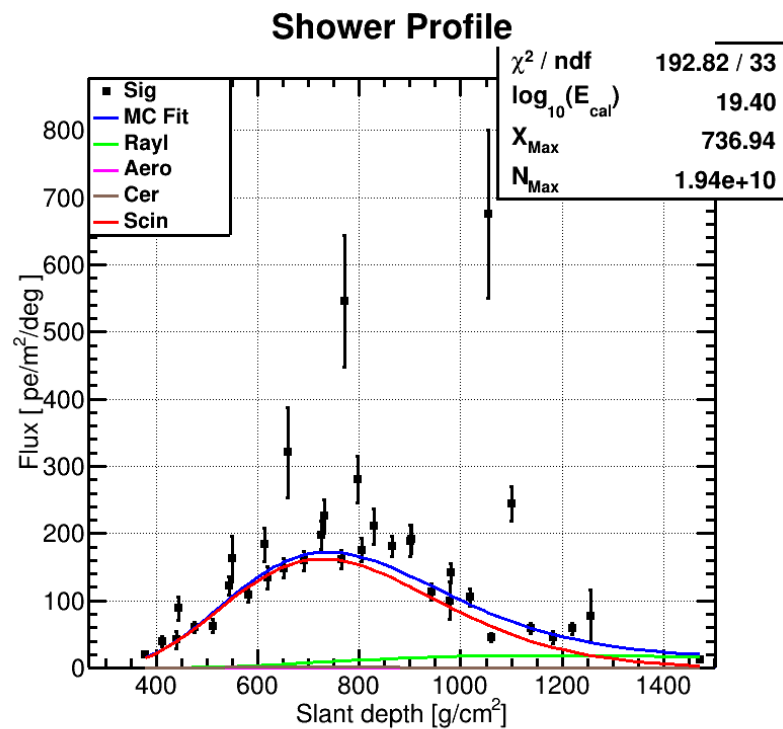


Figure 5.9: Shower profile plot for an event on 2012/01/15 at 4:51:43.95 UTC. The signal of the "good" PMTs is plotted as a function of slant depth in the shower. The points are fit to the Gaisser-Hillas function (Equation 5.17), and the fit results are shown in the statistical box. The amount of light generated due to Rayleigh scattering, Aerosols, Cerenkov light, and direct Scintillation light is also shown.

CHAPTER 6

DATA SELECTION AND DATA-MC COMPARISON

In this work, I analyzed about two years of data collected between June 2019 and October 2021. The data and the MC are processed using the same programs discussed in previous chapters. Quality cuts are applied to the fully reconstructed showers to obtain a good resolution and Data-MC comparisons. These cuts ensure quality while being loose enough to have decent event statistics above $10^{18.5}$ eV. Table 6.1 summarizes this work's quality cuts. An event is considered quality if,

- An event has a good weather flag. Events are considered good weather if there are no overhead clouds and seeing conditions are good (i.e., no haze or smoke).
- Events have a reconstructed energy that must be greater than $10^{18.5}$ eV. Below this energy, the acceptance of the hybrid detector begins to decrease, and the assumption of 100% SD trigger efficiency is no longer valid.
- Both the geometry (from the time versus angle fit) and profile fits for an event must have a χ^2/dof for that fit that is less than or equal to 50.
- The event's shower core must lie within the SD array border.
- The position of the shower core calculated by the hybrid fit and by SD-only fit are within 5 km of each other.
- The attempted fix of the one integer second offset in the TAx4 North array, discussed in Section 3.2.5, caused hybrid triggers to be sent to the northern SD array at the wrong time during a short window of time. Therefore, all hybrid trigger events between March 30, 2020, and November 7, 2020, for TAx4 North are discarded.

The number of data events that are retained after each cut level is shown in Table ??.

Name	Description
Energy Cut	$E \geq 10^{18.5}$ eV
Weather Cut	No overhead clouds and good seeing conditions
Hybrid Trigger Cut	Discard hybrid trigger events between March 2020 and October 2020 for the TAx4 North site
Core Position Cut	The hybrid core position is within 5 km of the core position calculated by SD only.
Border Cut	The shower core must be within the SD array
χ^2/ndf Cut	Profile and geometry $\chi^2/\text{ndf} \leq 50$

Table 6.1: TAx4 hybrid quality Cuts used in this works analysis. The same quality cuts are applied to both TAx4 sites.

6.1 Example Event

An example of a hybrid trigger event from the TAx4 South detector is shown in Figures 6.1 - 6.5. Figure 6.1 shows an FD event display with the fitted shower detector plane. Figure 6.2 shows an SD event display with the SDP projection to the SD plane and core position plotted. Figure 6.3 shows a T vs. U plot to determine the SDs that are contiguous in both space and time. Figure 6.4 shows the Time vs Angle plot using hybrid fitting. Figure 6.5 shows the profile fit to estimate the calorimetric energy of the shower.

This event is a double mirror event with about a ten μs long duration. In the time versus angle fit, the in-plane angle, ψ , is determined to be 120.54° . This means the direction of the event is coming towards the detector at a distance of 23 km. From the profile fit, we see that X_{max} is barely in the FOV, but most of the shower development is captured. The signal is dominated by scintillation light, and the energy of this event was estimated as $10^{19.99}$ eV. This is the highest energy event that is this works data analysis.

6.2 Data-MC Comparisons

The data and Monte Carlo events are reconstructed using the same programs discussed in the previous chapter, and observable distributions are compared to check if they agree with each other. Comparing these observable distributions is important to understanding whether our MC accurately represents the data.

In Figures 6.6 - 6.10 the zenith angle (θ), in-plane angle (ψ), azimuth angle (ϕ), impact parameter (R_p), and total energy from the MC are compared with the real data distributions. The azimuthal angle is plotted with respect to the detector FOV. These figures are

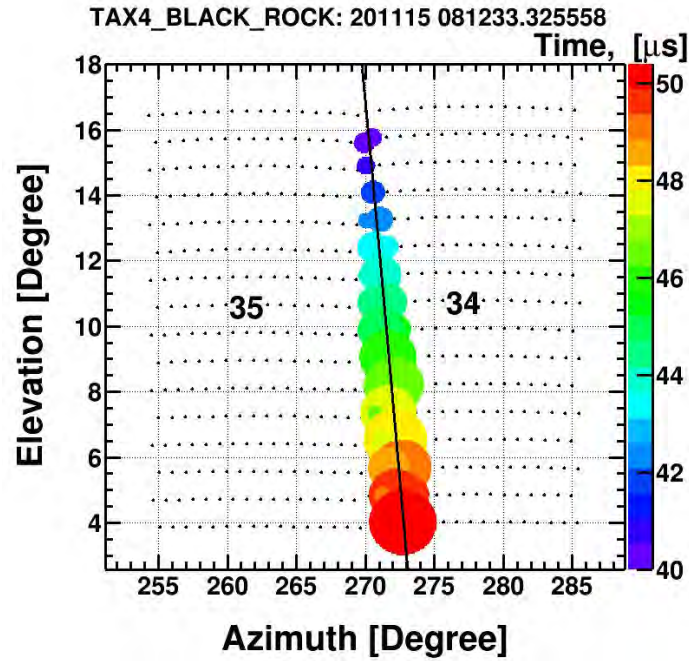


Figure 6.1: An FD event display of the highest energy event used in this work's analysis. This an FD event from the TAx4 South detector on 2020/11/15 at 08:12:33 UTC.

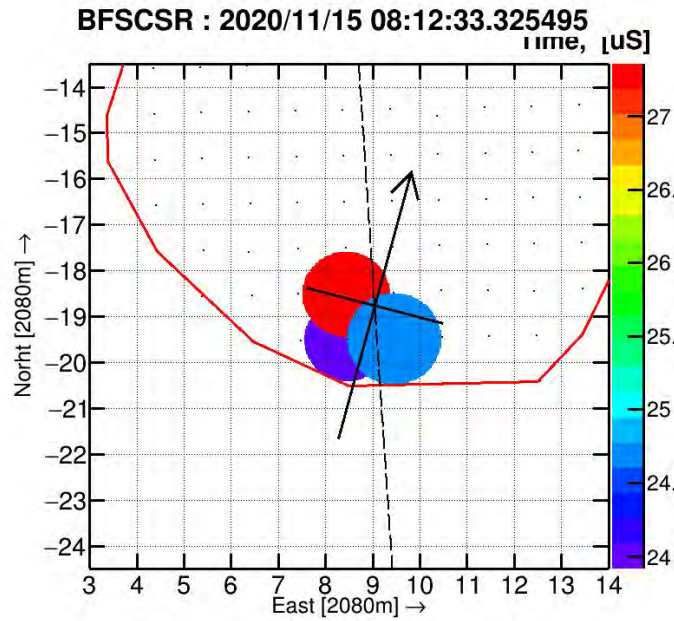


Figure 6.2: An SD event display of the highest energy event used in this work's analysis. This an SD event from the TAx4 South detector on 2020/11/15 at 08:12:33.33 UTC. Only the SDs that had both scintillator layers trigger and are contiguous in space and time are plotted.

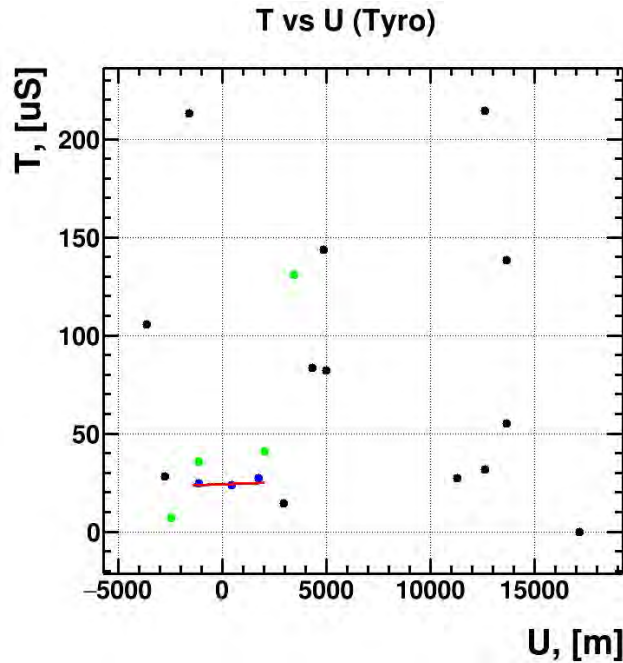


Figure 6.3: A time verse angle fit of the an SD event from the TAx4 South detector on 2020/11/15 at 08:12:33.33 UTC. This event is the highest energy event used in this work's analysis.

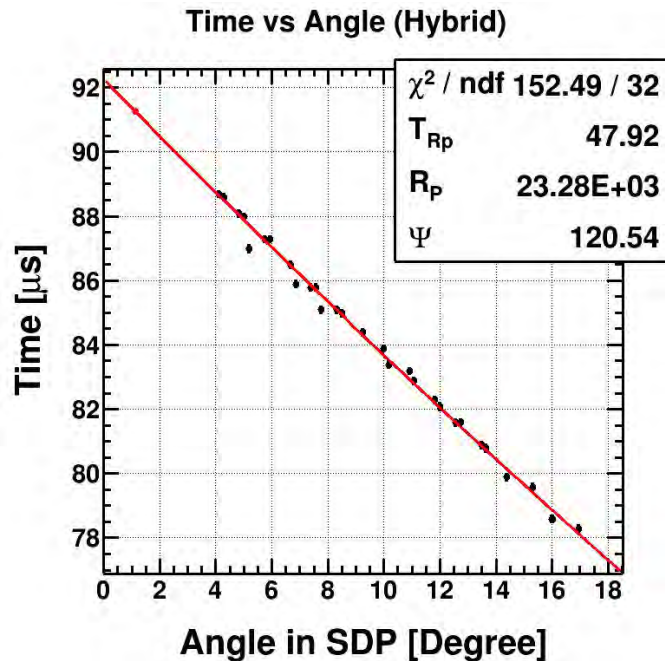


Figure 6.4: A hybrid time verses angle fit of the highest energy event used in this work's analysis. This event is taken from the TAx4 South detector on 2020/11/15 at 08:12:33.33 UTC.

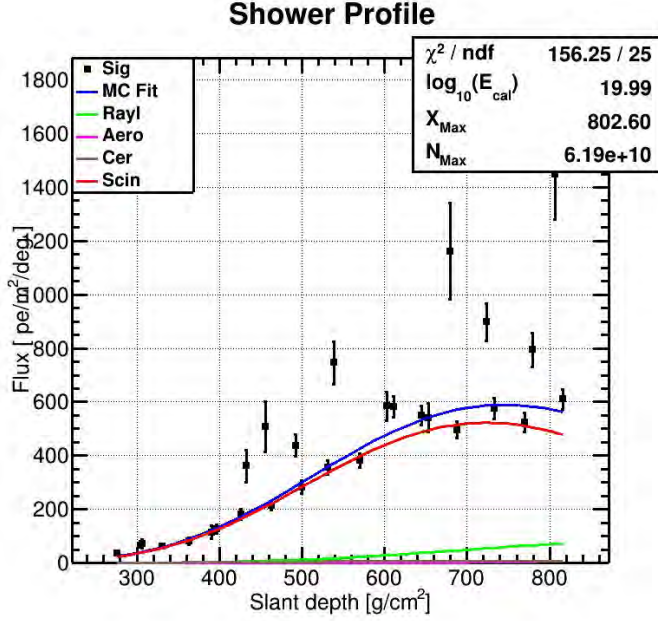


Figure 6.5: The profile plot of the highest energy event in this work's analysis. This event is taken from the TAx4 South detector on 2020/11/15 at 08:12:33.33 UTC.

separated into two panels; the top panel shows the observable parameter and the MC distributions, and the bottom panel shows the ratio of the data to the MC events. The number of MC events is orders of magnitude larger than the data; therefore, I normalize the area under the curve of the MC histogram to that of the data histogram's area. This allows for a proper comparison of the two histograms. The top panels also show the results of a Kolmogorov-Smirnov (K-S) test performed to compare the data and MC distributions. For a K-S test, values greater than 0.2 indicate reasonable agreement [9]. The bottom panels are fitted with a line whose slope is another indicator of the agreement between the two distributions. If the fitted line's slope is relatively flat, it indicates that the data and MC are in reasonable agreement, while a steep slope indicates disagreement.

Figure 6.6 shows the data-MC comparison of the zenith angle, θ . In the top panel, the K-S test returns a value of 0.98 for its probability; this means the distributions are in good agreement with each other. In the bottom plot, the slope is flat with a value of -0.00143, indicating a reasonable agreement between the data and the MC.

Figure 6.7 shows the data-MC comparison of the in-plane angle, ψ . In the top panel, the K-S test returns a value of 0.53 for its probability; this means the distributions are in good

agreement with each other. In the bottom plot, the slope is flat with a value of 0.00117, indicating a reasonable agreement between the data and the MC.

Figure 6.8 shows the data-MC comparison of the azimuth angle, ϕ . In the top panel, the K-S test returns a value of 0.86 for its probability; this means the distributions are in good agreement with each other. In the bottom plot, the slope is flat with a value of -0.00022, indicating a reasonable agreement between the data and the MC.

Figure 6.9 shows the data-MC comparison of the impact parameter, R_p . In the top panel, the K-S test returns a value of 0.89 for its probability; this means the distributions are in good agreement with each other. In the bottom plot, the slope is relatively flat with a value of -0.01097, indicating reasonable agreement between the data and the MC.

Figure 6.10 shows the data-MC comparison of the total energy. In the top panel, the K-S test returns a value of 0.52 for its probability; this means the distributions are in good agreement with each other. In the bottom plot, the slope is relatively flat with a value of 0.4283, indicating reasonable agreement between the data and the MC.

Despite the low statistics and parametric SD MC used in the analysis of this work, the data-MC comparisons appear to show general agreement. I am now ready to calculate the cosmic ray energy spectrum.

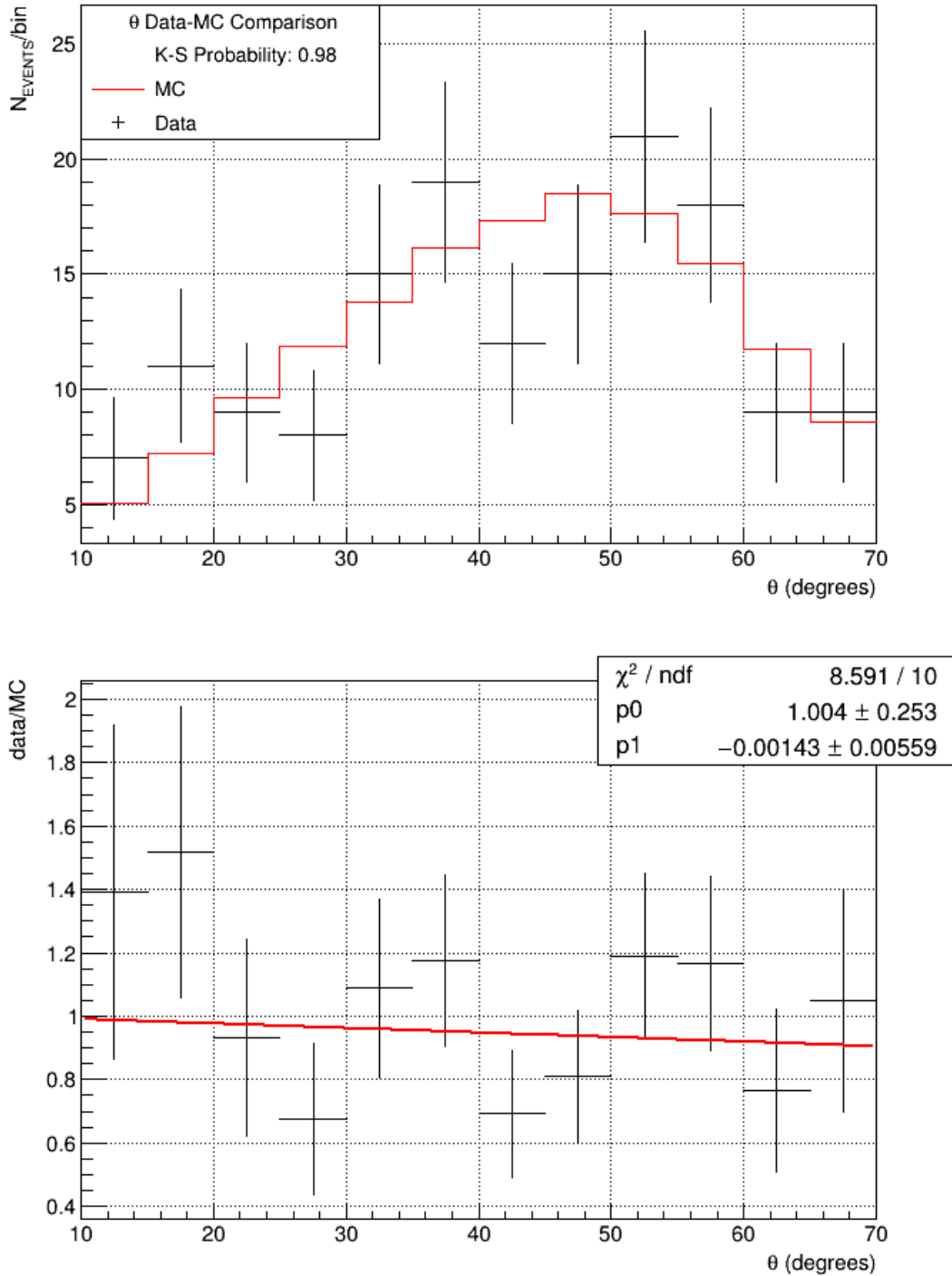


Figure 6.6: Data-MC Comparison of zenith angle, θ , distribution. In the top panel, the data is shown by the black points and the MC distribution is shown by the red histogram. The top panel also includes the K-S probability between the data and MC distributions. In the bottom panel, the ratio of the data to MC is shown along with a linear best fit line.

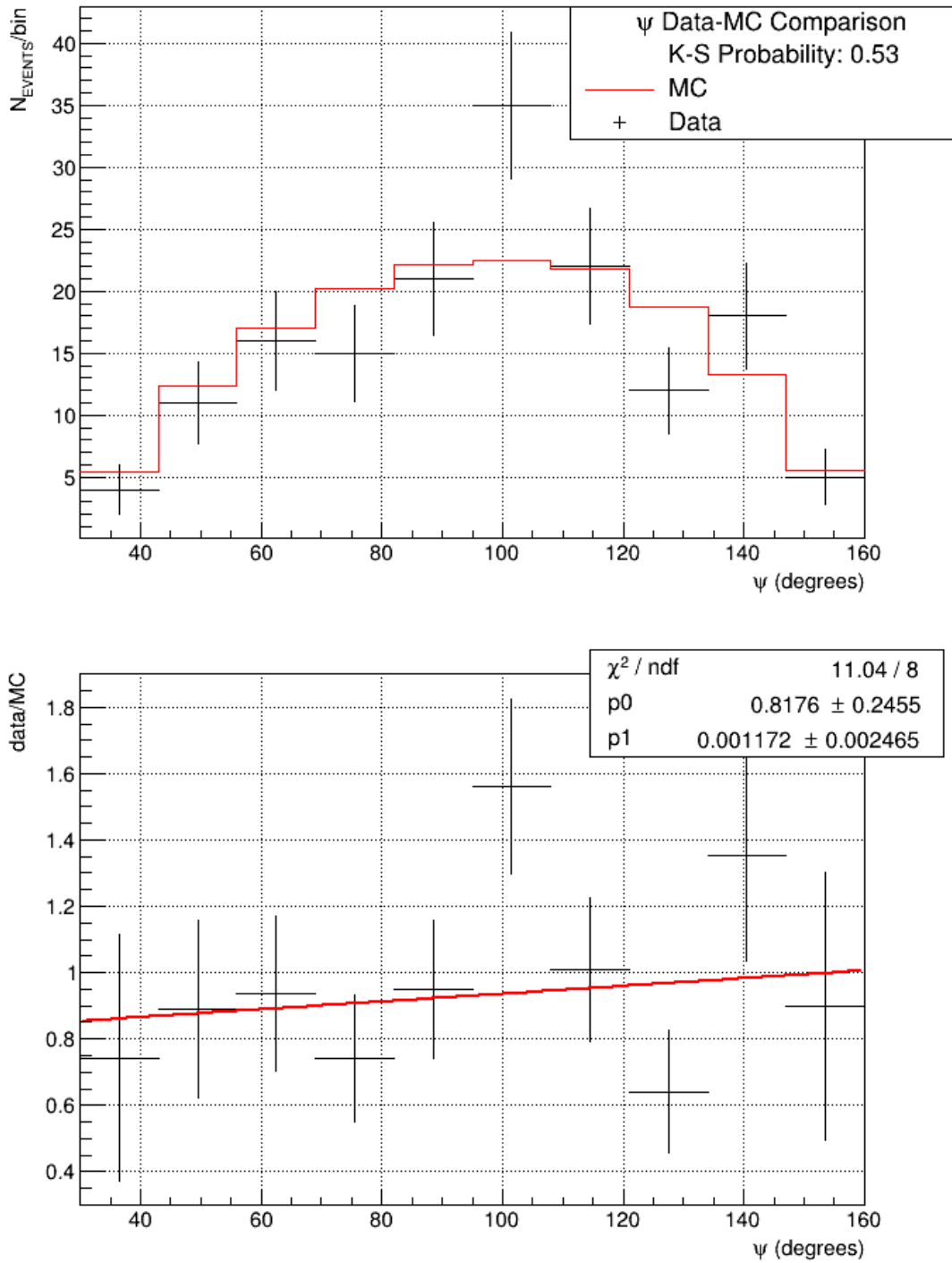


Figure 6.7: Data-MC Comparison of in-plane angle, ψ , distribution. In the top panel, the data is shown by the black points and the MC distribution is shown by the red histogram. The top panel also includes the K-S probability between the data and MC distributions. In the bottom panel, the ratio of the data to MC is shown along with a linear best fit line.

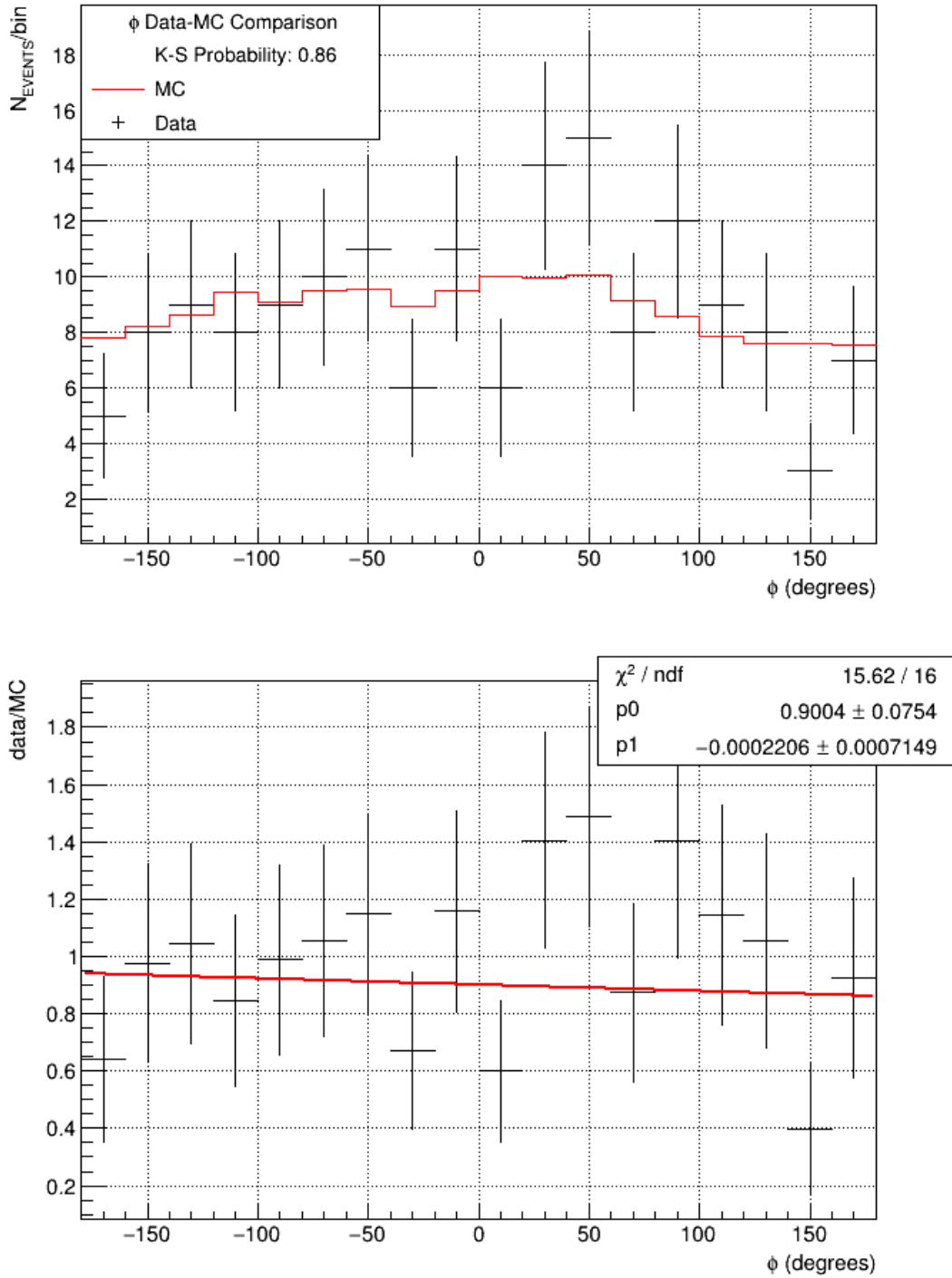


Figure 6.8: Data-MC Comparison of azimuth angle, ϕ , distribution. In the top panel, the data is shown by the black points and the MC distribution is shown by the red histogram. The top panel also includes the K-S probability between the data and MC distributions. In the bottom panel, the ratio of the data to MC is shown along with a linear best fit line.

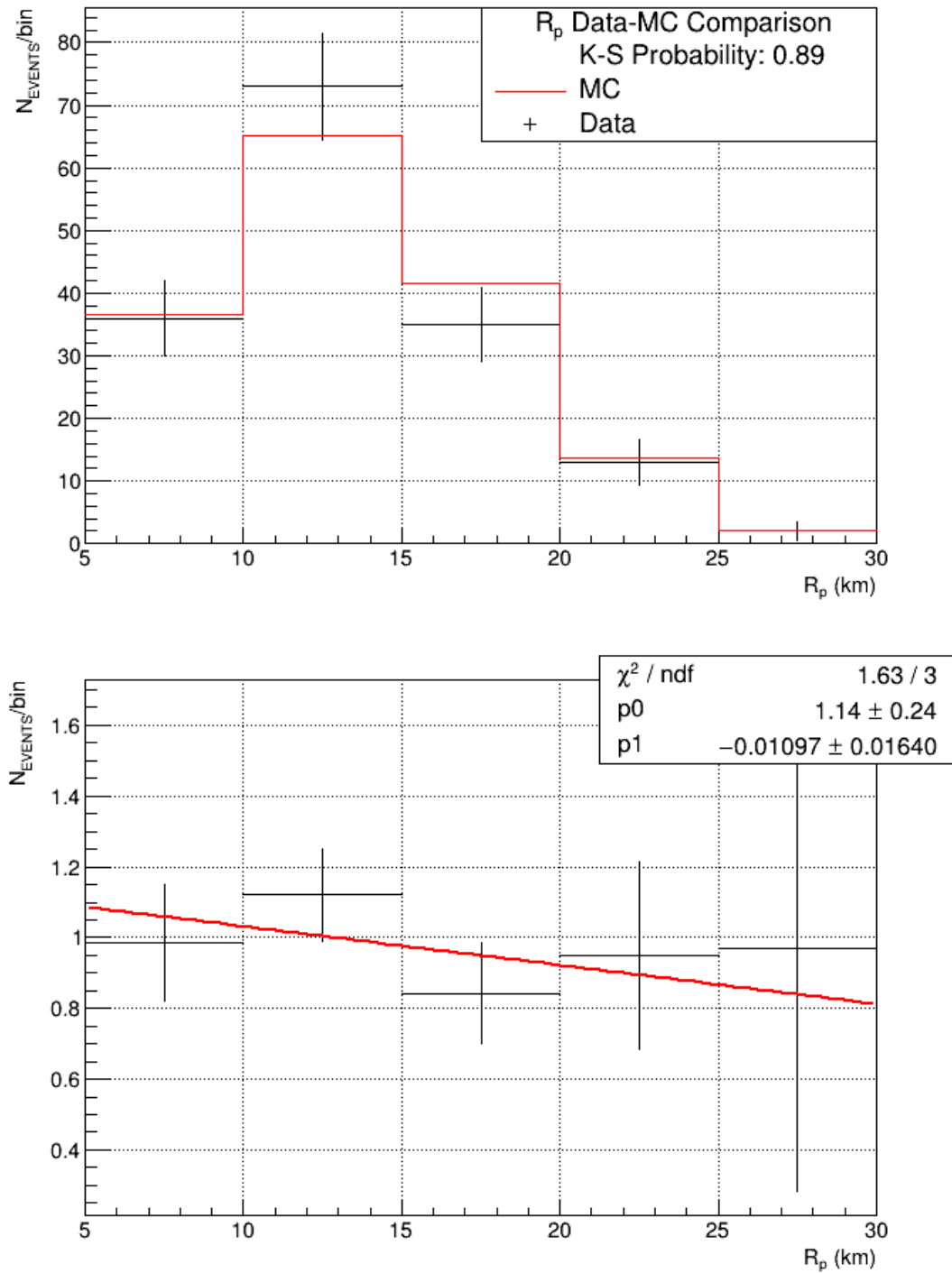


Figure 6.9: Data-MC Comparison of impact parameter, R_p , distribution. In the top panel, the data is shown by the black points and the MC distribution is shown by the red histogram. The top panel also includes the K-S probability between the data and MC distributions. In the bottom panel, the ratio of the data to MC is shown along with a linear best fit line.

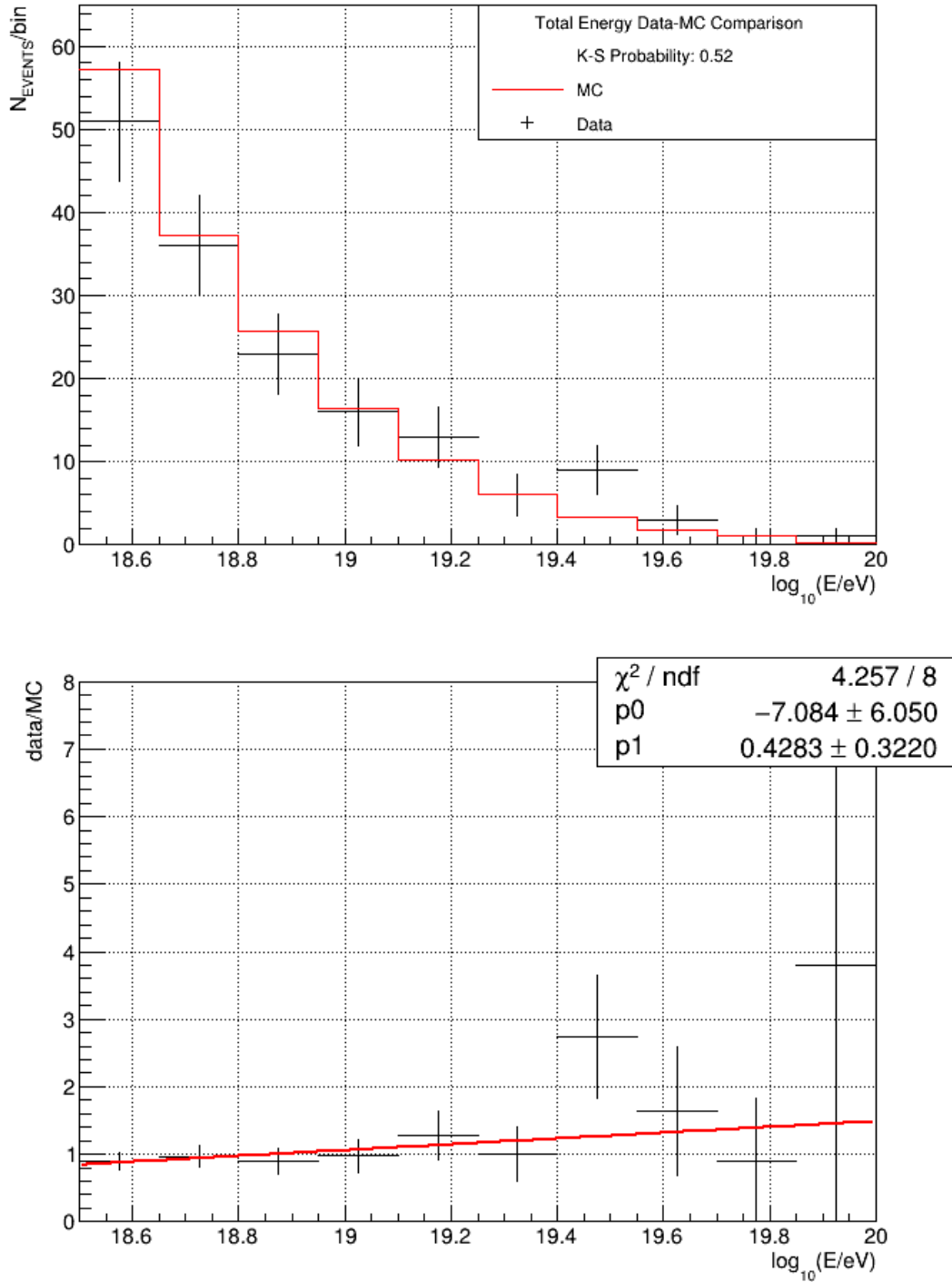


Figure 6.10: Data-MC Comparison of the the total energy distribution. In the top panel, the data is shown by the black points and the MC distribution is shown by the red histogram. The top panel also includes the K-S probability between the data and MC distributions. In the bottom panel, the ratio of the data to MC is shown along with a linear best fit line.

CHAPTER 7

RESULTS

In the previous chapter, I have shown that the data and the MC agree with each other reasonably well. This means we understand the detector response to cosmic rays reasonably well. Thus, I am ready to calculate the energy spectrum using hybrid events observed by the TAx4 detectors. Section 7.1 starts with a review of how the cosmic ray energy spectrum is calculated and describes the aperture, detector ontime, and exposure calculations needed to produce an energy spectrum. Finally, I show the measured hybrid energy spectrum compared to other the ICRC 2019 TA combined energy spectrum results in Section 7.2.

7.1 Spectrum Calculation

The cosmic ray energy spectrum is calculated by how many cosmic ray events are observed per unit area per unit solid angle per unit time per unit energy. This is written as

$$J(E_i) = \frac{N_{\text{TAx4}}(E_i)}{\epsilon_{\text{TAx4}} \times \Delta E_i}, \quad (7.1)$$

where $J(E_i)$ is the flux of cosmic rays, $N_{\text{TAx4}}(E_i)$ is the number of hybrid events observed by both TAx4 sites, ϵ_{TAx4} is the TAx4 detector exposure, and ΔE_i is the width of the i^{th} energy bin. In the following subsections each piece of the energy spectrum calculation is explained in detail.

7.1.1 Event Distribution

The total number of events detected by the TAx4 is written as

$$N_{\text{TAx4}}(E_i) = N_N(E_i) + N_S(E_i), \quad (7.2)$$

where $N_N(E_i)$ and $N_S(E_i)$ are the number of hybrid events observed by the TAx4 North and TAx4 South sites respectively. Figure 7.1 shows the number of hybrid events per energy bin for TAx4 after quality cuts have been applied.

$\log_{10}(E/eV)$	TAX4 North N(E)	TAX4 South N(E)	Total N(E)
18.5	16	17	33
18.6	7	26	33
18.7	10	11	21
18.8	6	9	15
18.9	6	10	16
19.0	5	3	8
19.1	5	4	9
19.2	5	2	7
19.3	2	1	3
19.4	4	4	8
19.5	2	0	2
19.6	1	1	2
19.7	1	0	1
19.8	0	0	0
19.9	0	1	1
Total Events	70	89	159

Table 7.1: Number of data events per energy bin from 2019/06/26 to 2021/10/11.

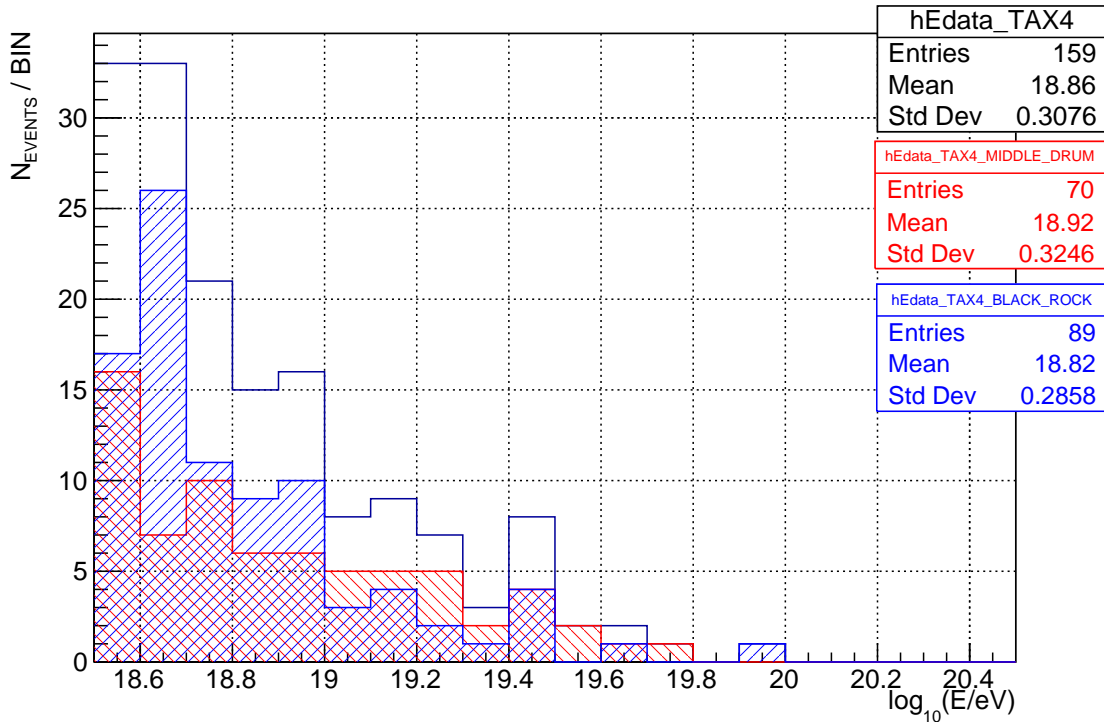


Figure 7.1: Number of hybrid data events per energy bin from 2019/06/26 to 2021/10/11. All events pass the quality cuts summarized in Table 6.1. The individual event distributions for the TAX4 North and TAX4 South detectors are represented by the red and blue histograms, respectively. The summation of both detector sites is represented by the black histogram.

7.1.2 Aperture

The aperture of the detector is dependent upon the layout and efficiency of the detector as well as on the geometry and energy of the shower. Higher energy EASs are brighter and can be seen farther away, while lower energy events can only be observed near the detector. The aperture and acceptance are calculated using the MC technique. The aperture of the detector is defined as,

$$A\Omega(E) = \frac{N_{\text{recon}}(E)}{N_{\text{thrown}}(E)} \times A_0\Omega_0 \quad (7.3)$$

where $N_{\text{recon}}(E)$ is the number of reconstructed MC events that pass quality cuts, $N_{\text{thrown}}(E)$ is the number of MC events thrown, A_0 is the effective area that is determined by thrown impact parameter range, Ω_0 is the solid angle that is determined by maximum thrown zenith angle, and $\frac{N_{\text{recon}}(E)}{N_{\text{thrown}}(E)}$ is the detector acceptance. The reconstructed aperture is shown in Figure 7.2. As the energy increases, the efficiency and SD aperture become constant and the aperture becomes limited by physical boundaries. The effective area for each detector is defined by

$$A_0 = \pi \left(R_{p,\max}^2 - R_{p,\min}^2 \right), \quad (7.4)$$

where $R_{p,\max} = 50$ km and $R_{p,\min} = 100$ m, and is equal to approximately $7,854$ km 2 . The solid angle for each detector is defined as

$$\Omega_0 = 2\pi (1 - \cos(\theta_{\max})), \quad (7.5)$$

where $\theta_{\max} = 70^\circ$, and is equal to approximately 4.13 sr.

7.1.3 Detector Ontime

The ontine for the TAx4 hybrid detector is limited by the ontine of the FDs. The ontine of each telescope is parsed from the raw data in pass 0, discussed in Section 5.2.1, and stored in ASCII files. Each file records how long each telescope is active; then, these times are summed for each run period.

In this analysis, I used data from TAx4 Epoch II, which includes data observed from June 2019 through October 2021. Figure 7.3 shows the number of ontine hours for both TAx4 sites plotted as a function of date. I examined all data files and summed up the time that each mirror trigger was permitted, summarized in Table 7.3. The total ontine for TAx4 North and TAx4 South is 1420.17 and 827.58 hours, respectively. This total ontine

$\log_{10}(E/eV)$	TAX4 N Aperture ($m^2\text{sr}$)	TAX4 S Aperture ($m^2\text{sr}$)
18.5	9.424×10^7	4.875×10^8
18.6	1.199×10^8	6.773×10^8
18.7	1.508×10^8	8.198×10^8
18.8	1.722×10^8	9.963×10^8
18.9	2.135×10^8	1.089×10^9
19.0	2.274×10^8	1.173×10^9
19.1	2.613×10^8	1.275×10^9
19.2	2.561×10^8	1.376×10^9
19.3	2.589×10^8	1.329×10^9
19.4	2.727×10^8	1.343×10^9
19.5	2.635×10^8	1.332×10^9
19.6	2.381×10^8	1.346×10^9
19.7	2.736×10^8	1.160×10^9
19.8	2.362×10^8	1.214×10^9
19.9	2.326×10^8	1.435×10^9
20.0	2.447×10^8	1.183×10^9
20.1	2.595×10^8	1.163×10^9
20.2	4.661×10^8	1.387×10^9
20.3	1.870×10^8	8.312×10^8
20.4	1.527×10^8	5.982×10^8

Table 7.2: TAX4 reconstructed aperture per energy bin.

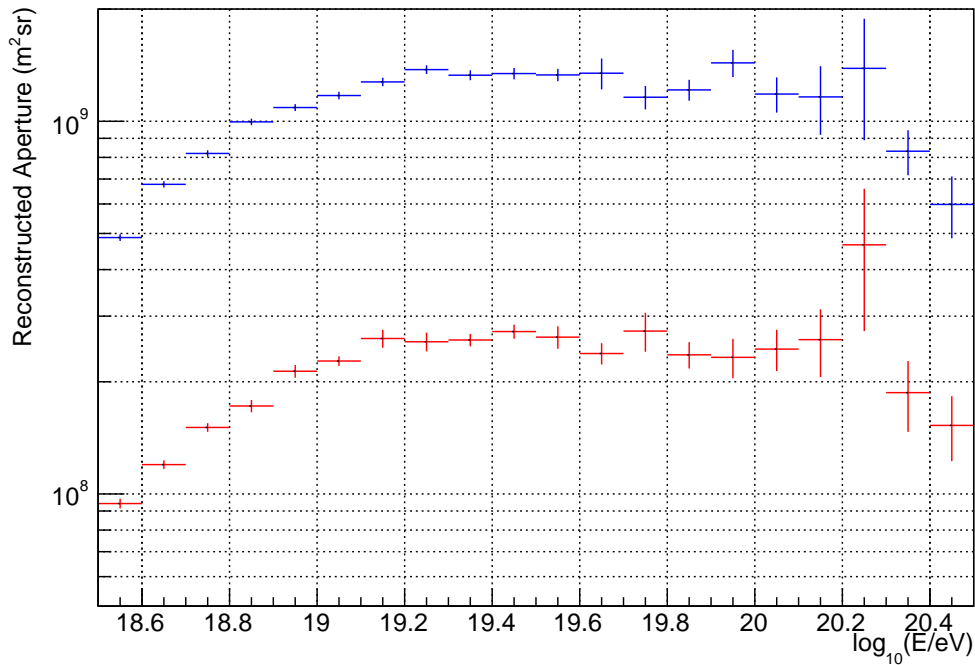


Figure 7.2: TAX4 reconstructed aperture above $10^{18.5}$ eV. The red data points represent TAX4 North's aperture and the blue data points represent TAX4 South's aperture.

includes good weather as well as bad weather data. In my quality cuts, I select events that pass a good weather condition; therefore, the weather cut effect has to be taken into account during the detector ontime calculation. The good weather ontime for TAx4 North and TAx4 South is 969.91 and 539.73 hours, respectively.

7.1.4 Exposure

The detector's exposure is defined as the product of the detector's aperture and ontime, written as

$$\epsilon = A\Omega T = \frac{N_{recon}(E)}{N_{thrown}(E)} A_0 \Omega_0 \times T. \quad (7.6)$$

Since the field of view of the TAx4 sites don't overlap, the total exposure for TAx4, ϵ_{TAx4} , simplifies to a sum given by

$$\epsilon_{TAx4} = \epsilon_N + \epsilon_S = A\Omega_N \times T_N + A\Omega_S \times T_S, \quad (7.7)$$

where ϵ_N and ϵ_S are the exposures, $A\Omega_N$ and $A\Omega_S$ are the apertures, and T_N and T_S are the good weather ontimes of TAx4 North and TAx4 South respectively. The calculated exposures is shown in Figure 7.4.

7.2 Energy Spectrum

The TAx4 hybrid energy spectrum was calculated using a little more than two years of data from July 26, 2019, to October 11, 2021. This work's spectrum uses data from both the Northern and Southern arrays to create a combined TAx4 hybrid spectrum. After all cuts, 159 hybrid events remain and are used in this energy spectrum calculation. The MC simulation is thrown up to 10^{21} eV so that the measurement is able to explore the highest energy region of the cosmic ray energy spectrum.

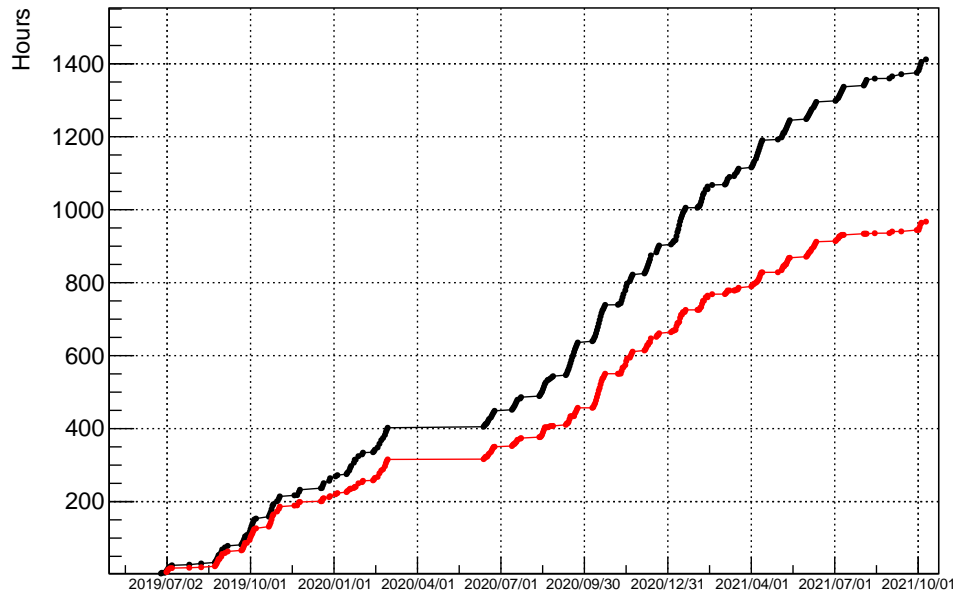
The flux of cosmic rays is calculated using Equation 7.1 and shown in Figure 7.5. This plot includes this work's calculated cosmic ray flux, represented by black squares, and the ICRC 2019 TA combined energy spectrum, represented by red circles. The number above each of the black points is the number of data events used to calculate the flux in that bin. In order to take out the dominant slope of the cosmic ray flux, both distributions are multiplied by energy to the third power, $E^3 J(E)$, and the result is shown in Figure 7.6. Figure 7.7 shows the ratio of this work's energy spectrum to the ICRC 2019 TA combined energy spectrum result. This plot has a fitted line to show the level of agreement between

Telescope	Total Ontime (hours)	
25	1366.6284	
26	1381.0281	
27	1339.3858	
28	1352.4767	
29	818.6036	
30	817.3898	
31	821.9800	
32	753.3116	
33	818.8213	
34	788.7251	
35	811.7769	
36	768.8446	
Site	Total Ontime (hours)	GW Ontime (hours)
TAX4 North	1420.1697	969.9144
TAX4 South	827.5822	539.7292
TAX4 Combined	2247.7492	1509.6436

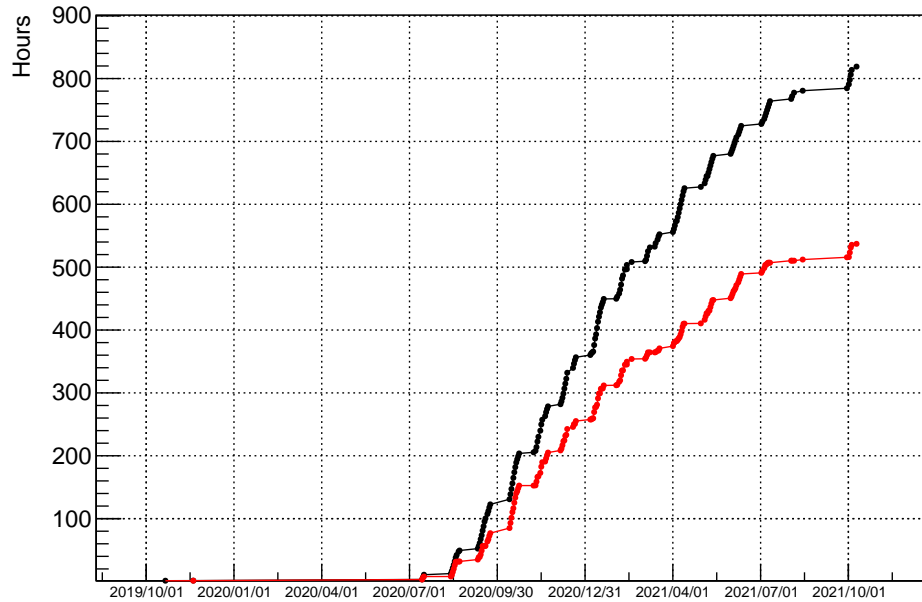
Table 7.3: TAX4 ontimesummary. The total ontimes is shown for each individual mirror. Mirrors 25-28 belong to TAX4 North and mirrors 29-36 belong to TAX4 South. The total ontimes for each TAX4 detector site is listed at the bottom of the table, as well as the good weather ontimes (ontimes after good weather cut is applied).

$\log_{10}(E/eV)$	TAX4 Exposure ($m^2 \text{sr s}$)
18.55	1.276×10^{15}
18.65	1.735×10^{15}
18.75	2.119×10^{15}
18.85	2.537×10^{15}
18.95	2.861×10^{15}
19.05	3.072×10^{15}
19.15	3.391×10^{15}
19.25	3.568×10^{15}
19.35	3.487×10^{15}
19.45	3.562×10^{15}
19.55	3.508×10^{15}
19.65	3.447×10^{15}
19.75	3.210×10^{15}
19.85	3.184×10^{15}
19.95	3.600×10^{15}
20.05	3.154×10^{15}
20.15	3.165×10^{15}
20.25	4.322×10^{15}
20.35	2.268×10^{15}
20.45	1.696×10^{15}

Table 7.4: TAX4 hybrid exposure per energy bin.



(a) Ontime of TAx4 North FD.



(b) Ontime of TAx4 South FD.

Figure 7.3: TAx4 ontine plots. The black histogram show the total ontine and the red histogram show the good weather ontine of the detector. The good weather ontine is calculated by applying the good weather quality cut, discussed in Chapter 6, to the total ontine. The large gap in the ontine seen between March 2020 and June 2020 was due to the COVID-19 shutdown.

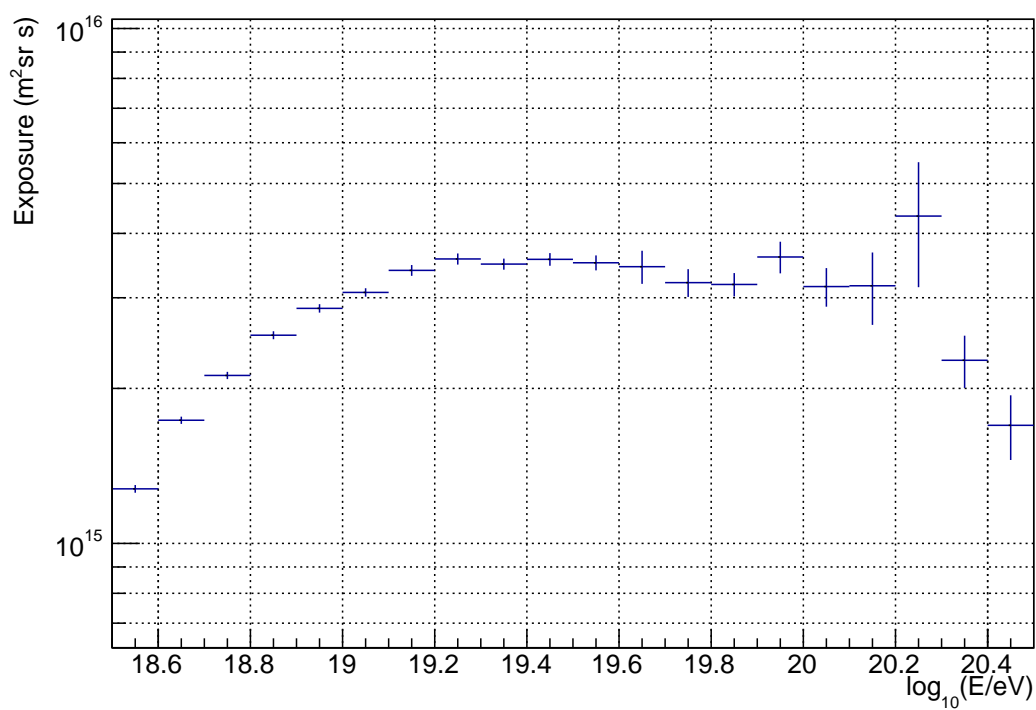


Figure 7.4: TAx4 hybrid exposure above $10^{18.5}$ eV. The blue data points represent the combined exposure of both TAx4 sites.

the two. The slope is relatively flat, indicating okay agreement between this works energy spectrum and TA's ICRC 2019 combined energy spectrum.

$\log_{10}(E/eV)$	J(E)	J(E) Lower Error	J(E) Upper Error
18.55	3.158×10^{-32}	5.497×10^{-33}	5.497×10^{-33}
18.65	1.846×10^{-32}	1.846×10^{-33}	1.846×10^{-33}
18.75	7.635×10^{-33}	1.666×10^{-33}	1.666×10^{-33}
18.85	3.619×10^{-33}	8.878×10^{-34}	1.043×10^{-33}
18.95	2.719×10^{-33}	6.229×10^{-34}	7.368×10^{-34}
19.05	1.006×10^{-33}	3.388×10^{-34}	4.174×10^{-34}
19.15	8.143×10^{-34}	2.411×10^{-34}	3.018×10^{-34}
19.25	4.781×10^{-34}	1.530×10^{-34}	2.257×10^{-34}
19.35	1.665×10^{-34}	1.052×10^{-34}	1.279×10^{-34}
19.45	3.453×10^{-34}	1.163×10^{-34}	1.433×10^{-34}
19.55	6.964×10^{-35}	4.387×10^{-35}	6.876×10^{-35}
19.65	5.629×10^{-35}	3.546×10^{-35}	5.559×10^{-35}
19.75	2.401×10^{-35}	1.513×10^{-35}	4.214×10^{-35}
19.85	0	0	0
19.95	1.351×10^{-35}	8.509×10^{-36}	2.370×10^{-35}
20.05	0	0	0

Table 7.5: TAx4 hybrid energy spectrum value for each energy bin. The upper and lower errors of the flux are also show for each energy bin.

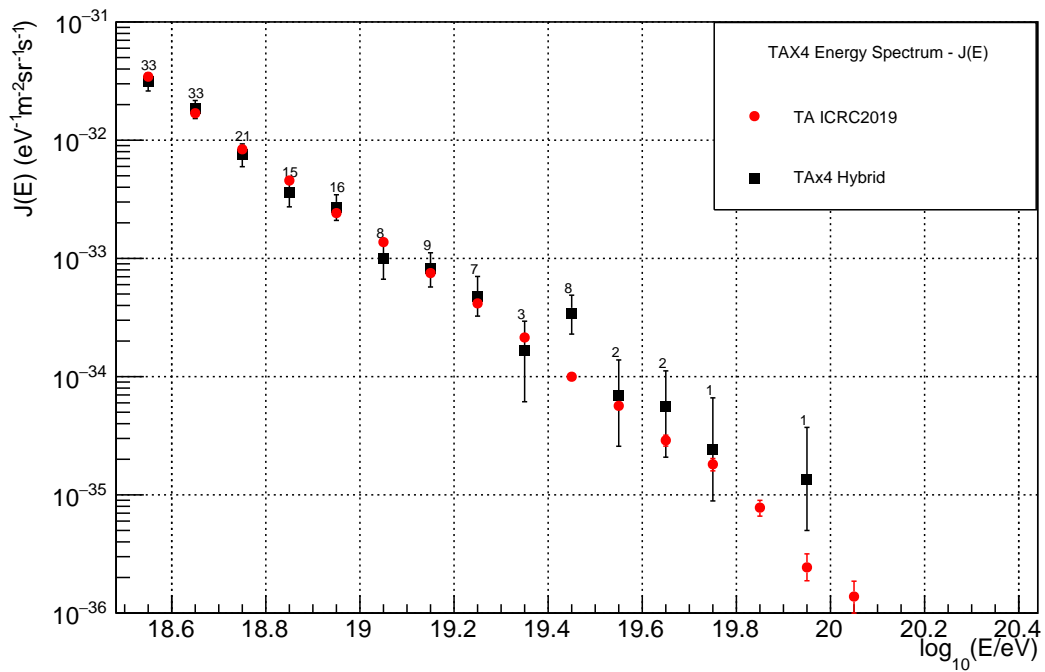


Figure 7.5: Hybrid Energy Spectrum - J(E). The black data points represent this work's hybrid energy spectrum. Above each black data point is the number of data events in that energy bin. The red points represent the TA ICRC2019 combined energy spectrum.

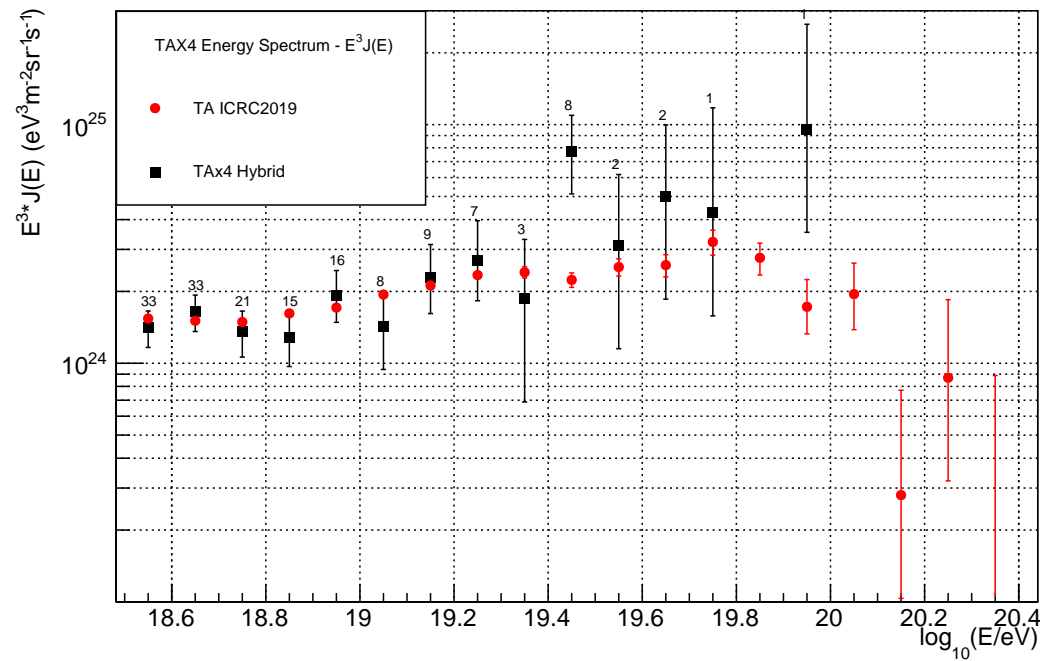


Figure 7.6: Hybrid Energy Spectrum - $E^3 J(E)$. The flux, see Figure 7.5, is multiplied by E^3 to bring out the features of the cosmic ray spectrum. This removes the effective E^{-3} trend. The black data points represent this work's $E^3 J(E)$ hybrid energy spectrum. Above each black data point is the number of data events in that energy bin. The red points represent the TA ICRC2019 combined energy spectrum.

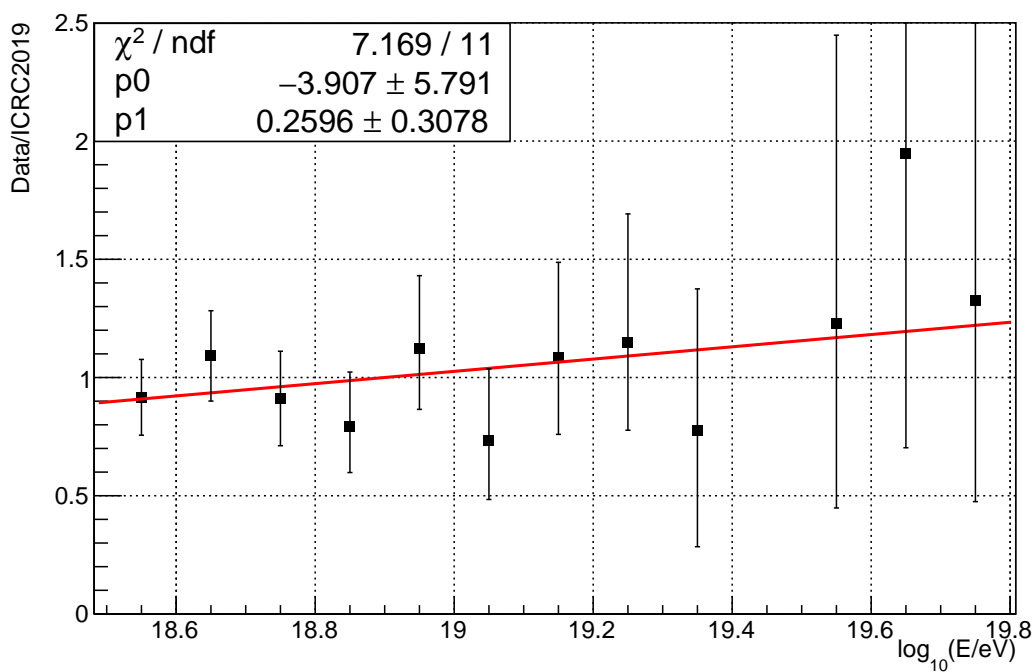


Figure 7.7: Ratio of this works hybrid energy spectrum and TA's ICRC2019 combined energy spectrum. The black data points represent the ratio, and the red line is a pol1 fitted to the ratio. The statistics box shows the resulting fit's slope, constant, and χ^2/ndf . The slope is shallow indicating reasonable agreement.

CHAPTER 8

CONCLUSIONS

Ultra-High Energy Cosmic Rays (UHECRs) are known as the most energetic particles in the Universe; however, the sources of these UHECRs are yet unknown. The assumption is that they come from large violent extragalactic astrophysical objects. UHECR studies aim to understand where they come from, what is their chemical composition, how they are accelerated to such high energies, and how they propagate through the intergalactic medium. The work in this dissertation is focused on calculating the cosmic ray energy spectrum of cosmic rays with energies greater than $10^{18.5}$ eV. The cosmic ray energy spectrum measurement is essential because it can hint at where UHECRs come from. This is because spectral features can indicate the energy distributions of particles at astrophysical sources and can imply a difference in chemical composition between galactic and extragalactic particles. This work's energy spectrum spans two important spectral features, the ankle and GZK cutoff. Cosmic rays in this energy range are speculated to be light in their composition. Future analyses will build upon this work to help determine the composition of cosmic rays at the highest energies.

I used TAx4 epoch II data that was collected between June 26, 2019, and October 28, 2021, combining the data from both TAx4 sites. The quality cuts select well-reconstructed cosmic ray events while being open enough to have higher event statistics. This work's energy spectrum only uses events above $10^{18.5}$ eV. In this energy range, the hybrid trigger for the SDs is assumed to be 100%. After all the cuts were applied to the data, there were 159 hybrid events retained and used for this work's hybrid energy spectrum calculation.

The TAx4 hybrid aperture depends significantly on energy. Higher energy events are brighter and can be seen from farther away, while lower energy events are only seen nearby. At the highest energies, the aperture is restricted by the boundary of the SD array. The aperture and acceptance of the detector are calculated by an inverse Monte Carlo

(MC) technique. The MC simulates an Extensive Air Showers (EAS) and the FD detector response. Afterward, a parametric MC adds 100% efficient SDs with nominal calibration values to the FD MC. Next, the MC events are processed through the same programs as the data. Finally, the fully reconstructed data and MC distributions were compared and shown to agree with each other. Then the MC information is used to calculate the aperture and exposure, which is required to determine the cosmic ray energy spectrum.

In conclusion, this work examines the earliest stable running of the TAx4 hybrid detector to measure the cosmic ray spectrum. This work's hybrid energy spectrum using both TAx4 sites has been demonstrated to agree with TA's energy spectrum measurement presented at the ICRC2019. More statistics are required to examine the energy spectrum features, but this work is a crucial first step measurement needed before a composition study can take place, which will be left for a future project.

REFERENCES

- [1] R. U. Abbasi *et al.* Indications of Intermediate-Scale Anisotropy of Cosmic Rays with Energy Greater than 57 EeV in the Northern Sky measured with the Surface Detector of the Telescope Array Experiment. *The Astrophysical Journal*, 790(2):L21, July 2014.
- [2] R. U. Abbasi *et al.* Measurement of the proton-air cross section with telescope array's middle drum detector and surface array in hybrid mode. *Physical Review D*, 92(3), August 2015.
- [3] R. U. Abbasi *et al.* Search for EeV Protons of Galactic Origin. *Astropart. Phys.*, 86:21–26, 2017.
- [4] R. U. Abbasi *et al.* Depth of Ultra High Energy Cosmic Ray Induced Air Shower Maxima Measured by the Telescope Array Black Rock and Long Ridge FADC Fluorescence Detectors and Surface Array in Hybrid Mode. *The Astrophysical Journal*, 858(2):76, May 2018.
- [5] R. U. Abbasi *et al.* Surface detectors of the TAx4 experiment. *Nuclear Instruments and Methods in Physics Research Section A: Accelerators, Spectrometers, Detectors and Associated Equipment*, page 165726, 2021.
- [6] R. U. Abbasi *et al.* Surface detectors of the tax4 experiment. *Nuclear Instruments and Methods in Physics Research Section A: Accelerators, Spectrometers, Detectors and Associated Equipment*, 1019:165726, 2021.
- [7] T. Abu-Zayyad *et al.* The surface detector array of the telescope array experiment. *Nuclear Instruments and Methods in Physics Research Section A: Accelerators, Spectrometers, Detectors and Associated Equipment*, 689:87–97, 2012.
- [8] T. AbuZayyad. *The Energy Spectrum of Ultra High Energy Cosmic Rays*. Ph.D. Thesis, University of Utah, Salt Lake City, UT, USA, 2000.
- [9] M. Allen. *Ultra High Energy Cosmic Ray Energy Spectrum and Composition using Hybrid Analysis with Telescope Array*. Ph.D. Thesis, University of Utah, Salt Lake City, UT, USA, 2012.
- [10] E. L. Barcikowski. *The Composition of Ultra High Energy Cosmic Rays through Hybrid Analysis at Telescope Array*. Ph.D. Thesis, University of Utah, Salt Lake City, UT, USA, 2011.
- [11] J. H. Boyer, B. C. Knapp, E. J. Mannel, and M. Seman. FADC-based DAQ for HiRes Fly's Eye. *Nucl. Instrum. Meth. A*, 482:457–474, 2002.
- [12] D. Heck, G. Schatz, T. Thouw, J. Knapp, and J. Capdevielle. CORSIKA: A Monte Carlo code to simulate extensive air showers. *Forschungszentrum Karlsruhe - Wissenschaftliche Berichte*, 1998.

- [13] G. D. Furlich. *Observation of the GZK Suppression with the Telescope Array Fluorescence Telescopes and Deployment of the Telescope Array Expansion*. Ph.D. Thesis, University of Utah, Salt Lake City, UT, USA, 2020.
- [14] T. K. Gaisser. *Cosmic Rays and Particle Physics*, page 226 (Chapter 15). Cambridge University Press, 1990.
- [15] T. K. Gaisser and A. M. Hillas. Reliability of the Method of Constant Intensity Cuts for Reconstructing the Average Development of Vertical Showers. In *International Cosmic Ray Conference*, volume 8 of *International Cosmic Ray Conference*, page 353, Jan. 1977.
- [16] Hamamatsu Photonics K.K. Editorial Committee. *Photomultiplier Tube Basics and Applications*. Hamamatsu Photonics, 2017.
- [17] W. F. Hanlon. *The Energy Spectrum of Ultra High Energy Cosmic Rays Measured by the High Resolution Fly's Eye Observatory in Stereoscopic Mode*. Ph.D. Thesis, University of Utah, Salt Lake City, UT, USA, 2008.
- [18] W. Heilter. *The Quantum Theory of Radiation, Third Edition*, page 386 (Section 38). Oxford University Press, London, 1954.
- [19] D. Ivanov. *Energy Spectrum Measured by the Telescope Array Surface Detector*. Ph.D. Thesis, Rutgers, The State University of New Jersey, New Brunswick, New Jersey, 2012.
- [20] D. Ivanov. Energy Spectrum Measured by the Telescope Array Experiment. In *Proceedings of the International Cosmic Ray Conference (ICRC2019)*, Madison, USA, 2019.
- [21] J. J. Beatty, J. Matthews, S. P. Wakely. Cosmic Rays. Particle Data Group. 2019.
- [22] Keilhauer, B., Bohacova, M., Fraga, M., Matthews, J., Sakaki, N., Tameda, Y., Tsunesada, Y., and Ulrich, A. Nitrogen fluorescence in air for observing extensive air showers. *EPJ Web of Conferences*, 53:01010, 2013.
- [23] J. Kim. *The Cosmic Ray Spectrum Above 0.1 EeV Measured by the Telescope Array and TALE Fluorescence Telescopes*. Ph.D. Thesis, University of Utah, Salt Lake City, UT, USA, 2018.
- [24] Kuraray. *Plastic Scintillating Fibers*. page 4, Kuraray Co., Ltd., 2014.
- [25] Linsley, J., In NASA. Goddard Space Flight Center 19th International Cosmic Ray Conference, 7, 359, 1985.
- [26] J. Matthews. A Heitler model of extensive air showers. *Astroparticle Physics*, 22(5-6):387–397, Jan. 2005.
- [27] S. Ogio. Telescope Array Low-energy Extension (TALE) hybrid. In *Proceedings of the International Cosmic Ray Conference (ICRC2019)*, Madison, USA, 2019.
- [28] M. Potts. Monocular Energy Spectrum using the TAx4 Fluorescence Detector. In *Proceedings of the International Cosmic Ray Conference (ICRC2019)*, Madison, USA, 2019.

- [29] D. C. Rodriguez. *The Telescope Array Middle Drum Monocular Energy Spectrum and a Search for Coincident Showers Using High Resolution Fly's Eye HiRes-I Monocular Data*. Ph.D. Thesis, University of Utah, Salt Lake City, UT, USA, 2011.
- [30] Telescope Array Collaboration. Indications of a Cosmic Ray Source in the Perseus-Pisces Supercluster, 2021.
- [31] J. A. *et al.* Recent developments in geant4. *Nuclear Instruments and Methods in Physics Research Section A: Accelerators, Spectrometers, Detectors and Associated Equipment*, 835:186–225, 2016.
- [32] S. A. *et al.* Geant4—a simulation toolkit. *Nuclear Instruments and Methods in Physics Research Section A: Accelerators, Spectrometers, Detectors and Associated Equipment*, 506(3):250–303, 2003.
- [33] Z. Zundel. *Spectrum Measurement with the Telescope Array Low Energy Extension (TALE) Fluorescence Detector*. Ph.D. Thesis, University of Utah, Salt Lake City, UT, USA, 2016.